

Multicomponent local Lorentz force velocimetry

Dissertation

zur Erlangung des akademischen Grades

Doktoringenieur

(Dr.-Ing.)

vorgelegt der

Fakultät für Maschinenbau der

Technischen Universität Ilmenau

von Herrn

Ingeniero Mecánico Daniel Hernández Hernández

geboren am 08.01.1987 in Bogotá, Kolumbien

1. Gutachter: apl. Prof. Dr.-Ing. habil. Christian Karcher
2. Gutachter: Prof. Dr.-Ing. Leo Bühler
3. Gutachter: Dr. Sergio Cuevas García

Tag der Einreichung: 12.10.2017

Tag der wissenschaftlichen Aussprache: 12.04.2018

urn:nbn:de:gbv:ilm1-2018000137

Abstract

Lorentz force velocimetry (LFV) is a contactless velocity measurement technique for liquid metals. Due to the relative motion between an electrically conductive fluid and a static applied magnetic field, eddy currents and a flow-braking Lorentz force are generated inside the metal melt. This force is proportional to the electrical conductivity of the fluid and to the flow rate or local velocity, depending on the portion of the flow volume spanned by the magnetic field. Due to Newton's third law, a force of the same magnitude but in the opposite direction acts on the source of the applied magnetic field, which are permanent magnets in our case. According to Ohm's law, moving conductors at low magnetic Reynolds numbers induce an electric potential that ensures charge conservation. This thesis begins with a study of the contribution of the induced electric potential in the total Lorentz force. This problem is numerically and experimentally analyzed by considering two different scenarios: conducting walls of finite thickness and the aspect ratio variation of the flow cross-section. In both cases, the force component generated by the electric potential always opposed the total Lorentz force. This force component was sensitive to the electric boundary conditions of the flow, of which insulating and perfectly conducting walls are the two limiting cases. It is shown that the measurable Lorentz force can be considerably increased when the force component originating from the electric potential is decreased, by either changing the electrical conductivity of the wall or by modifying the aspect ratio of the cross-section of the flow. Hence, the sensitivity of the measurement technique can also be significantly improved.

Following this analysis, this thesis focuses on multicomponent local Lorentz force velocimetry. This technique is based on the measurement of all force and torque components acting on magnet systems that are significantly smaller than the cross-section of the flow. In this scenario, the rapid decay of magnetic fields induces a localized magnetic field distribution in the liquid metal allowing a local velocity assessment. Multicomponent local Lorentz force velocimetry was studied using a steady three-dimensional turbulent flow inside the mold of a continuous casting model, where the working fluid was GaInSn in eutectic composition. The magnet systems composed of cubic and cross-shaped permanent magnets were attached to a sensor that was spe-

cially developed to simultaneously record all three force and three torque components. With this sensor, it was possible to obtain information on the three-dimensional velocity distribution of the liquid metal inside the mold in the region adjacent to its wall next to the magnet. Additionally, by using a cross-shaped magnet, the torque in the direction of magnetization of the magnet could be measured. According to a numerical model of the experiments, this torque correlates with the curl of the velocity field in this direction.

Zusammenfassung

Lorenzkraft-Anemometrie (LKA oder LFV) ist ein berührloses elektromagnetisches Strömungsmessverfahren für Flüssigmetalle. Durch eine Relativbewegung zwischen einem elektrischen leitfähigen Fluid und einem statisch angelegten Magnetfeld werden Wirbelströme und eine strömungsbremsende Lorentzkraft erzeugt. Diese Kraft ist proportional zu der elektrischen Leitfähigkeit des Fluides und zu der Durchflussrate oder zu der lokalen Geschwindigkeit, welche abhängig von dem Anteil des durch das Magnetfeld aufgespannten Volumens ist. Gemäß dem dritten newtonschen Gesetz wirkt eine gleich starke, jedoch entgegengesetzt gerichtete Kraft auf die Quelle des angelegten Magnetfeldes, die in unserem Fall Permanentmagnete sind. Entsprechend dem Ohm'schen Gesetz induzieren bewegende elektrisch leitfähige Fluide bei niedrigen magnetischen Reynolds-Zahlen ein elektrisches Potential, das die Ladungserhaltung gewährleistet. Diese Arbeit beginnt mit der Untersuchung des Beitrags des induzierten elektrischen Potentials in der gesamten Lorentzkraft. Dieses Problem wird numerisch und experimentell analysiert, indem zwei verschiedene Szenarien betrachtet werden: elektrisch leitfähige Wände mit endlicher Dicke und Aspektverhältnisvariation des Strömungsquerschnitts. In beiden Fällen stand die durch das elektrische Potential erzeugte Kraftkomponente immer entgegen der gesamten Lorentzkraft. Diese Kraftkomponente war empfindlich gegenüber den elektrischen Randbedingungen der Strömung, von denen isolierte und perfekt leitende Wände die Grenzfälle sind. Es wird gezeigt, dass die messbare Lorentzkraft beträchtlich erhöht werden kann, wenn die aus dem elektrischen Potential stammende Kraftkomponente verringert wird, indem entweder die elektrische Leitfähigkeit der Wand oder das Querschnittsverhältnis der Strömung verändert wird. Daher kann die Empfindlichkeit der Messtechnik erheblich verbessert werden.

Im Anschluss an dieser Analyse konzentriert sich die vorliegende Arbeit auf die lokale Multikomponenten-Lorenzkraft-Anemometrie. Diese Technik basiert auf der Messung aller auf den Magnetsystemen wirkenden Kraft- und Drehmomentkomponenten. In diesem Fall sind die Magnetsysteme deutlich kleiner als der Strömungsquerschnitt. Die kleinen Magnetsysteme induzieren eine lokalisierte Magnetfeld-

verteilung im flüssigen Metall, die eine lokale aufgelöste Geschwindigkeitsmessung von flüssigem Metall ermöglichen. Die lokale Multikomponenten-Lorentzkraft-Anemometrie wurde mittels einer stetigen dreidimensionalen turbulenten Strömung innerhalb der Kokille eines Stranggussmodells untersucht, wobei das Arbeitsfluid GaInSn in eutektischer Zusammensetzung war. Die aus kubischen und kreuzförmigen Permanentmagneten bestehenden Magnetsysteme wurden an einem Sensor befestigt, der speziell für die gleichzeitige Erfassung aller drei Kraft- und drei Drehmomentkomponenten entwickelt wurde. Mit diesem Sensor war es möglich, Informationen über die dreidimensionale Geschwindigkeitsverteilung des flüssigen Metalls innerhalb der Kokille in der Nähe der Magneten zu erhalten. Zusätzlich könnte unter Verwendung eines kreuzförmigen Magneten das Drehmoment in der Feldrichtung des Magneten gemessen werden. Gemäß einem numerischen Modell der Experimente korreliert dieses Drehmoment mit der Wirbelstärke des Geschwindigkeitsfeldes in dieser Richtung.

List of Abbreviations

LFV	Lorentz force velocimetry
UDV	Ultrasonic Doppler velocimetry
LFF	Lorentz force flowmeter
L2F2	Local Lorentz force flowmeter
1D-L2F2	1D local Lorentz force flowmeter composed of a 1D interference optical force sensor attached to a magnet system
6D-L2F2	Six-degrees-of-freedom local Lorentz force flowmeter composed of a multicomponent force/torque sensor attached to a magnet system
LITINCA	Liquid tin calibration facility
SOMECA	Solid metal calibration facility
ILMET	Ilmenau liquid metal channel
mini-LIMMCAST	Liquid metal model of continuous casting of steel
$CUB_{l_{mag}}$	Magnet system compose of a cubic permanent magnet with characteristic length l_{mag}
$CSM_{l_{mag}}$	Magnet system compose of a cross-shaped permanent magnet with characteristic length l_{mag}
$CSMA_{l_{mag}}$	Magnet system compose of small permanent magnets glued in a cross-shaped form with characteristic length l_{mag}
RMS	Root mean square



Contents

Abstract	iii
Zusammenfassung	v
Contents	ix
1 Introduction	1
2 Lorentz force velocimetry	5
2.1 Magnetohydrodynamic equations	5
2.2 Theory of Lorentz force velocimetry	6
2.3 State of the art	9
2.3.1 Flow rate measurement	10
2.3.2 Local Lorentz force velocimetry	13
3 Electric potential in Lorentz force velocimetry	17
3.1 Wall conductivity effect	18
3.1.1 Experimental set-up and results	19
3.1.2 Analytic model	20
3.1.2.1 Limiting case of infinite wall conductivity	21
3.1.2.2 Limiting case of insulating walls	23
3.1.3 Numerical model	25
3.1.4 Numerical results	27
3.2 Aspect ratio variation	31
3.2.1 Experimental set-up and results	32
3.2.2 3D Model	33
3.2.3 2D Model	36
3.3 Lorentz force velocimetry in electrolytes	38
3.4 Conclusions	42

CONTENTS

4	1D local Lorentz force velocimetry	45
4.1	Magnet systems	45
4.1.1	Magnetic field distribution	47
4.2	Experimental set-up	48
4.3	Results	49
4.4	Conclusions	52
5	Multicomponent local Lorentz force velocimetry	55
5.1	Multicomponent local Lorentz force flowmeter	56
5.2	Magnet systems	57
5.3	Dry calibration	60
5.3.1	Numerical model	62
5.3.2	Results	62
5.3.3	Two-dimensional limit	66
5.3.4	Calibration factor	67
5.3.5	Calibration set-up	68
5.4	Experimental set-up mini-LIMMCAST	69
5.4.1	Measurement procedure	70
5.5	Numerical model	72
5.6	Results using the CUB ₁₅	74
5.6.1	Torque-to-force ratio	78
5.6.2	Calibration factor	81
5.7	Results using the CSM _{31.17}	82
5.7.1	Torque-to-force ratio	85
5.8	Spatial resolution	86
5.9	Conclusions	90
6	Summary and Outlook	93
	A List of publications	96
	B General description of the numerical model	98
	C Uncertainty analysis	101
	References	107
	Erklärung	115
	Acknowledgements	117

Chapter 1

Introduction

In metallurgy, the measurement of flow rates and local velocities in liquid metals is given high priority in order to accurately control the process for optimizing final product quality. However, the aggressiveness and high temperatures of liquid metals remain a large obstacle to the application of already-established and commercially available contact measurement techniques like the use of a Pitot tube, Vives probe, or hot-wire anemometer. Even contactless optical measurement techniques such as particle image velocimetry (PIV) fail due to the opacity of liquid metals (for an overview of established measurement techniques see [62]). Following the work of Takeda [54], ultrasound Doppler velocimetry (UDV) probes have been widely accepted and established as a standard for measuring the local velocity of metal melts at low temperatures, typically up to 80°C. Liquid temperatures can be even higher, up to 200°C when using liquid sodium, by using high-temperature UDV probes and a special stainless steel adapter that covers the front wall of the ultrasonic transducer [9]. Additionally, this technique has been applied in liquid metals such as PbBi at elevated temperatures up to 620°C by using an acoustic wave guide [10]. However, a large gap remains in applying in more extreme environments such as the continuous casting of steel (see figure 1.1(a)). Assessing flow characteristics like vorticity or curl have presented a formidable challenge since accurate velocity measurements over small distances is required. PIV and hot-wire probes have been used for this task in transparent liquids such as water [62], but as previously explained, they cannot be used for hot, opaque and aggressive liquid metals.

In order to overcome these challenges, the development of reliable contactless measurement techniques is of considerable interest. One large subgroup of methods is based on Faraday's induction principle. Here, the relative motion between an electrically conductive fluid and an externally applied magnetic field is used for velocity measurements. This is the basis of contactless inductive flow tomography (CIFT) [51],

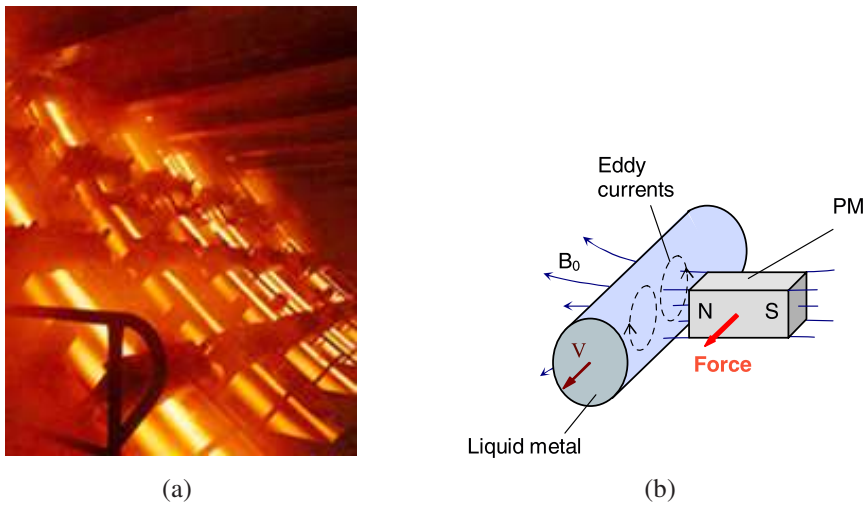


Figure 1.1: (a) Photograph of a continuous casting plant [6]. (b) Sketch of Lorentz force velocimetry showing the action of a permanent magnet (PM) on the flow of an electrically conducting fluid. The magnetic field generating system consists of permanent magnets [59].

the contactless electromagnetic phase-shift flowmeter [40], and the single-magnet rotary flowmeter [39], among others (for an overview see [44]). Lorentz force velocimetry (LFV) also belongs to this group of contactless measurements techniques [58, 59]. Lorentz force velocimetry is based on magnetohydrodynamics: due to the relative motion between an electrically conductive fluid and a static applied magnetic field \vec{B}_0 , eddy currents and a flow-braking Lorentz force are generated inside the metal melt (see figure 1.1(b)). According to Ohm's law, moving conductors at low magnetic Reynolds numbers induce an electric potential that ensures charge conservation (see section 2.2). This force is proportional to the electrical conductivity of the fluid, to the square of the applied magnetic field and to the flow rate or local velocity, depending on the portion of the flow volume spanned by the magnetic field. By using small magnets, a localized magnetic field distribution can be created that allows measurement of the local velocity in the region adjacent to the wall. Because it is localized, this subcategory of LFV is called local Lorentz force velocimetry (local LFV).

The two main goals of the present work are to develop a better understanding of the influence of the induced electric potential seen in LFV and to study local LFV in complex three-dimensional liquid metal flows by measuring all force and torque components that act on a given magnet system. The structure of the thesis is as follows: chapter 2 gives an overview of the present state of contactless flow rate and local velocity measurements of electrically conducting liquids in the framework of LFV. Then, chapter 3 describes the influence of the induced electric potential on the magnitude of the measurable Lorentz force by covering two specific cases: conducting walls and aspect ratio variation of the flow cross-section. This is an extension to previous work

on LFV (section 2.3) and offers the possibility of further improvements to the sensitivity of the measurement technique, especially for low-conductivity liquids such as electrolytes. This study is experimentally and numerically investigated using a turbulent pipe flow with different wall conductivities and a solid bar with rectangular cross-section.

Following this analysis, this thesis extends previous experimental work of local LFV (section 2.3.2), which have been based primarily on measuring individual components of the Lorentz force acting on a cubic permanent magnet. The aim of the present study is to experimentally and numerically investigate the concept of multicomponent sensing of the three force and three torque components acting on a magnet system. In this context, new magnet systems with different geometries (cross-shaped magnets) as well as cubic magnets (the current state of the art) are investigated in two experiments. Cross-shaped magnets have particular features that can generate a non-axisymmetric magnetic field distribution in the liquid, allowing measurement of the torque that points into the magnetization of the magnet. The first set-up consists of a one-dimensional interference optical force sensor connected to a magnet system, which is placed next to a rectangular duct in fully-developed turbulent flow. The results obtained with this set-up are described in chapter 4. The second set-up consists of a multicomponent force and torque sensor attached to different magnet systems that scans the wide face of the mold of a continuous caster model. The multicomponent force and torque sensor provides unprecedented simultaneous sensing of all three force and three torque components acting on a given magnet system. The results of multicomponent local LFV are presented in chapter 5. The working fluid in both set-ups is GaInSn in eutectic composition, and the magnet systems are moved along pre-determined measurement paths, in order to infer local information on the three-dimensional velocity distribution of the liquid metal. Finally, chapter 6 summarizes the main results and gives by a brief outlook toward future work.

Chapter 2

Lorentz force velocimetry

Lorentz force velocimetry (LFV) [59, 58] is part of the research area of magnetohydrodynamics and belongs to the subgroup of contactless velocity measurement techniques for electrically conducting fluids. This chapter starts with the fundamental equations of magnetohydrodynamics followed by the theoretical background of LFV. Afterwards, a brief overview of the current state of the art of LFV is presented focusing on flow rate and local velocity assessment.

2.1 Magnetohydrodynamic equations

Magnetohydrodynamics (MHD) studies the interaction between magnetic fields and moving liquids. The liquids are non-ferromagnetic, electrically conducting, incompressible and treated as continuous. According to [50], the governing equations in dimensionless form (* superscript) that describe the physics involve are: the Navier-Stokes equation for incompressible flow with Lorentz force term \vec{f}

$$\frac{\partial \vec{u}^*}{\partial t} + (\vec{u}^* \cdot \nabla) \vec{u}^* = -\nabla p^* + \frac{\nabla^2 \vec{u}^*}{Re} + N \vec{f}^* \quad \text{with} \quad \nabla \cdot \vec{u}^* = 0 \quad (2.1, 2.2)$$

and the transport equation of magnetic fields

$$\frac{\partial \vec{B}^*}{\partial t} = \nabla \times (\vec{u}^* \times \vec{B}^*) + \frac{\nabla^2 \vec{B}^*}{R_m} \quad \text{with} \quad \nabla \cdot \vec{B}^* = 0. \quad (2.3, 2.4)$$

In (2.1) the velocity field \vec{u}^* is driven by the pressure gradient ∇p^* , where no-slip boundary conditions are applied ($\vec{u}^* = 0$ on any stationary solid surface). Here, Re and N denote the Reynolds number and the interaction parameter or Stuart number,

respectively. Re is the ratio of inertia to viscous shear forces defined as

$$Re = \frac{ul_c}{\nu}, \quad (2.5)$$

where l_c , u and ν denote the characteristic length, velocity scale and the kinematic viscosity of the liquid, respectively. In the case of N , it represents the ratio of Lorentz forces to inertia defined as

$$N = \frac{\sigma_l B^2 l_c}{\rho u} = \frac{Ha^2}{Re}, \quad (2.6)$$

where ρ and σ_l denote the density and the electrical conductivity of the liquid, respectively. For simplicity, the properties of the fluid σ_l , ρ and ν are normally considered constant and known. In (2.6) another important dimensionless number appears defined as

$$Ha = \sqrt{NRe}. \quad (2.7)$$

Ha is the so-called Hartmann number and is typically used for scaling the magnitude of the applied magnetic field in a given system.

In the case of (2.3), it is the combination of Ohm's law (see section 2.2), Faraday's equation and Ampère's law [5]. It represents how the magnetic field inside a moving conductor changes in time by advection (first term on the right) and diffusion (second term on the right). Here, \vec{B} represents the sum of the applied field \vec{B}_0 and the flow induced field \vec{b} . The duct walls containing the electrically conducting liquid are considered to be electrically insulating which translates to vanishing wall normal current density $j_n = 0$. Finally, R_m represents the magnetic Reynolds number which is proportional to the ratio of $|\vec{b}|$ to $|\vec{B}_0|$. R_m is defined as

$$R_m = l_c u / \lambda = \mu_0 \sigma_l l_c u, \quad (2.8)$$

where $\lambda = (\mu_0 \sigma_l)^{-1}$ is the magnetic diffusivity and μ_0 denotes the permeability of free space.

2.2 Theory of Lorentz force velocimetry

When an electrically conducting fluid flows through a static magnetic field \vec{B}_0 (figure 2.1(a)), the current density

$$\vec{j} = \sigma_l (\vec{E} + \vec{u} \times \vec{B}) \quad (2.9)$$

is induced according to Ohm's law for moving conductors (figure 2.1(b)). Here, \vec{E} represents the induced electric field. These eddy currents in the liquid generate a secondary magnetic field \vec{b} (figure 2.1(c)). For low $R_m \ll 1$, which is the case for most industrial applications, \vec{b} is negligible in comparison with \vec{B}_0 so $\vec{B} \approx \vec{B}_0$. In this case, the electric field \vec{E} is irrotational and can be written as $-\nabla\phi$ where ϕ is the induced electric potential. Then, (2.9) takes the form

$$\vec{j} = \sigma_l(-\nabla\phi + \vec{u} \times \vec{B}_0) \quad (2.10)$$

which is known as the low- R_m approximation of Ohm's law for moving conductors [5]. Here, the induced electric potential ϕ ensures charge conservation $\nabla \cdot \vec{j} = 0$. Additionally, the contribution of $-\nabla\phi$ is typically in the same order of magnitude and in the

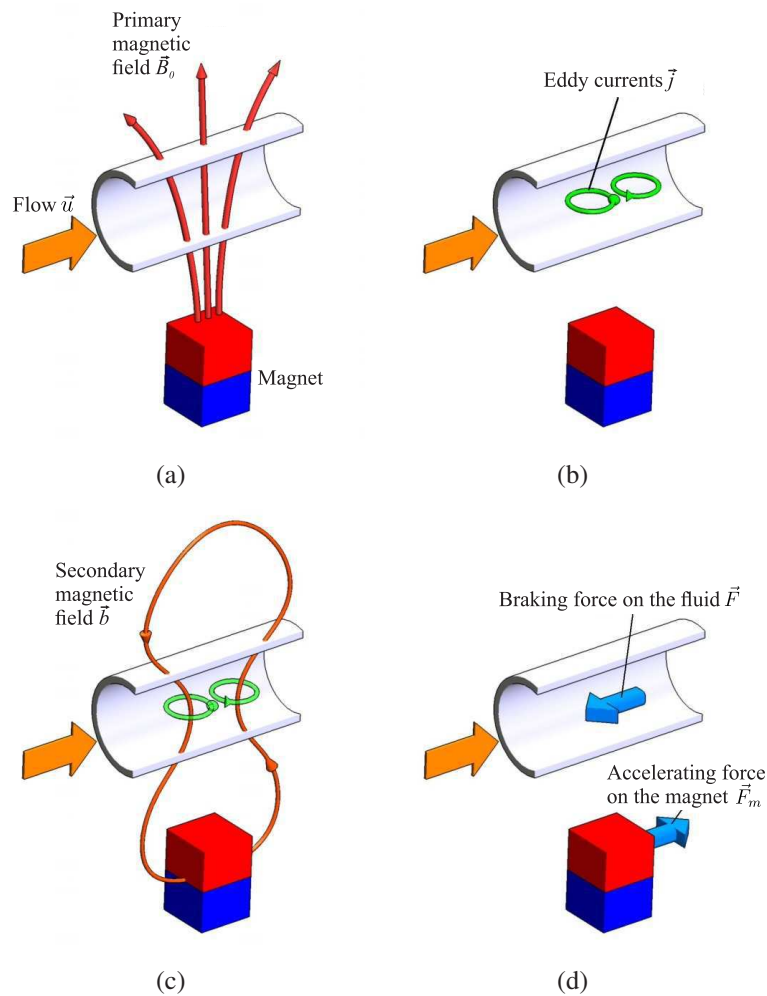


Figure 2.1: Liquid metal flow exposed to a static magnetic field generated by a permanent magnet. Flow induced eddy currents and a secondary magnetic field are generated inside the liquid giving rise to Lorentz forces acting on the flow and to an accelerating force of the same magnitude on the magnet. Courtesy of Institute for Thermodynamics and Fluid Mechanics, Technische Universität Ilmenau.

opposite direction to the $\vec{u} \times \vec{B}_0$ term. By taking the divergence of (2.10) with $\nabla \cdot \vec{j} = 0$, we get

$$\nabla^2 \phi = \nabla \cdot (\vec{u} \times \vec{B}_0). \quad (2.11)$$

The induced electric potential ϕ is obtained by solving (2.11) for insulating boundary conditions and \vec{j} is found by substituting ϕ in (2.10).

The interaction of \vec{j} with \vec{B}_0 is responsible for the generation of the Lorentz force density \vec{f} in the liquid according to the relation

$$\vec{f} = \vec{j} \times \vec{B}_0 \sim \sigma_l u B_0^2. \quad (2.12)$$

Finally, by integrating \vec{f} in the fluid domain, we obtain the total force \vec{F} and torque \vec{T} according to [57] as

$$\vec{F} = \int \vec{j} \times \vec{B}_0 dV, \quad \vec{T} = \int (\vec{r} - \vec{r}_0) \times \vec{f} dV, \quad (2.13, 2.14)$$

respectively. Here, \vec{r} is the position of every volume element of the fluid and \vec{r}_0 is a given reference point which could be either the center of the magnet or the center of the sensor's coordinate system which is defined by calibration. The total force \vec{F} is proportional to the electrical conductivity, to B_0^2 and to the flow rate or local velocity of the fluid. Due to Newton's third law, a force \vec{F}_m and a torque \vec{T}_m of the same magnitude but in opposite direction act on the source of the applied magnetic field which in our case are permanent magnets (figure 2.1(d)).

Then, by measuring \vec{F}_m , the flow rate of liquid metal \dot{V} is given by

$$\dot{V} = K_v \cdot |\vec{F}_m|, \quad (2.15)$$

where K_v is the calibration factor which is obtained experimentally. K_v is independent of the viscosity or density of the liquid, and depends only on the strength of the magnetic field, the electrical conductivity of the liquid metal and on the geometry of the channel in which the metal melt flows [27]. However, in the general case, the electrical conductivity depends on the temperature of the liquid metal, e.g. in molten aluminum the variation of σ_l is about 4% in the range 1150 K to 1250 K [31]. Additionally, the magnetic field of the permanent magnets depends also on the temperature [32]. For instance, it was found in [27] that the magnetic induction of NdFeB magnets decreased by 8.5% when the temperature of the magnets increased from 293 K to 363 K.

In LFV, the measuring device is called Lorentz force flowmeter (LFF) and is composed of a single or a group of permanent magnets which are connected to a force sensor. If the magnetic field lines penetrate the entire cross-section of the flow, the

LFF is able to measure the flow rate of electrically conducting liquids. Owing to the rapid decay of magnetic fields and by using magnets significantly smaller in comparison with the cross-section of the flow, a localized magnetic field distribution in the liquid metal is achieved. In this case, the Lorentz force is generated from a small portion of the fluid whose volume is located in the region near the wall adjacent to the magnet allowing a local velocity assessment. Due to its localized nature, this subsection of LFV is called local Lorentz force velocimetry (local LFV) and the system composed of the small-sized magnet altogether with the force sensor is called Local Lorentz Force Flowmeter (L2F2).

A quantitative approximation of the expected force and torque orthogonal to the magnetization of the magnet can be obtained analytically by assuming a semi-infinite conducting layer with velocity $u_x \vec{e}_x$. The magnetic field can be approximated by a magnetic dipole with magnetic dipole moment $m \vec{e}_z$ at a distance κ_{dip} away from the layer. Then, the force and torque acting on the dipole are in this case [58]

$$\vec{F}_m = \left(\frac{\mu_0^2 \sigma m^2}{128\pi} \right) \left(\frac{u_x}{\kappa_{dip}^3} \right) \vec{e}_x, \quad \vec{T}_m = - \left(\frac{\mu_0^2 \sigma m^2}{128\pi} \right) \left(\frac{u_x}{\kappa_{dip}^2} \right) \vec{e}_y. \quad (2.16, 2.17)$$

To conclude, Lorentz force velocimetry is based on the assumption that the back reaction of the induced forces acting on the flowing liquid is negligible, i.e. the flow is not affected by the magnetic field. This is known as the kinematic regime of LFV [18], where the interaction parameter N is much smaller than 1. This is the case for many applications of LFV in metallurgy characterized by turbulent flows at high Reynolds numbers. However, the assumption of $N \ll 1$ is not always totally fulfilled in the case of local LFV. As the magnets are here much closer to the wall, they may generate a strong localized magnetic field distribution in the liquid, and therefore, the probability of having finite values of N increases considerably. This situation will be discussed more in detail in section 5.6 and section 5.7, where a comparison between two magnet systems is done based on experiments and simulations in the framework of local LFV at a continuous caster model under low and finite values of N .

2.3 State of the art

LFV has been a subject of intensive academic research within the Research Training Group (RTG) "Lorentz force velocimetry and Lorentz force eddy current testing" at the Technische Universität Ilmenau. This RTG is financially supported by the Deutsche Forschungsgemeinschaft (DFG). This section gives an overview of the present state of the art regarding contactless flow rate and local velocity measurements of electrically

conducting liquids. It is classified in flow rate measurement using a LFF and local velocity assessment using a L2F2.

2.3.1 Flow rate measurement

The concept of flow rate measurement of hot liquid metals using a LFF has been successfully tested in industrial applications. For instance, a LFF was used to determine the flow rate of hot liquid aluminum at a secondary aluminum production facility [27, 34]. Here, the liquid aluminum has an electrical conductivity of about 3.01 MS/m and is transported by runners (open-channel flow) at an operating temperature of about 1053 K (780°C). In this case it is desirable to measure the mean velocity of the liquid metal for deducing the mass or volume-flux in order to monitor and control the production process. The LFF used for this task consists of two permanent magnet arrangements attached to an iron yoke, which closes the magnet circuit and increases the strength of the applied magnetic field.

One of the biggest challenges in open-channel flows is that the flow level of the liquid metal is fluctuating, and therefore, K_V cannot be considered constant as it depends on the level of the melt in the channel. For a successful implementation of the LFF

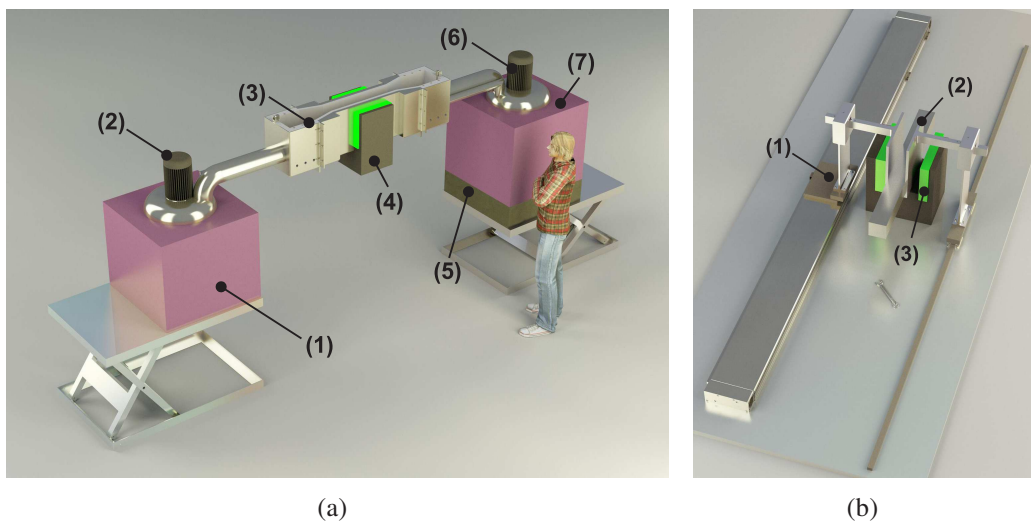


Figure 2.2: In the wet calibration facility LITINCA (a), liquid tin is melted in the first furnace (1) and pumped into the runner by a metal pump (2). The liquid tin flows through the runner (3) and is collected at the end by a second furnace (7) which sits on a weighting device (5). This device allows us to generate the cumulative mass signal during experiments which is afterwards compared with the signal of the LFF (4) that is located in the middle of the runner. Finally, the runner is tilted and the liquid metal pump (6) drives the molten tin back to the first furnace. On the other hand, in the dry calibration facility SOMECA (b), the liquid metal flow is modeled by solid bars (2) whose cross-section and electrical conductivity are known. They are moved by a linear motor (1) at a controlled velocity through the magnetic field lines produced by the LFF (3). Courtesy of Institute for Thermodynamics and Fluid Mechanics, Technische Universität Ilmenau.

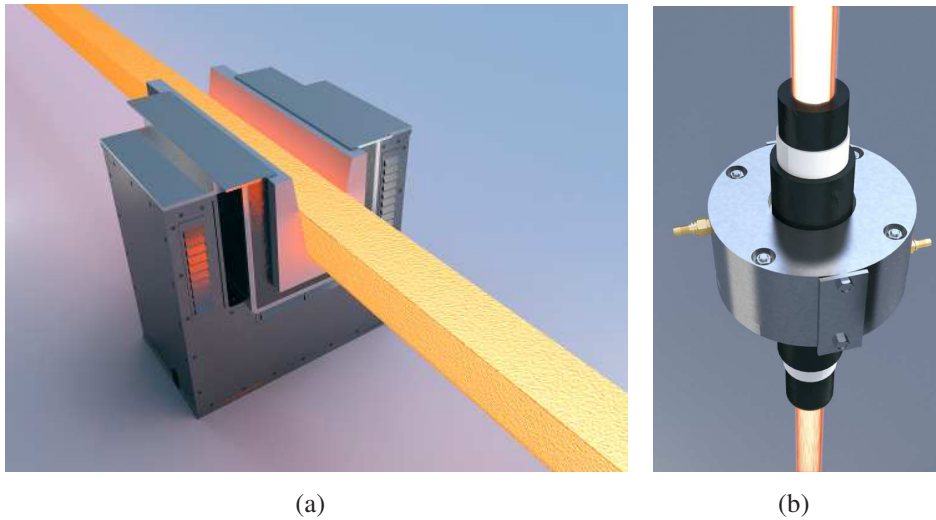


Figure 2.3: LFF prototypes for open-channel (a) and pipe flows (b). The yoke with the permanent magnets and the measuring device are enclosed in a housing with a cooling system [26].

in application, one needs to determine K_v by either performing numerical simulations [66] or by using calibration facilities [33, 35]. Dry and wet calibration procedures have been developed in order to determine K_v under laboratory conditions. Two of these calibration facilities are SOMECA (Solid METal CALibration) and LITINCA (LIquid TIN CALibration) which are shown in figure 2.2. An example of wet calibration can be found in [20].

In [70, 69], a LFF has been experimentally tested for pipe flows in continuous casting of steel ($\sigma_l \approx 0.25 \text{ MS/m}$). This prototype was constructed for controlling the level of the mold of a slab caster. In this case, the LFF had to perform dynamic force measurements with a response time less than 100 ms. However, the actual response time of the final LFF was about $\approx 220 \text{ ms}$ and suggestions for its improvement were given. The magnet system in the LFF was a FEM-optimized Halbach cylinder composed by 16 trapezoidal segments. It should be pointed out that, in this case as well as in many industrial applications, the LFF has to be enclosed in e.g. an air-cooled housing (figure 2.3) that maintains the temperature of the magnets under its Curie temperature. The housing also protects the LFF from possible collisions with ferromagnetic materials in the environment attracted by the strong magnetic field. To summarize, these experiments and industrial tests (including the ones with liquid aluminum) have validated the feasibility of LFF for measuring the flow rate of hot liquid metals whose conductivity is in the order of magnitude of about 1 MS/m .

In [67], LFV has been successfully applied for measuring the flow rate of weakly conducting fluids like electrolytes, whose conductivity is the same order of magnitude as molten glass ($\sigma_l \approx 1 \text{ S/m}$) [1, 41]. The magnets are placed at each side of a rectangu-

2. Lorentz force velocimetry

lar glass duct through which salty water flows. The small Lorentz forces acting on the magnets were measured using a pendulum-like system. When the electrolyte starts to flow, the induced Lorentz force moves slightly the magnets, which hang from tungsten wires. This deflection is measured by a sensitive optical interferometer which, after calibration [68], gives the magnitude of the Lorentz force in the order of $\approx 17\mu\text{N}$ for a mean velocity of 5.7 m/s and $\sigma_l = 4\text{ S/m}$. The sensitivity of the force measurement was then later improved using a direct force compensation scheme. In this case, the weight of the magnets is compensated allowing gravity-free force measurements using a state-of-the-art electromagnetic force compensation weighting balance (EMFC). This EMFC has a complex inner mechanical construction with flexure and parallel spring beams allowing flow rate measurements of even tap water ($\sigma_l \approx 0.06\text{ S/m}$) [63].

Another important application of LFF for flow rate measurements is Lorentz torque velocimetry (LTV) [7]. Here, it was demonstrated the feasibility of both pumping and flow rate measurement by using a torque sensor mounted on the shaft of an electromagnetic pump (see figure 2.4(a)). The electromagnetic pump consists of two rotating steel disks having embedded permanent magnets with alternating poles. The torque sensor measures the torque due to the induced Lorentz force in the liquid which is then converted to a flow rate value. The first stage of calibration was done with aluminum plates between the disk gaps and the second stage with GaInSn using a Vives probe.

To summarize, the LFF concept has been extensively tested with different electrically conducting liquids, hot or at room temperature, covering a wide range of σ_l . However, the LFF has the disadvantage that K_v has to be obtained *a priori* in order to assess correctly the magnitude of the flow rate in application. The definition of K_v increases in complexity for open-channels flows that exhibit strong flow-level and

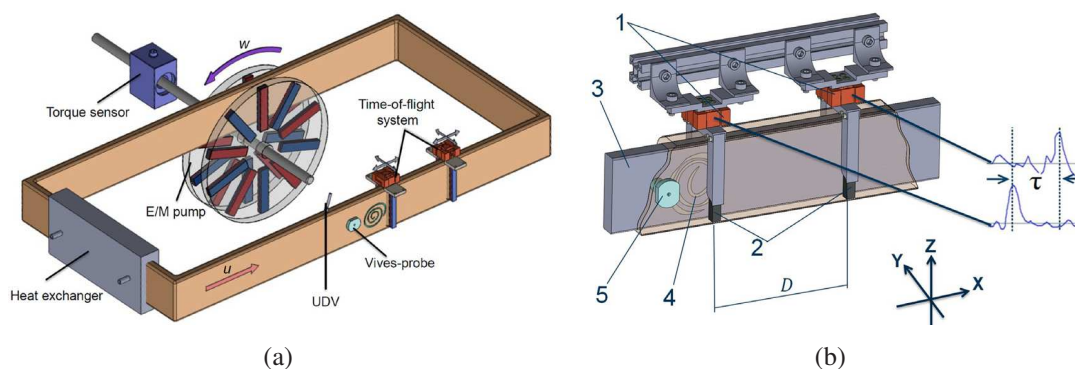


Figure 2.4: (a) Set-up for investigating LTV and time-of-flight LFV [8]. (b) Scheme of time-of-flight LFV. Force signal perturbations are induced by passing vortices which are shown as peaks at the presented signals diagram. The velocity of liquid metal can be obtained as the relation of distance between sensors per time between the perturbations. (D -distance between flowmeters, τ -time delay between perturbations, 1-force sensors, 2-permanent magnets, 3-liquid metal, 4-a vortex, 5-Vives-probe) [8].

temperature fluctuations of the liquid and/or permanent magnets. Hence, a new LFF concept was proposed that uses two LFF separated at a given distance from each other. The Lorentz force signals of each LFF are recorded in time, for which the auto- and cross-correlation can be used to determine the flow rate of the liquid metal. The reliability of this technique, the so called time-of-flight LFV, was numerically investigated in [65] with synthetic and realistic 3-dimensional turbulent flows with and without the effect of the magnetic field on the flow (kinematic and dynamic simulations). Time-of-flight LFV was then successfully applied for the flow rate measurement of GaInSn in eutectic composition having a cylindrical obstacle [24] and a Vives-probe [8] as vortex generator. However, the signal-to-noise ratio is still low for practical applications. Further improvements in both measuring system and signal processing are needed.

2.3.2 Local Lorentz force velocimetry

Figure 2.5 shows a simplified sketch of the main components of a local LFV set-up. With this set-up, Heinicke [16] started the experimental studies of local LFV focusing mainly on a 10mm cubic permanent magnet attached to a 1-D interference optical force sensor (IOFS). The system composed of the IOFS and a magnet system will be referred in this thesis as the 1D-L2F2. Thus, this 1D-L2F2 can measure just one component of the force acting on the magnet at a time. As the dimensions of the permanent magnet are significantly smaller than the flow under investigation (GaInSn in eutectic

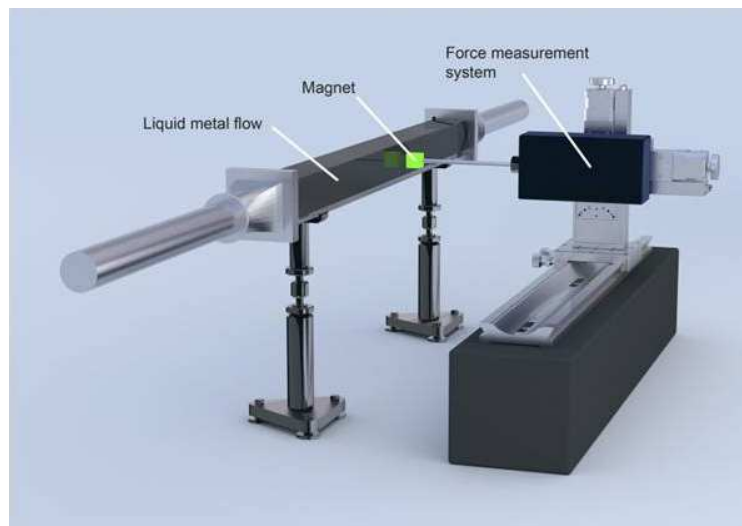


Figure 2.5: Simplified sketch of a local LFV set-up. A permanent magnet connected to a force measurement system, the so-called 1D-L2F2, is placed besides a channel in which liquid metal flows. The permanent magnet is smaller than the cross-section of the flow producing a localized magnetic field distribution in the liquid metal. The 1D-L2F2 is usually mounted on a granite stone in order to avoid unwanted vibrations from the duct. Courtesy of Institute for Thermodynamics and Fluid Mechanics, Technische Universität Ilmenau.

composition), the 1D-L2F2 was capable to identify cylindrical obstacles in a square duct (figure 2.6(a)) as well as the resulting modified structures based on the stream-wise force measurements [17]. These local-velocity predictions based on the force profiles were validated with UDV measurements. By comparing the peaks of the UDV and the force profiles, whose peaks were both separated by 3 cm, it was concluded that the spatial resolution of the 1D-L2F2 was 3 cm with a 1 cm cubic magnet. Chapter 4 gives a more detailed description of the sensor and the experimental set-up, whereby the influence of the geometry of different magnet systems on the streamwise Lorentz force is investigated.

This 1D-L2F2 was later used to reconstruct a 2D velocity distribution of liquid metal in the vicinity of the wall of a confined vessel [19]. The working fluid is GaInSn in eutectic composition and the flow is driven by a propeller on the top of the vessel, for which downward and upward pumping were considered. A sketch of the set-up is depicted in figure 2.6(b). For a 2D force measurement using a 1D force sensor, the 1D-L2F2 has to measure first one component of the force along the measuring grid, and then should be rotated 90 degrees for obtaining the second perpendicular force component. Hence, there is the implicit assumption that the flow regime in the vessel is steady, allowing us to perform a correct reconstruction of the 2D velocity field based on force distributions measured at different times. It was concluded that the 1D-L2F2 can reproduce well the vertical velocity distribution of GaInSn at least qualitatively. It was also found that the 1D-L2F2 responds to temporal changes in the flow in the order of 1 Hz. However, in local LFV it is not only important the time variation of the velocity field itself, but also the type of velocity distribution in the portion of the fluid

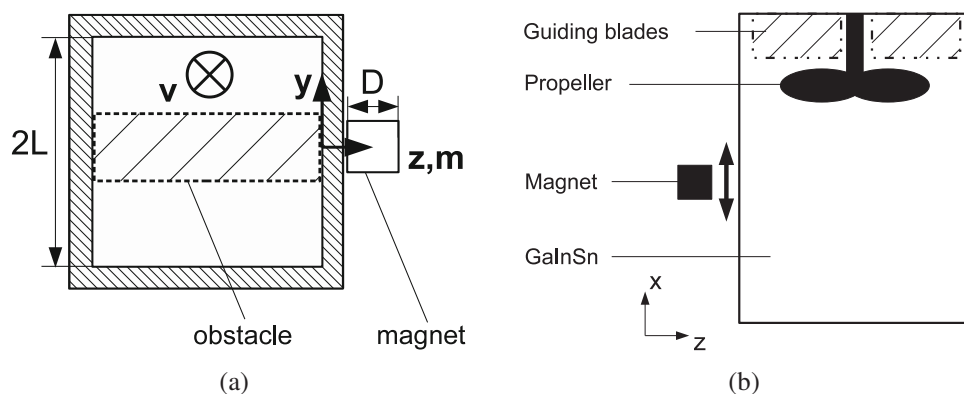


Figure 2.6: (a) The fluid flows in a straight square duct with mean velocity v in the x -direction. The cross-section of the duct is $5\text{ cm} \times 5\text{ cm}$, in which the characteristic length scale is the half-width $L = 2.5\text{ cm}$. The cubic magnet ($D = 1\text{ cm}$) is placed beside the duct, (almost) touching the 5 mm plexiglass wall [17]. (b) Sketch of confined cylindrical vessel experiment. The propeller and the guiding blades are attached to the bottom of the lid. The L2F2 uses a 1 cm cubic magnet for measuring the vertical and horizontal force components. The measured force profiles cover the entire height of the liquid metal in the vessel [19].

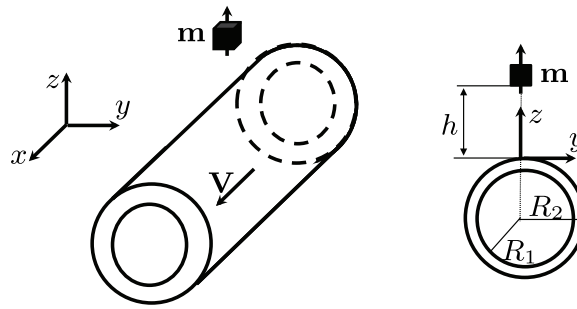


Figure 2.7: Sketch of the considered problem regarding local LFV and conducting walls. A permanent magnet m is placed next to a pipe in which GaInSn flows in turbulent regime at an average velocity v . Here, conducting (brass and copper) and non-conducting (PVC) walls were considered in both experiments and simulations [25].

volume spanned by the magnetic field generated by the small-size magnet. Chapter 5 will discuss the influence of different types of velocity distributions on the force and torque components acting on different magnet systems.

In [25], the 1D-L2F2 was used to investigate the effect of conducting walls on the Lorentz force acting on a permanent magnet placed near a cylindrical-pipe flow. A sketch of the considered problem is depicted in figure 2.7. A numerical model and experimental results were reported showing good agreement except for lower air gaps between the surface of the magnet and the surface of the tube. In the case of the numerical model, the analytic magnetic field distribution of a dipole and a rectangular magnet were both considered. Here, it was found that the Lorentz force in experiments and in the numerical model increased when the electrical conductivity of the wall increased. According to [25], this increase could be attributed to the eddy currents flowing through the conducting wall next to the magnet.

To summarize, local LFV has proven to give a qualitative assessment of the velocity field of a liquid metal flow in the area near the wall next to the magnet. However, important open questions still remain unsolved like the definition of the fraction of the fluid that contributes mainly to the measurable force and its dependence on different velocity distributions. Additionally, a better understanding of the effect of conducting walls in LFV has to be deeply analyzed for optimization studies in future applications.

Chapter 3

Electric potential in Lorentz force velocimetry

This chapter focuses on the effect of the induced electric potential in Lorentz force velocimetry by considering two different scenarios: conducting walls of finite thickness and aspect-ratio variation of the cross-section of the flow. It has been observed in previous and in the present experiments that the measurable Lorentz force is stronger when either the electrical conductivity of the wall increases or the aspect ratio of the cross-section of the flow varies, i.e. when the ratio of the height h to the width w of the duct increases. The first case is studied for a turbulent flow inside a pipe (figure 3.1(a)), and the second one for a moving solid conductor with rectangular cross-section (figure 3.1(b)). Based on numerical models of the experiments, it is shown that the force component generated by the electric potential is always in the opposite direction to the total Lorentz force. This component is sensitive to the electrical conductivity of the walls, being perfectly conducting and perfectly insulating the two limited cases.

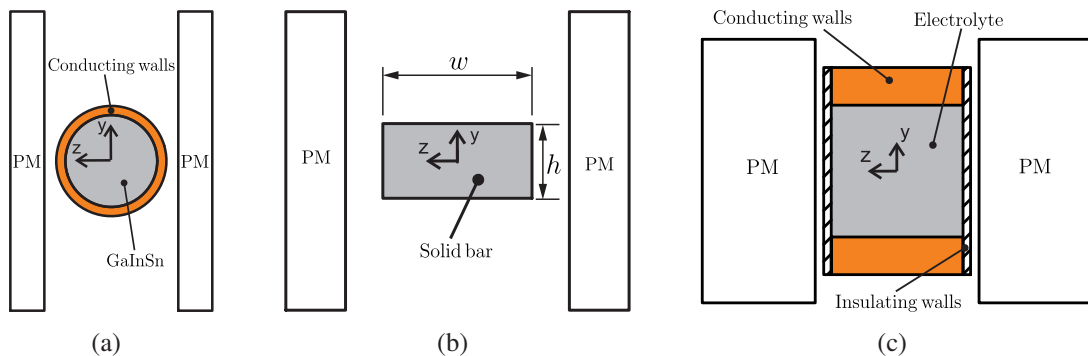


Figure 3.1: Simplified sketches for investigating wall conductivity effect (a) and the aspect ratio variation of the cross-section of the flow (b) on the Lorentz force. (c) Sketch of LFV in electrolytes with conducting side walls and insulating Hartmann walls. In all cases, permanent magnets (PM) are placed on each side of the tube/bar/duct. Their magnetization points into the z -direction.

Additionally, it is also sensitive to the aspect ratio of the cross-section of the flow. The measurable Lorentz force increases significantly when this force component originating from the induced electric potential decreases. At the end of this chapter, a proposal is presented using conducting side walls (parallel to the magnetization of the magnets and located at the top and bottom of the duct) and insulating Hartmann walls (perpendicular to the magnetization of the magnets). For this configuration (see figure 3.1(c)), the expected increase of the total Lorentz force in electrolytes is obtained based on the experimental results in [67], where the flow rate of salt water was measured. In the particular case of electrolytes, the ratio of conductivities between the liquid and the wall can be effectively infinite by using copper or aluminum walls.

The main results in this chapter will be published in the first reference of the author's publication list (Appendix: A List of publications). The structure of this chapter is organized as follows: section 3.1 focuses on the effect of wall conductivity on the Lorentz force. It starts with the results at the experimental facility GaInSn loop followed by an analytical model of the general case regarding perfectly conducting and insulating walls. Afterwards, the numerical model of the experiments is described presenting the corresponding numerical results. Then, section 3.2 will examine the effect of the aspect ratio variation of the cross-section of the flow on the Lorentz force. It starts with the experiments at SOMECA followed by the numerical results. Section 3.3 analyses numerically the effect of top and bottom conducting side walls in the case of electrolytes giving an estimate of the expected increase of the total Lorentz force. Finally, section 3.4 summarizes the main conclusions.

3.1 Wall conductivity effect

As mentioned previously in section 2.3.2, the effect on the total Lorentz force caused by different electrical conductivities of the wall was studied by Kazak using a small-size magnet [25]. The experiments were done at the GaInSn loop (figure 3.2(a)) and a numerical model was developed. In both cases, the magnitude of the simulated/measured Lorentz force was stronger, when the ratio of the conductivity of the wall σ_w to the conductivity of the liquid σ_l increased. However, the analysis provided by Kazak did not take into account the limiting case where σ_w tends to infinity or a deeper explanation of the cause of this increase. In this section, the considered problem is analytically and numerically analyzed for both limiting cases, for which the ratio of conductivities tends to infinity (perfectly conducting) or to zero (perfectly insulating). Here, a LFF composed of two permanent magnets is used as measuring device, contrary to the small-size magnet used by Kazak. In this way the results can

be extended to LFF in general, e.g. to the application of low conducting liquids like electrolytes (section 3.3).

3.1.1 Experimental set-up and results

The effect of wall conductivity on the measured Lorentz force is experimentally investigated at the GaInSn loop available at Helmholtz-Zentrum Dresden-Rossendorf (HZDR). A photo of the set-up is depicted in figure 3.2(a). It is a liquid metal loop composed of a stainless steel section connected to 3 different tubes made from PVC, copper and brass. They share the same inner diameter $d = 27$ mm, wall thickness $t = 2.5$ mm and length $l = 400$ mm. The electrical conductivities of the brass and copper tubes are 13.7 MS/m and 47.1 MS/m, respectively. These two quantities were measured using SIGMATEST 2.069 [23]. At the beginning of the tubes there is a valve that controls the flow of GaInSn, whose electrical conductivity is $3.3 \cdot 10^6 \pm 3 \cdot 10^4$ S/m at 20°C [37]. The flow is driven by an electromagnetic pump from the stainless steel tube passing first through a commercial inductive flowmeter and then to the corresponding valve-controlled tube. The average velocity \overline{u}_x in the experiments is in the range of $0 \leq \overline{u}_x \leq 1$ m/s in steps of 0.2 m/s, which corresponds to a range of Reynolds numbers of $0 \leq Re \leq 7.9 \cdot 10^4$.

The LFF in this case consists of two permanent magnets (NdFeB, N40) with dimensions $88 \text{ mm} \times 24 \text{ mm} \times 10 \text{ mm}$, which are mounted on a yoke made of aluminum.

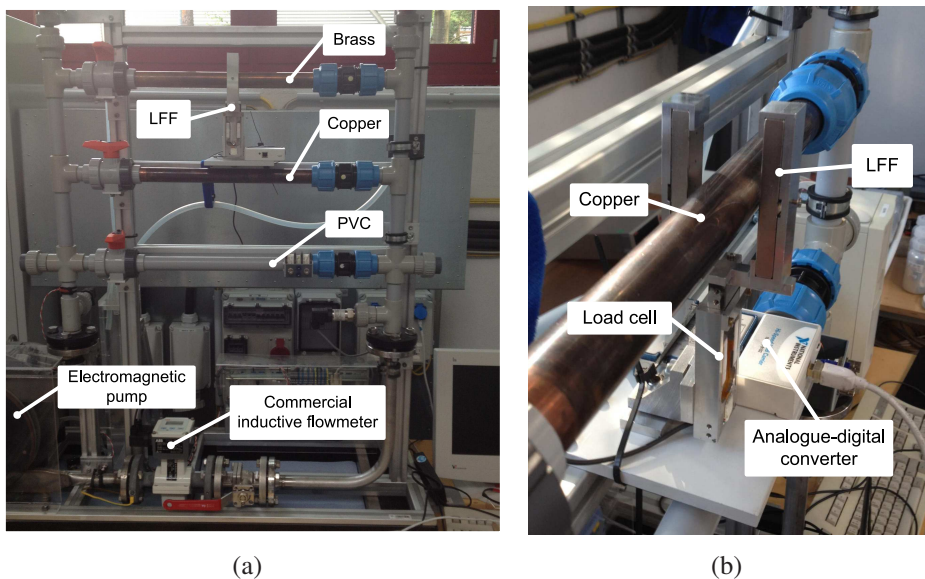


Figure 3.2: (a) GaInSn loop facility with electromagnetic pump, commercial inductive flowmeter (COPA-XL DN25 from ABB) and LFF. (b) Close-up of the set-up including the LFF and the copper tube. The tube is placed in the middle of the permanent magnets maintaining an air gap of about 3.9 mm at each side.

3. Electric potential in Lorentz force velocimetry

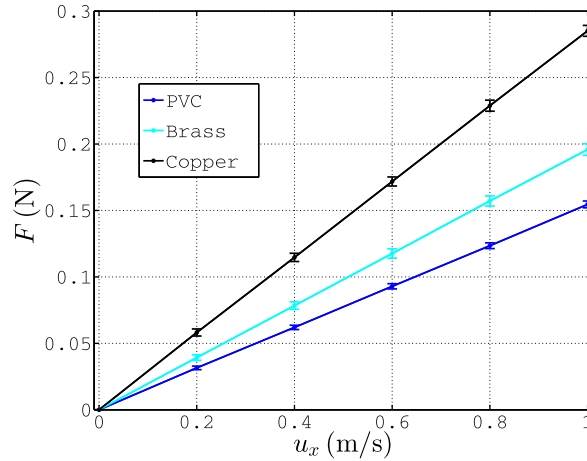


Figure 3.3: Dependence of the Lorentz force magnitude on the average velocity of the liquid metal for different wall conductivities. The error bars represent the standard deviation of the measurements at different positions along the tube (inlet, middle, and outlet) and for pumping in positive and in negative direction.

The yoke is fixed to a load cell that measures the total streamwise force that acts on the magnets. The load cell is connected to an analogue-to-digital converter. The results of the force measurements show that the Lorentz force increased when the electrical conductivity of the wall also increased (figure 3.3). By using the brass and copper tubes, the force was about 1.3 and 1.9 times higher in comparison with the PVC tube, respectively. The detail explanation of this effect can be found in section 3.1.4.

3.1.2 Analytic model

The analytical model in this section is the result of private communication with Thomas Boeck (TU Ilmenau). Here, based on perturbation theory, the two limiting cases of this system are analyzed: perfectly conducting ($\sigma_w/\sigma_l \gg 1$) and perfectly insulating ($\sigma_w/\sigma_l \ll 1$) walls. It is assumed in both cases the low- R_m approximation

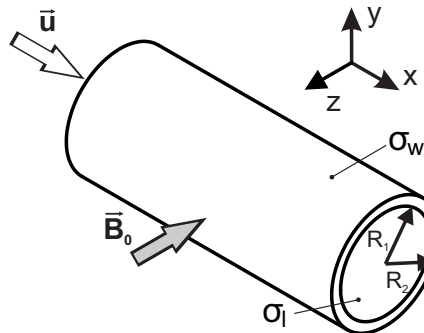


Figure 3.4: Sketch of the considered problem: liquid metal with conductivity σ_l flows with a constant velocity \vec{u} inside a circular pipe with conductivity σ_w . Orthogonal to the flow direction, an static magnetic field \vec{B}_0 is applied.

of Ohm's law and $N \ll 1$. The sketch of the considered problem is shown in figure 3.4.

3.1.2.1 Limiting case of infinite wall conductivity

According to figure 3.4, Ohm's law for the two regions, liquid metal and wall, read as

$$\vec{j}_l = \sigma_l(-\nabla\phi + \vec{u} \times \vec{B}_0), \quad \vec{j}_w = \sigma_w(-\nabla\phi), \quad (3.1, 3.2)$$

respectively. At the liquid-solid boundary, the electric potential ϕ and the normal current j_n are continuous. Now we define

$$\psi_l = \sigma_l\phi, \quad \psi_w = \sigma_w\phi. \quad (3.3, 3.4)$$

By taking the divergence of (3.1) and (3.2), where $\nabla \cdot \vec{j} = 0$ due to charge conservation, we obtain

$$\nabla^2\psi_l = \nabla \cdot (\sigma_l\vec{u} \times \vec{B}_0), \quad \nabla^2\psi_w = 0. \quad (3.5, 3.6)$$

Here, (3.5) is defined in cylindrical coordinates in the region $0 \leq r \leq R_1$ and (3.6) in $R_1 \leq r \leq R_2$. Moreover, at $r = R_1$, the normal current that leaves the liquid $j_{n,l}$ and the normal current that enters the wall $j_{n,w}$ are

$$j_{n,l} = -\frac{\partial\psi_l}{\partial r}, \quad j_{n,w} = -\frac{\partial\psi_w}{\partial r}, \quad (3.7, 3.8)$$

respectively. As $j_{n,l} = j_{n,w}$, we obtain

$$\left. \frac{\partial\psi_l}{\partial r} \right|_{r=R_1} = \left. \frac{\partial\psi_w}{\partial r} \right|_{r=R_1}. \quad (3.9)$$

Since the electrical potential ϕ is continuous at $r = R_1$, we also find using (3.3, 3.4) that

$$\psi_l = \frac{\sigma_l}{\sigma_w}\psi_w. \quad (3.10)$$

Now let $\varepsilon = \frac{\sigma_l}{\sigma_w} \ll 1$. In this case we can express ψ_l as

$$\psi_l = \varepsilon\psi_w \quad (3.11)$$

at $r = R_1$. At the outer boundary $r = R_2$, we have an insulating wall condition, i.e.

$$\left. \frac{\partial\psi_w}{\partial r} \right|_{R_2} = 0. \quad (3.12)$$

3. Electric potential in Lorentz force velocimetry

Here (3.9), (3.11) and (3.12), provide proper boundary conditions for (3.5, 3.6). We can now make a regular series expansion in ε [2]:

$$\psi_l = \sum_{i=0}^{\infty} \varepsilon^i \psi_l^{(i)}, \quad \psi_w = \sum_{i=0}^{\infty} \varepsilon^i \psi_w^{(i)}. \quad (3.13, 3.14)$$

The leading order problem (ε^0) is therefore

$$\nabla^2 \psi_l^{(0)} = \nabla \cdot (\sigma_l \vec{u} \times \vec{B}_0), \quad \nabla^2 \psi_w^{(0)} = 0, \quad (3.15, 3.16)$$

$$\left. \frac{\partial \psi_l^{(0)}}{\partial r} \right|_{R_1} = \left. \frac{\partial \psi_w^{(0)}}{\partial r} \right|_{R_1}, \quad \left. \frac{\partial \psi_w^{(0)}}{\partial r} \right|_{R_2} = 0, \quad \psi_l^{(0)}|_{R_1} = 0. \quad (3.17, 3.18, 3.19)$$

For the order ε^1 :

$$\nabla^2 \psi_l^{(1)} = 0, \quad \nabla^2 \psi_w^{(1)} = 0, \quad (3.20, 3.21)$$

$$\left. \frac{\partial \psi_l^{(1)}}{\partial r} \right|_{R_1} = \left. \frac{\partial \psi_w^{(1)}}{\partial r} \right|_{R_1}, \quad \left. \frac{\partial \psi_w^{(1)}}{\partial r} \right|_{R_2} = 0, \quad \psi_l^{(1)}|_{R_1} = \psi_w^{(0)}|_{R_1}. \quad (3.22, 3.23, 3.24)$$

The equations are the same for higher orders in ε . The eddy currents in the liquid are therefore

$$\vec{j}_l = - \sum_{i=0}^{\infty} \varepsilon^i \nabla \psi_l^{(i)} + \sigma_l \vec{u} \times \vec{B}_0. \quad (3.25)$$

By substituting (3.25) in (2.13), the total Lorentz force in the liquid is

$$\vec{F}_l = \vec{F}_l^{(0)} + \varepsilon \vec{F}_l^{(1)} + \dots \quad (3.26)$$

It follows that the force should tend to a finite asymptotic limit when $\sigma_w \rightarrow \infty$. The first correction is linear in ε , i.e. $\sim 1/\sigma_w$. This behavior should be found in a full numerical solution with very high values of $\sigma_w \gg \sigma_l$. We now compute the leading term:

$$\vec{F}_l^{(0)} = \int_{r \leq R_1} (-\nabla \psi_l^{(0)} \times \vec{B}_0) dV + \int_{r \leq R_1} \sigma_l (\vec{u} \times \vec{B}_0) \times \vec{B}_0 dV. \quad (3.27)$$

In order to solve the first term on the right side of (3.27), we define \vec{B}_0 as the gradient of the magnetic scalar potential χ . This is the case for simply-connected current-free regions according to [15] where $\nabla^2 \chi = 0$. Then, the first term on the right side of (3.27) is

$$\int \nabla \psi_l^{(0)} \times \nabla \chi \, dV = \int \nabla \times (\psi_l^{(0)} \nabla \chi) \, dV - \int \psi_l^{(0)} \nabla \times \nabla \chi \, dV. \quad (3.28)$$

Since the curl of a gradient is always zero, the second term on the right side of (3.28) vanishes. Now, based on the identity $\oint_S (\vec{n} \times \vec{A}) \, dS = \int_V (\nabla \times \vec{A}) \, dV$, the left term on the right side of (3.28) turns into the integral

$$\psi_l^{(0)} \oint_S \vec{n} \times \nabla \chi \, dS \quad (3.29)$$

over the boundary liquid-wall where $\psi_l^{(0)}|_{R_1} = 0$ as mentioned above. This means that when the walls are infinitely conducting, the total Lorentz force in the liquid is

$$\vec{F}_l^{(0)} = \int_{r \leq R_1} \sigma_l (\vec{u} \times \vec{B}_0) \times \vec{B}_0 \, dV, \quad (3.30)$$

i.e. the first term of (3.27) vanishes. This term originating from the electric potential is sensitive to the boundary conditions and influences the distribution of the currents in the liquid. It can thus be concluded that this component of the Lorentz force in the fluid depends on the electrical resistivity of the wall. According to the numerical simulations presented in the following section for insulating and low ε , this force component is always pointing in the opposite direction to the $\vec{u} \times \vec{B}_0$ term causing a considerable decrease of the total force in the liquid. This same effect can also be seen by changing the aspect ratio of the cross-section of the flow as shown in section 3.2. However, in the case of conducting walls, we have to keep in mind that as the eddy currents are flowing through the wall too, they also generate a force

$$\vec{F}_w = \int (\vec{j}_w \times \vec{B}_0) \, dV = \int \sigma_w (-\nabla \phi \times \vec{B}_0) \, dV \quad (3.31)$$

in the region $R_1 \leq r \leq R_2$ that contributes to the total Lorentz force \vec{F} according to $\vec{F} = \vec{F}_l + \vec{F}_w$.

3.1.2.2 Limiting case of insulating walls

In this section, the second limiting case of the system is investigated in which $1/\varepsilon \ll 1$. Let us define $\varepsilon_w = \sigma_w/\sigma_l$, i.e $\varepsilon_w = 1/\varepsilon$. According to section 3.1.2.1, ϕ is continuous at $r = R_1$ so

$$\phi_l|_{R_1} = \phi_w|_{R_1}. \quad (3.32)$$

The divergence of (3.1) and (3.2) is in this case

$$\nabla^2 \phi_l = \nabla \cdot (\vec{u} \times \vec{B}_0), \quad \nabla^2 \phi_w = 0. \quad (3.33, 3.34)$$

As described in the previous section, the normal current at the boundary liquid-wall j_n is continuous so

$$\sigma_l \frac{\partial \phi_l}{\partial r} \Big|_{R_1} = \sigma_w \frac{\partial \phi_w}{\partial r} \Big|_{R_1} \quad \text{or} \quad \frac{\partial \phi_l}{\partial r} \Big|_{R_1} = \varepsilon_w \frac{\partial \phi_w}{\partial r} \Big|_{R_1}. \quad (3.35, 3.36)$$

By making a regular series expansion of ϕ_l and ϕ_w in ε_w analogous to section 3.1.2.1, the leading problem (ε_w^0) in this case reads as

$$\nabla^2 \phi_l^{(0)} = \nabla \cdot (\vec{u} \times \vec{B}_0), \quad \nabla^2 \phi_w^{(0)} = 0, \quad (3.37, 3.38)$$

$$\frac{\partial \phi_l^{(0)}}{\partial r} \Big|_{R_1} = 0, \quad \frac{\partial \phi_w^{(0)}}{\partial r} \Big|_{R_2} = 0, \quad \phi_l^{(0)} \Big|_{R_1} = \phi_w^{(0)} \Big|_{R_1}. \quad (3.39, 3.40, 3.41)$$

For the order ε^1 we obtain

$$\nabla^2 \phi_l^{(1)} = 0, \quad \nabla^2 \phi_w^{(1)} = 0, \quad (3.42, 3.43)$$

$$\frac{\partial \phi_l^{(1)}}{\partial r} = \frac{\partial \phi_w^{(0)}}{\partial r} \Big|_{R_1}, \quad \frac{\partial \phi_w^{(1)}}{\partial r} \Big|_{R_2} = 0, \quad \phi_l^{(1)} \Big|_{R_1} = \phi_w^{(1)} \Big|_{R_1}. \quad (3.44, 3.45, 3.46)$$

The equations are the same for higher orders of ε_w . The eddy currents in the wall according to (3.2) are therefore

$$\vec{j}_w = -\sigma_w \left(\sum_{i=0}^{\infty} \varepsilon_w^i \nabla \phi_w^{(i)} \right). \quad (3.47)$$

By substituting (3.47) in (3.31), the total Lorentz force in the wall is

$$\vec{F}_w = \int \varepsilon_w \left(-\sigma_l \sum_{i=0}^{\infty} \varepsilon_w^i \nabla \phi_w^{(i)} \times \vec{B}_0 \right) dV, \quad (3.48)$$

i.e.

$$\vec{F}_w = \varepsilon_w \vec{F}_w^{(0)} + \varepsilon_w^2 \vec{F}_w^{(1)} + \dots \quad (3.49)$$

in the region $R_1 \leq r \leq R_2$. Analogous to (3.26), it follows that the force in the wall also tends to zero when $\sigma_w \rightarrow 0$. Since σ_l is assumed fixed, the force in the wall has a leading term proportional to ε_w , i.e. $\sim \sigma_w$.

3.1.3 Numerical model

The numerical model is depicted in figure 3.5(a) and is based on the experiments at GaInSn loop from section 3.1.1. In this case, ϵ_w will be gradually increased starting from insulating walls ($\epsilon_w \ll 1$), passing through brass ($\sigma_w = 13.7 \text{ MS/m}$) and copper ($\sigma_w = 47.1 \text{ MS/m}$), until reaching the asymptotic limit of F_l for perfectly conducting walls ($\epsilon_w \gg 1$) according to the analytical model from section 3.1.2.1. For every value of σ_w , the induced electric potential ϕ is obtained by solving simultaneously (3.5) and (3.6) using the PDE Module in the commercial FEM software COMSOL Multiphysics. Insulating boundary conditions are applied ($j_n = 0$) at $\vec{r} = R_2$ as well as at the outlet and inlet of the tube. The tube is sufficiently long in order to avoid the effect of both

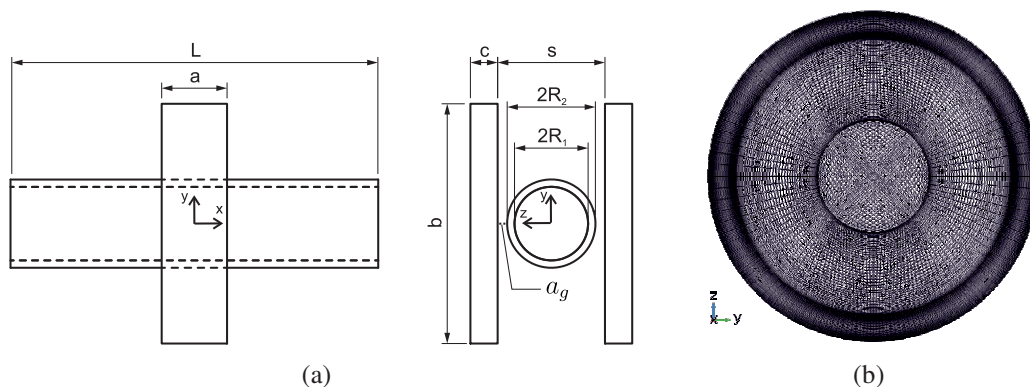


Figure 3.5: (a) Sketch of the considered problem: GaInSn with conductivity σ_l flows through a pipe with conductivity σ_w and thickness $R_2 - R_1$. Two permanent magnets are placed at each side of the tube at a distance s leaving an air gap a_g between the surface of the magnet and the surface of the tube. Their magnetization M_z points into \vec{e}_z and their center is placed at $x = 0$, $y = 0$, $z = \pm(R_2 + a_g + c/2)$. (b) Cross-section of the structure of the mesh for $N_a = 100$, $N_l = 100$, $N_r = 50$.

Table 3.1: Geometry parameters and material properties of GaInSn and wall.

Parameter	Value
Kinematic viscosity ν	$3.4 \cdot 10^{-7} \text{ m}^2/\text{s}$
Elec. cond. liquid σ_l	$3.3 \cdot 10^6 \text{ S/m}$
Elec. cond. wall σ_w	$10^{-6} \dots 10^{15} \text{ S/m}$
Pipe inner radius R_1	13.5 mm
Wall thickness $R_2 - R_1$	2.5 mm
Pipe length L	$10R_1$
Distance magnets s	39.8 mm

Table 3.2: Parameters of the permanent magnets.

Parameter	Value
Size ($a \times b \times c$)	$24 \times 88 \times 10 \text{ mm}^3$
Material	NdFeB
Grade	N40
Remanent magnetization B_r	1.3 T
Magnetization density M_z	$1.034 \cdot 10^6 \text{ A/m}$

ends on the solution. A summary of the geometry and material properties is shown in table 3.1.

In order to have a complete specification of the problem, the velocity field \vec{u} as well as the applied magnetic field \vec{B}_0 have to be fixed in both liquid and wall. Like in the experiments, two rectangular permanent magnets are the source of \vec{B}_0 , whereby their magnetization is $\vec{M} = M_z \vec{e}_z$. Their properties are summarized in table 3.2. The magnetic field generated by a rectangular magnet can be represented by the expression $\vec{B}_0 = B_x \vec{e}_x + B_y \vec{e}_y + B_z \vec{e}_z$, where the components B_x , B_y and B_z can be obtained analytically [12]. As there are two rectangular magnets in the experimental set-up, \vec{B}_0 contains the contribution of both magnets according to the superposition principle of magnetic fields. The formulas for \vec{B}_0 are given in Appendix B as well as a general description of the numerical model, which is the basis of all simulations developed in this thesis.

In the case of the velocity field \vec{u} , a mixing-length formula can be employed as the flow regime in the tube is turbulent. Here, the fluctuations of the flow are not taken into consideration, i.e. \vec{u} is purely axial and depends only on the radius r . According to [46], the velocity field can be analytically determined as

$$u_x(r) = \frac{u_\tau}{\kappa_0} \ln \left(1 + \kappa_0 \frac{u_\tau R_1}{\nu} \frac{1}{2} \left(1 - \frac{r^2}{R_1^2} \right) \right), \quad (3.50)$$

where u_τ is defined as the friction velocity and $\kappa_0 = 0.42$ is the von Kármán constant. Here, u_τ is defined in such a way that the required mean velocity is obtained by integrating the velocity over the cross-section of the flow. The results of the numerical model are given for $\bar{u}_x = 1$ m/s having $u_\tau = 0.0768$ m/s.

Similar to [3, 25], the meshing across the liquid and the wall is composed of non-uniform second-order hexahedral elements that take into account the decay of the magnetic field with the distance in the radial, axial and azimuthal direction. There is a deformed mesh in the region defined by a circumference with radius $2R_1/5$ in order to have a structured mesh inside the liquid. It is also used as a starting line for the geometric progression of element size towards the outer radius. The structure of the non-uniform mesh is parameterized by the following variables: number of azimuthal N_a , radial N_r and axial N_l grid lines. It was observed that \vec{F} is more sensitive to N_a and N_r . In relation with grid convergence, for $N_a = 50$, $N_l = 50$, $N_r = 25$ in comparison with $N_a = 100$, $N_l = 100$, $N_r = 50$, the variation is $\approx 1\%$ for $\sigma_w = 47.1 \cdot 10^6$ S/m. The finer mesh defined by these last parameters (about $1.43 \cdot 10^6$ elements) was consistently used in all computations and its cross-section is shown in figure 3.5(b).

3.1.4 Numerical results

Before presenting the results regarding \vec{F} , we first consider the change of \vec{j} in the liquid and in the wall due to the progressive increase of σ_w . The eddy current distribution is of highest importance and every change will represent in either a positive or negative influence on \vec{F} . In this sense, the eddy currents stream lines of \vec{j} in the $x-y$ plane for insulating, copper and perfect conducting walls are plotted in figure 3.6. Here, it can be seen that the overall distribution of \vec{j} is affected by the conductivity of the wall. For example, the center of the main eddies is shifted from $x \approx \pm 0.02$ m to $x \approx \pm 0.03$ m for insulating (figure 3.6(a)) and copper walls (figure 3.6(b)), respectively. When ε_w is sufficiently high, the eddy currents in the liquid and in the wall do no longer change (figure 3.6(c)). Here, ϕ does not contribute to \vec{F}_l but $\vec{u} \times \vec{B}_0$ in agreement with the analytical model from section 3.1.2.1. In view of a better understanding

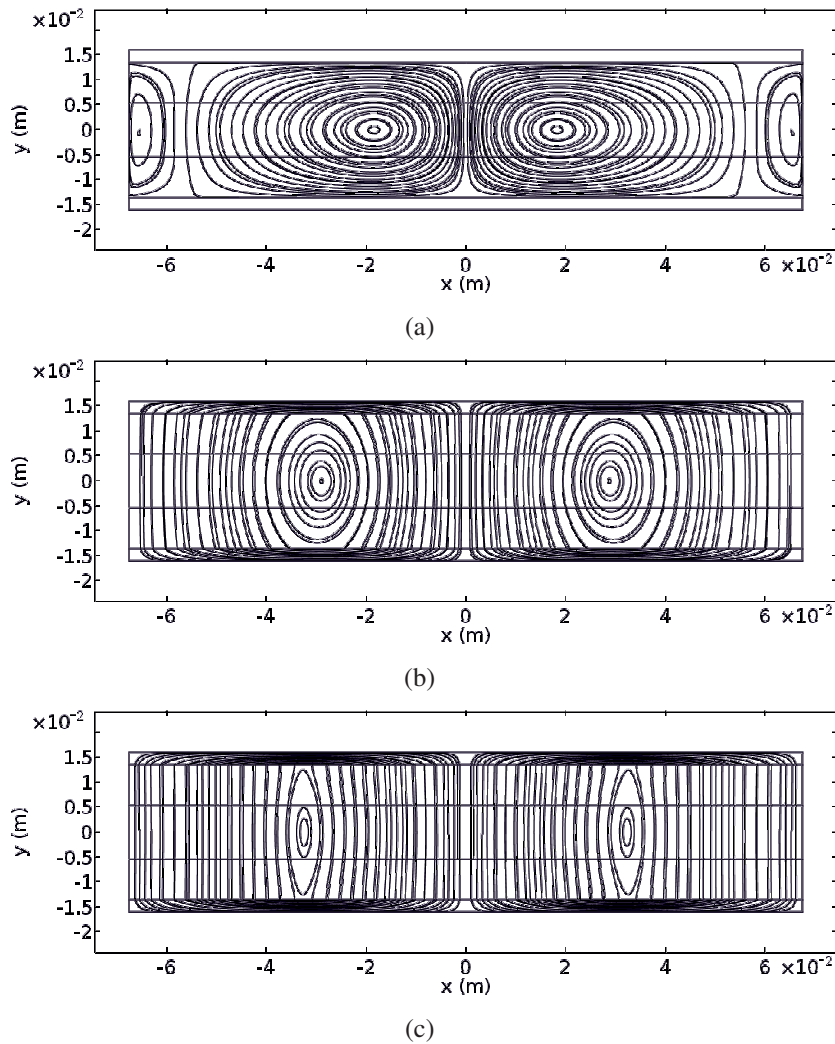


Figure 3.6: Eddy current streamlines in the liquid and in the wall in the $x-y$ plane for (a) insulating, (b) copper and (c) perfectly conducting walls.

3. Electric potential in Lorentz force velocimetry

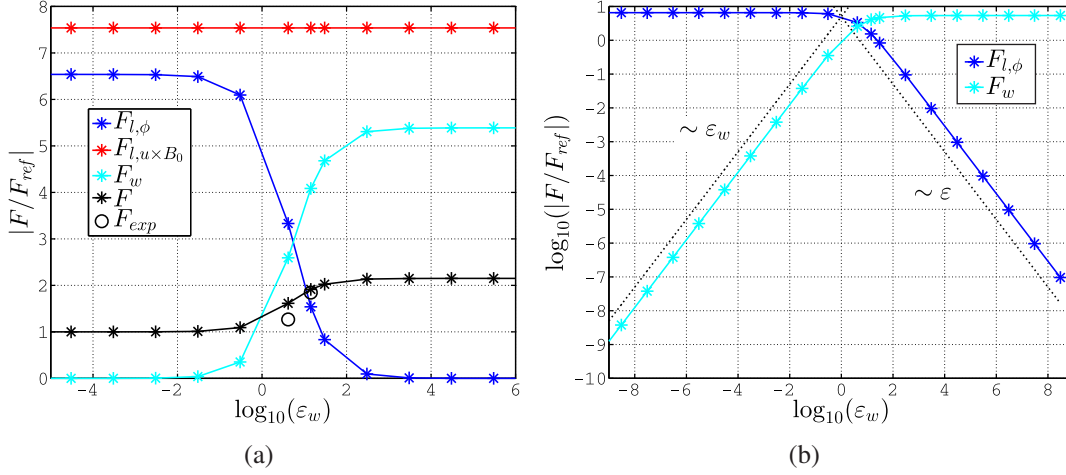


Figure 3.7: (a) $F_{l,\phi}$, $F_{l,u \times B_0}$, F_w , F and F_{exp} as a function of $\log_{10}(\epsilon_w)$ normalized by $|F_{ref}| = 0.146\text{N}$ and $|F_{PVC}| = 0.154\text{N}$ for the numerical and experimental results, respectively. The values of F_{exp} at $\log_{10}(\epsilon_w) = 0.62$ and $\log_{10}(\epsilon_w) = 1.15$ correspond to the measured forces using the brass and copper tube, respectively. For $\log_{10}(\epsilon_w) > 4.5$ the wall tends to infinite conductivity ($F_{l,\phi} \approx 0$), and for $\log_{10}(\epsilon_w) < -4.5$, we approach electrically insulating boundary conditions ($F_w \approx 0$). (b) Limiting cases of wall conductivity. For $\epsilon_w \gg 1$, $F_{l,\phi}$ is proportional to ϵ and for $\epsilon_w \ll 1$, F_w is proportional to ϵ_w validating the predictions in sections 3.1.2.1 and 3.1.2.2.

of this behavior, the total streamwise Lorentz force is analyzed by the contributions of the liquid and wall as

$$F = F_l + F_w. \quad (3.51)$$

Analogous to (3.27), F_l can be also written as

$$F_l = F_{l,\phi} + F_{l,u \times B_0} \quad (3.52)$$

where

$$F_{l,\phi} = \int_{r \leq R_1} \sigma_l (-\nabla \phi \times \vec{B}_0) \cdot \vec{e}_x dV \quad (3.53)$$

and

$$F_{l,u \times B_0} = \int_{r \leq R_1} \sigma_l ((\vec{u} \times \vec{B}_0) \times \vec{B}_0) \cdot \vec{e}_x dV, \quad (3.54)$$

respectively. Finally, F_w can be also represented in the same way as

$$F_w = \int_{R_1 \leq r \leq R_2} \sigma_w (-\nabla \phi \times \vec{B}_0) \cdot \vec{e}_x dV. \quad (3.55)$$

The equations (3.51) to (3.55) are used for the analysis of the three different con-

Table 3.3: Comparison between the measured total Lorentz force F_{exp} and the total Lorentz force F calculated using the numerical model for $\overline{u_x} = 1\text{m/s}$.

Tube	σ_w	$ F_{exp} $	$ F $	Error
	MS/m	N	N	
PVC	0	0.154	0.146	5.5%
Brass	13.7	0.196	0.236	16.9%
Copper	47.1	0.285	0.280	1.8%

figurations considered in this chapter: conducting walls (section 3.1.4), aspect ratio variation of the cross-section of the flow (section 3.2) and LFV in electrolytes with top and bottom conducting side walls (section 3.3).

Figure 3.7(a) summarizes the results of $F_{l,\phi}$, $F_{l,u \times B_0}$, F_w and F in the case of the GaInSn loop. They are normalized by F_{ref} as a function of $\log_{10}(\epsilon_w)$ for a better visualization. Here, F_{ref} represents the value of F for insulating walls which is the current state of the art of Lorentz force velocimetry. The measured forces in the experiments F_{exp} are also normalized in the same way by F_{PVC} which is the measured force using the PVC tube. Table 3.3 summarizes the results of F_{exp} in comparison with F .

Due to the rapid decay of magnetic fields, one of the usual important contributions to uncertainty regarding measurements and simulations is the position of the magnets with respect to the flow. For instance, it was found in chapter 4 that a position uncertainty of about 0.5 mm of the small-size magnet with respect to the liquid metal could generated force uncertainties of about 13%. In this sense, the deviation between F and F_{exp} according to table 3.3 may be caused by the positioning errors between the LFF and the tube, and the errors of measurement regarding the inner diameter of the tube ($\pm 0.1\text{mm}$). In order to minimize this effect, multiple measurements were performed at different positions along the tube (inlet, middle, and outlet) and also pumping in the positive and in the negative direction (figure 3.3). However, these uncertainties are not sufficient to explain 16.9% deviation regarding the brass tube. It is assumed that the main source of this deviation is due to the formation of oxide layers or even a possible passive chemical reaction on the inner surface of the brass tube decreasing the current flow into the wall. Further investigations in this area are highly recommended in order to identify exactly the cause of this behavior, although this effect was not seen with the copper tube where there was a good agreement with a relative error of 1.8%.

According to figure 3.7(a), the wall approaches infinite conductivity when $\log_{10}(\epsilon_w) > 4.5$, whereby $F_{l,\phi} \approx 0$ as already predicted in section 3.1.2.1. For $\log_{10}(\epsilon_w) < -4.5$, the wall is effectively insulating so $F_w \approx 0$. Despite the fact that

there is indeed a significant increase in F of around 91% using copper walls in comparison with F_{ref} , we find that the expected magnitude of F by the perfectly conducting wall case is just 24% above this value. The numerical results show that F does not converge to the $F_{l,u \times B_0}$ limit which is constant and does not depend on σ_w . This situation is attributed to the eddy current distribution in the wall which is shown in figure 3.8(a). When the eddy currents are generated inside the liquid, they flow upwards into the wall and at R_2 , due to insulating boundary condition, they are forced to bend to the sides. Then, they flow downwards through the wall and close at the bottom. As a consequence, the eddy currents in the wall are opposite to the eddy currents inside the liquid generating a force F_w opposite to $F_{u \times B_0}$. Even if the electric potential approaches an equipotential state i.e. $-\nabla\phi \approx 0$ at $\epsilon_w \gg 1$, the magnitude of F_w will be still comparable to $F_{u \times B_0}$ restricting F to approach this limit. We have to keep in mind that if ϕ is indeed constant, i.e. $\nabla\phi = 0$, no current could flow through the wall and the eddy currents generated inside the liquid will not be able to close.

For a better understanding of the physics involved, the effect of the flow-braking Lorentz force can also be expressed as the loss of mechanical energy due to Joule dissipation as

$$P = P_{l,j} + P_{w,j} \quad (3.56)$$

where

$$P = - \int \vec{f}_l \cdot \vec{u} dV, \quad (3.57)$$

$$P_{l,j} = \frac{1}{\sigma_l} \int \vec{j}_l^2 dV, \quad (3.58)$$

and

$$P_{w,j} = \frac{1}{\sigma_w} \int \vec{j}_w^2 dV. \quad (3.59)$$

Here, \vec{f}_l corresponds to the induced Lorentz force density in the liquid defined as $\vec{f}_l = \vec{j}_l \times \vec{B}_0$. As F_l from (3.52), P can be also written as a term that depends on ϕ and a term that depends on $\vec{u} \times \vec{B}_0$ so

$$P = P_{l,u \times B_0} + P_{l,\phi} \quad (3.60)$$

where

$$P_{l,u \times B_0} = - \int \sigma_l ((\vec{u} \times \vec{B}_0) \times \vec{B}_0) \cdot \vec{u} dV, \quad (3.61)$$

$$P_{l,\phi} = - \int \sigma_l (-\nabla\phi \times \vec{B}_0) \cdot \vec{u} dV. \quad (3.62)$$

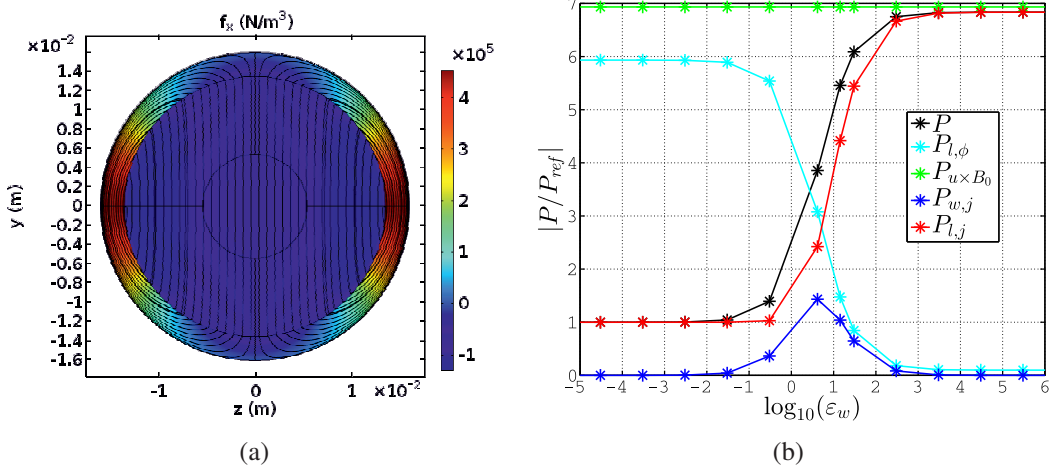


Figure 3.8: (a) Eddy current streamlines in the $z-y$ plane together with the contour plot of the stream-wise Lorentz force density f_x for $\log_{10}(\epsilon_w) > 4.5$. Here, f_x on the lateral sides of the tube is in the opposite direction that the one in the liquid. (b) Results of each of the components of (3.60) and (3.63) as a function of $\log_{10}(\epsilon_w)$ normalized by $|P_{ref}| = 0.162$ W which is the value of P for $\log_{10}(\epsilon_w) < -4.5$. For $\log_{10}(\epsilon_w) > 4.5$ the wall is infinitely conducting and all components converge to a constant value.

$P_{l,u \times B_0}$ represents the maximal power available in the system and is independent of σ_w . This power is transformed into the eddy currents in the liquid and in the wall represented by $P_{l,j}$ and $P_{w,j}$, and a contribution $P_{l,\phi}$ that depends on ϕ , so

$$P_{l,u \times B_0} = P_{l,j} + P_{w,j} + P_{l,\phi}. \quad (3.63)$$

The results of these last equations are summarized in figure 3.8(b). In this figure it is shown that $P_{l,\phi}$ does not converge to 0 as $F_{l,\phi}$. As explained before, $F_{l,\phi}$ expresses the electrical resistivity of the wall depending on the value of ϵ_w . Despite the fact that $F_{l,\phi} \approx 0$ for high ratios of ϵ_w , the electric potential ϕ is still present in the liquid generating an electric field $\vec{E} = -\nabla\phi$ that ensures $\nabla \cdot \vec{j} = 0$. According to the numerical results, $P_{l,\phi}$ inside the liquid for $\epsilon_w \gg 1$ (perfectly conducting walls) is a small fraction in comparison with $\epsilon_w \ll 1$ (insulating walls), where a stronger induced electrical potential is needed for the eddy currents to close inside the liquid.

3.2 Aspect ratio variation

In section 3.1 it was shown that the force component $F_{l,\phi}$ depends on the resistivity of the wall that confines the liquid. However, it will be discussed in this section that this force component can also be affected when the aspect ratio of the cross-section of the flow varies, leading to a significant increase of the total Lorentz force F_l . In the experiments at SOMECA (section 3.2.1), it was observed that the Lorentz force

is about 2.6 times stronger when the bar with cross-section $100 \times 50 \text{ mm}^2$ is placed vertically than horizontally (figure 3.9). For a better understanding of this effect, two numerical models of the experiments were developed: 3D model (section 3.2.2) and 2D model (section 3.2.3). Each component of the Lorentz force is going to be separately analyzed in order to see their evolution by different aspect ratios of the bar, which has a constant cross-section.

3.2.1 Experimental set-up and results

The influence of the aspect ratio variation of the cross-section of the flow on the measured Lorentz force is experimentally investigated at the SOMECA facility (Solid METal CALibration) which is depicted in figure 3.9(a). It is used for the dry calibration of the LFF. Dry calibration is understood as the use of solid bars instead of liquid metal in order to find the calibration factor K_v that relates the force signal \vec{F} of the load cell and the volumetric flow rate \dot{V} according to $\dot{V} = K_v \cdot |\vec{F}|$. This procedure was proposed by Minchenya [35] for the calibration of LFF in open-channel flows where the melt level is fluctuating resulting in a non-linear behavior between the force and the flow rate. According to [52], the Lorentz force \vec{F} for closed channel turbulent flows at high Reynolds numbers ($Re > 10^4$) is weakly affected by the specific shape of the velocity profile and it can be approximated by a solid conductor moving at a constant velocity. Additionally, the influence of symmetric and asymmetric flow profiles was experimentally investigated in [72] in the case of electrolytes. Here, it

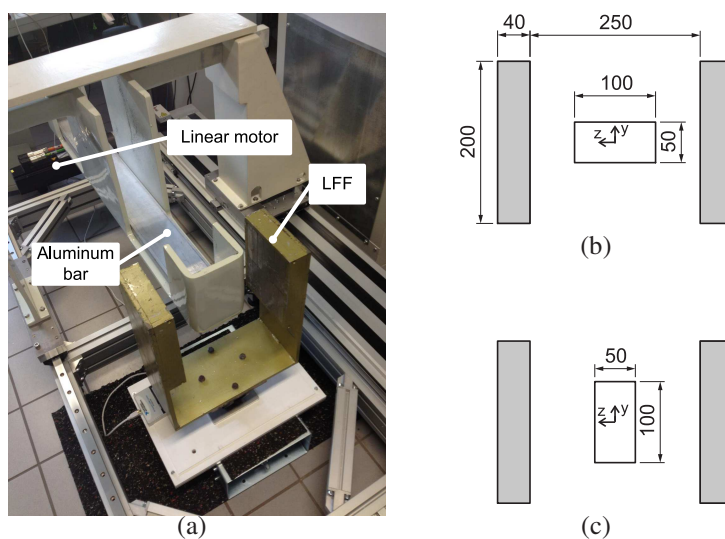


Figure 3.9: (a) SOMECA experimental facility with linear motor, aluminum bar and LFF. Cross-section of SOMECA with aluminum bar placed horizontally (b) and vertically (c) in the middle of two permanent magnets (gray). The distance between the permanent magnets is 250 mm and the cross-section of the bar is $100 \times 50 \text{ mm}^2$. The measured Lorentz force in (b) is 0.51 N and in (c) is 1.34 N.

was concluded that the measured Lorentz force is not sensitive to various flow profiles in turbulent regime.

The LFF at SOMECA has two magnet blocks with dimensions $140\text{mm} \times 200\text{mm} \times 40\text{mm}$. Each of this magnet blocks is composed of 28 single permanent magnets (NdFeB, N48H) with dimensions $20\text{mm} \times 100\text{mm} \times 20\text{mm}$. The magnetization direction is the same for all magnets and points perpendicular to the moving bar. The magnets blocks are fixed to a steel yoke that closes the outer magnet circuit and is connected to an analogue-digital converter (like the LFF from section 3.1.1). In the present study, an aluminum bar (previously used in [35]) with dimensions $1000\text{mm} \times 50\text{mm} \times 100\text{mm}$ was employed as test body. In the experiments, two different arrangements of the bar were used: 1- bar placed horizontally (figure 3.9(b)) and 2- bar placed vertically (figure 3.9(c)) in the middle of the permanent magnets. For both cases, the bar moves at a constant velocity $\bar{u}_x = 0.12\text{m/s}$. Although the magnitude of the magnetic field inside the bar is weaker in the vertical case, it generates about 2.6 times stronger Lorentz force in comparison with the horizontal case. A detailed explanation of these results is presented further in this chapter in section 3.2.2.

3.2.2 3D Model

The sketch of the 3D numerical model is depicted in figure 3.10 and the geometrical parameters are presented in table 3.4. By changing h/w , the eddy current distribution in the bar is modified due to the proximity of the top and bottom walls of the bar to the magnetic field generated by the permanent magnets. The insulating walls do not allow the currents to grow further, and therefore, they are forced to close in a smaller region restricting the magnitude of F_l . This kind of resistivity regarding insulating walls is associated with how strong the gradient of the induced electric potential ϕ has to be in order to close the eddy currents inside the bar. This resistivity, as in the conducting

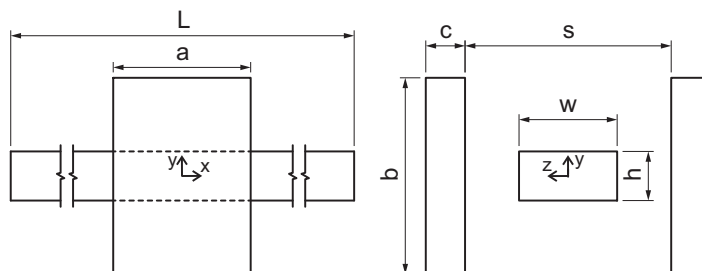


Figure 3.10: Sketch of the considered problem: a solid bar with conductivity σ_l and cross-section $w \times h$ moves at a constant velocity u_x through the middle of two permanent magnets whose magnetization direction is \vec{e}_z . Their center is placed at $x = 0$, $y = 0$, $z = \pm(s/2 + c/2)$.

3. Electric potential in Lorentz force velocimetry

Table 3.4: Geometry parameters and material properties of the aluminum bar.

Parameter	Value
Cross-section $w \times h$	$50 \times 100 \text{ mm}^2$
Length L	1000 mm
h/w	0.125 ... 32
Elec. cond. bar σ_l	$22 \cdot 10^6 \text{ S/m}$
Distance magnets s	250 mm

Table 3.5: Parameters of the permanent magnets used in the numerical model of SOMECA.

Parameter	Value
Dimensions (a \times b \times c)	$140 \times 200 \times 40 \text{ mm}^3$
Material	NdFeB
Grade	N48H
Magnetization density M_z	$1.29 \times 10^6 \text{ A/m}$

Table 3.6: Comparison between measured total Lorentz force F_{exp} and the total Lorentz force F_l calculated using the numerical model for $u_x = 0.12 \text{ m/s}$.

h	$ F_{exp} $	$ F_l $	Error
mm	N	N	
50	0.51	0.51	0%
100	1.34	1.32	1%

walls case, is associated with $F_{l,\phi}$.

The magnetization of the permanent magnets $M_z = 0.97 \cdot 10^6 \text{ A/m}$ was previously obtained by Stelian in [53]. Here, it was found that without the steel yoke, the total force decreases by about 40%. However, the increase of magnetic field due to the magnetization of the yoke is not taken into consideration in the present numerical model. Hence, in order to incorporate this effect, the magnetization is increased likewise up to the value $M_z = 1.29 \cdot 10^6 \text{ A/m}$. In this case for $u_x = 0.12 \text{ m/s}$, there is a good agreement between the experiments and the numerical model for the values of h shown in table 3.6. The parameters of the permanent magnets are presented in table 3.5. It is acknowledged that the magnetic field in experiments and simulations using this modified M_z may differ locally, but the physics behind the increase or decrease of F_l due to the variation of the aspect ratio of the cross-section of the bar are the same.

Like in the numerical model of section 3.1.3 and as the magnetic field \vec{B}_0 and velocity u_x of the bar are already given, the electrical potential ϕ can be obtained by solving (3.5). Then, \vec{j}_l , F_l , $F_{l,\phi}$ and $F_{l,u \times B_0}$ are determined through (3.1), (3.52), (3.53) and (3.54), respectively. The results of the forces are shown in figure 3.11(c). In contrast to the case discussed in section 3.1, it is found that $F_{l,u \times B_0}$ is no longer constant and decays by increasing the aspect ratio h/w . Due to the rapid decay of magnetic field along the z -axis and as the bar is becoming thinner in this direction, the average strength of the magnetic field in the bar becomes weaker in each step. For the simultaneous

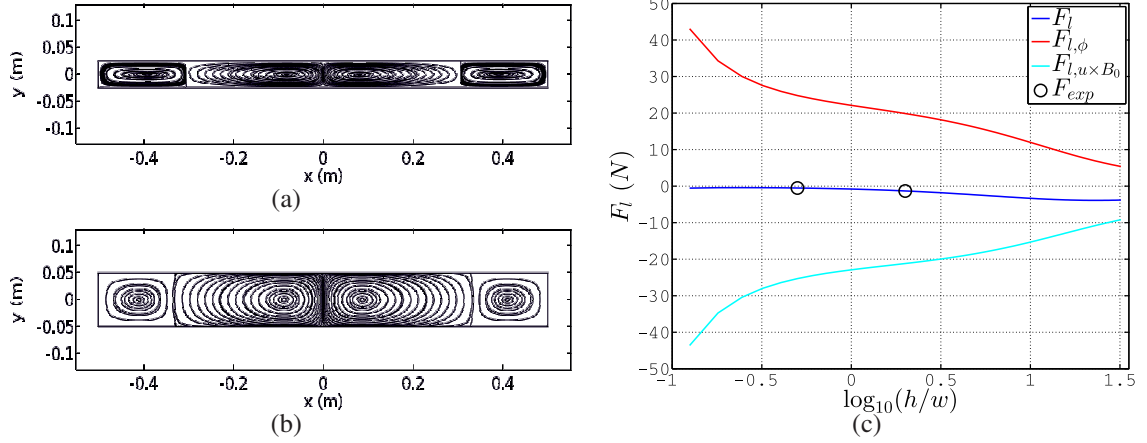


Figure 3.11: (a) Eddy current streamlines for j_x and j_y in the $x-y$ plane for $\log_{10}(h/w) = -0.3$ (a) and $\log_{10}(h/w) = 0.3$ (b). (c) F_l , $F_{l,\phi}$, $F_{l,u \times B_0}$ and F_{exp} , as a function of $\log_{10}(h/w)$. $F_{l,\phi}$ is always in the order of magnitude and in the opposite direction to $F_{l,u \times B_0}$. We can see that even though $F_{l,u \times B_0}$ decays when h/w is rising, the total Lorentz force F_l increases.

increase of F_l , the influence of the top and bottom insulating walls plays an important role restricting the growth of the induced eddy currents. At the top and bottom boundaries, an electric field $\frac{\partial \phi}{\partial y} = \vec{u} \times \vec{B}_0 \cdot \vec{e}_y$ is generated in order to satisfy the electrical insulating boundary condition. According to the numerical results based on the 2D approximation of the problem (section 3.2.3), the force generated by this electric field represents a fraction of $F_{l,\phi}$ which diminishes when the top and bottom side walls ($y = \pm h/2$) in comparison with the Hartmann walls ($z = \pm w/2$) get smaller. In other words, for bigger h/w , the eddy current loops cover a larger volume of the bar generating a stronger value of F_l . For a better visualization of this effect, the eddy currents j_x and j_y in the $x-y$ plane are plotted in figures 3.11(a) and 3.11(b) for $h = 50$ mm and $h = 100$ mm, which correspond to $\log_{10}(h/w) = -0.3$ and $\log_{10}(h/w) = 0.3$, respectively. For $h = 50$ mm, the eddy currents loops are forced to close earlier in y -direction, and therefore, its value of $F_{l,\phi}$ in comparison with $F_{u \times B_0}$ is higher than in $h = 100$ mm. As a consequence, F_l , which is the sum of $F_{l,\phi}$ and $F_{u \times B_0}$, is significantly higher when the bar is placed vertically than horizontally.

According to figure 3.11(c), as expected, $F_{l,\phi}$ is always in the opposite direction to $F_{l,u \times B_0}$. The way in which both quantities interact will represent in a positive or negative effect on the total Lorentz force F_l . For example, F_l does not increase when h/w grows for values lower than $\log_{10}(h/w) \approx -0.61$ (see figure 3.12(b)). This effect can be attributed to the fact that the lateral sides of the bar are very close to the magnet where the magnetic field and its gradient are higher. After this minimum point in h/w , the decay of $F_{l,\phi}$ is faster than $F_{l,u \times B_0}$. By increasing h/w further, the maximum value of F_l is reached at $\log_{10}(h/w) \approx 1.36$ in which the magnetic field with higher density does not reach the upper and lower walls any more.

3.2.3 2D Model

For bigger values of h/w , the eddy currents become purely two dimensional and the bar can be modeled by a 2D thin layer with thickness w (figure 3.12(a)). The length of the layer is $L_{2D} = 10L = 10\text{ m}$ and its height will be gradually increased until $h = 5000\text{ mm}$. Here, \vec{B}_0 is taken from the symmetry plane $x-y$ and it is assumed constant across the thickness w . The current density is obtained from (2.10) and the forces per unit width w of the layer take in this case the form

$$F_{2D} = F_{2D,\phi} + F_{2D,u \times B_0}, \quad (3.64)$$

$$F_{2D,\phi} = \int \sigma_l (-\nabla \phi \times \vec{B}_0) \cdot \vec{e}_x dA, \quad (3.65)$$

and

$$F_{2D,u \times B_0} = \int \sigma_l ((\vec{u} \times \vec{B}_0) \times \vec{B}_0) \cdot \vec{e}_x dA. \quad (3.66)$$

In this case, the boundaries of the domain are electrically insulating where $j_n = 0$. According to figure 3.12(b), there is good agreement between the 3D and the 2D numerical models for values of $\log_{10}(h/w) > 1$, where $F_l \approx F_{2D} \cdot w$, $F_{l,\phi} \approx F_{2D,\phi} \cdot w$ and $F_{l,u \times B_0} \approx F_{2D,u \times B_0} \cdot w$. The advantage of the simplified 2D model is that for $h = 5000\text{ mm}$, the layer can be considered semi-infinite, which means that the magnetic field \vec{B}_0 does not reach anymore the boundaries of the domain and (3.64), (3.65), and (3.66) converge to a limit different from zero. When $h/w \rightarrow \infty$, the induced elec-

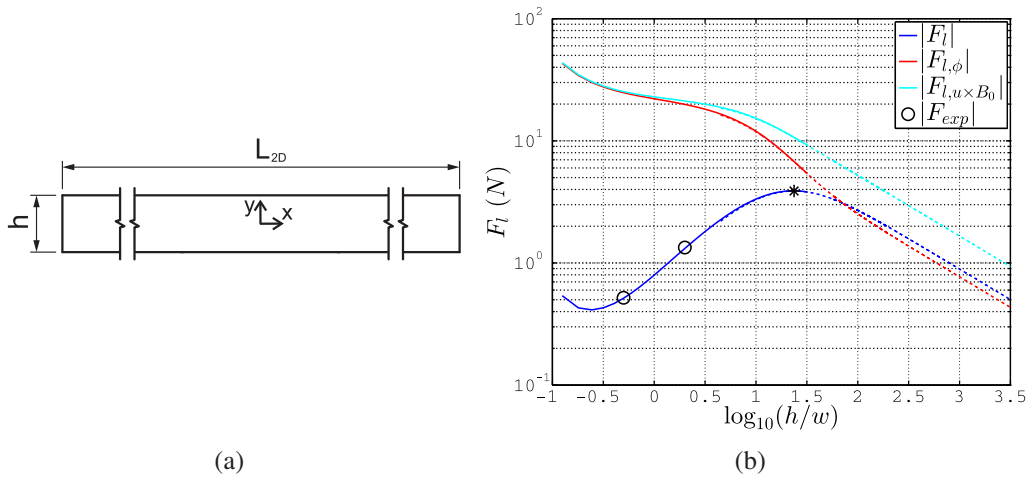


Figure 3.12: (a) 2D model of the bar for $\log_{10}(h/w) > 1$. (b) F_l , $F_{l,\phi}$, $F_{l,u \times B_0}$ and F_{exp} , as a function of $\log_{10}(h/w)$ for the 3D (solid lines) and 2D numerical model (dashed lines). The 2D solution is plotted for $\log_{10}(h/w) > 0.65$. The dark asterisk corresponds to the value of h/w where $F_l \approx F_{2D} \cdot w$ is maximum.

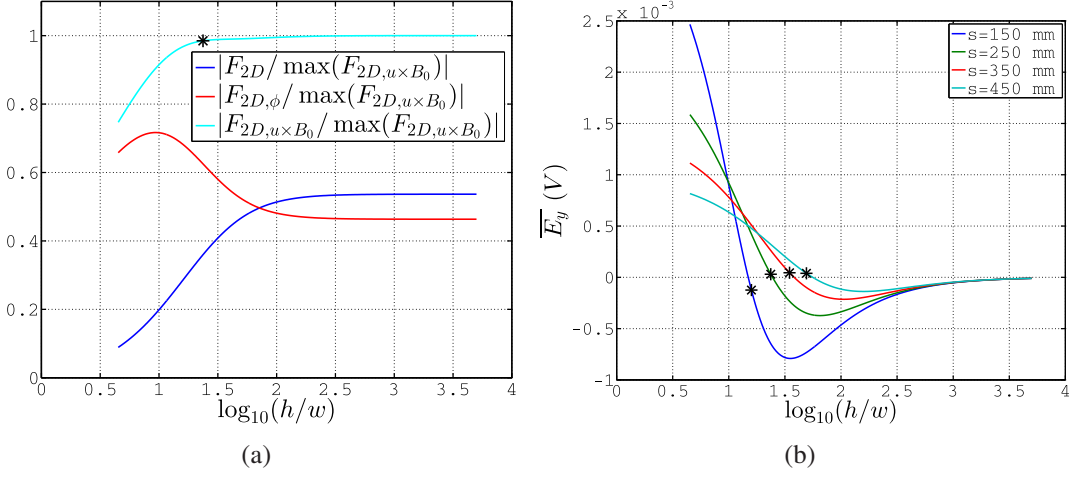


Figure 3.13: (a) F_{2D} , $F_{2D,\phi}$ and $F_{2D,u \times B_0}$ normalized by $\max(|F_{2D,u \times B_0}|) = |F_{2D,u \times B_0}|_{h/w \rightarrow \infty} = 742.4 \text{ N/m}$ as a function of $\log_{10}(h/w)$. (b) \overline{E}_y as a function of $\log_{10}(h/w)$ for different s . The black points correspond to the location of the maximum force $F_{2D} \cdot w$ and $|F_{2D,u \times B_0}/\max(F_{2D,u \times B_0})| \approx 98\%$.

tric field on the boundary will vanish and the value of $F_{2D,\phi}$ will represent the effect of the induced electric potential ϕ without the influence of insulating walls (see figure 3.13(a)). In order to quantify the effect of the induced electric field given by $\frac{\partial \phi}{\partial y}$ on the top and bottom walls, let's define

$$\overline{E}_y = \int_{-L/2}^{L/2} \frac{\partial \phi}{\partial y} dl = \int_{-L/2}^{L/2} (\vec{u} \times \vec{B}_0) \cdot \vec{e}_y dl. \quad (3.67)$$

Here, \overline{E}_y is the line integral of $\frac{\partial \phi}{\partial y}$ on the top or bottom boundary of the layer ($y = \pm h/2$). The results are presented in figure 3.13(b). In this figure it is shown that \overline{E}_y is maximum for small values of h/w , where the top and bottom walls are near to the applied magnetic field of higher magnitude, and therefore, a stronger electric field is induced in order to satisfy insulating boundary conditions. For $h/w \gg 1$, $\overline{E}_y \rightarrow 0$ as expected. Additionally, it was observed that the value of the aspect ratio h/w , where $\overline{E}_y = 0$ for distance between magnets $s = 150 \dots 450 \text{ mm}$, provides a relative good assessment of the expected value of the maximum force $F_{2D} \cdot w$ and h .

In conclusion, the more pronounced decay of $F_{l,\phi}$ compensates the one of $F_{u \times B_0}$ when the aspect ratio of the bar is changed resulting in a considerable increase of the total Lorentz force F_l . However, according to the results of the 2D model, $F_{2D,\phi}$ converges to a value different from zero for $h/w \gg 1$, contrary to the infinite wall conductivity case where $F_{l,\phi} \approx 0$. The numerical results show that $F_{2D,\phi}$, or in general $F_{l,\phi}$, has a component that depends on the proximity of the top and bottom side walls to the applied magnetic field of higher density and it decreases when h/w increases. The optimal h/w , where F_{2D} is maximum, is obtained where $F_{2D,u \times B_0}/F_{2D,u \times B_0}|_{h/w \rightarrow \infty} \approx 98\%$ or $\overline{E}_y \approx 0$ according to figures 3.13(a) and 3.13(b). The location of $F_{2D} \cdot w|_{\overline{E}_y=0}$

offers a good approximation of the maximum values of $F_{2D} \cdot w$ with a relative error less than 1% and for h less than 7%.

3.3 Lorentz force velocimetry in electrolytes

According to section 3.1 and 3.2 it was found that in particular, when ϵ_w or h/w are increased, $F_{l,\phi}$ diminishes providing a significant increase of the magnitude of the measurable Lorentz force F . Now, the numerical model in this section applies these two concepts in order to increase the measurable Lorentz force in weakly conducting fluids, i.e. electrolytes. Here, the results obtained in the experimental set-up described in [67] are taken as reference, where the flow rate of salt water was measured using a LFF. In this set-up, salt water flows through a rectangular duct made of glass at an average velocity \overline{u}_x . Two permanent magnets are placed on each side in the middle of the duct and are connected to a pendulum. Their magnetization M_z points orthogonal to the duct as the previous set-ups mentioned in the present chapter. The displacement of the pendulum due to the induced Lorentz force acting on the magnets is measured by a laser interferometer. On the other hand, the top and bottom side walls in the present numerical model are electrically conducting, whereas the Hartmann walls are insulating. As shown in section 3.2, the top and bottom side walls have the predominant influence on the growth of the eddy currents, and therefore, contribute strongly to the magnitude of $F_{l,\phi}$. The reason of choosing insulating Hartmann walls relies on the fact that if they were conducting, the currents flowing through them will actually generate a force opposite to that one of the flow. As shown in figure 3.8(a), these currents in the wall will cause a reduction of F rather than an increase. The sketch of the considered

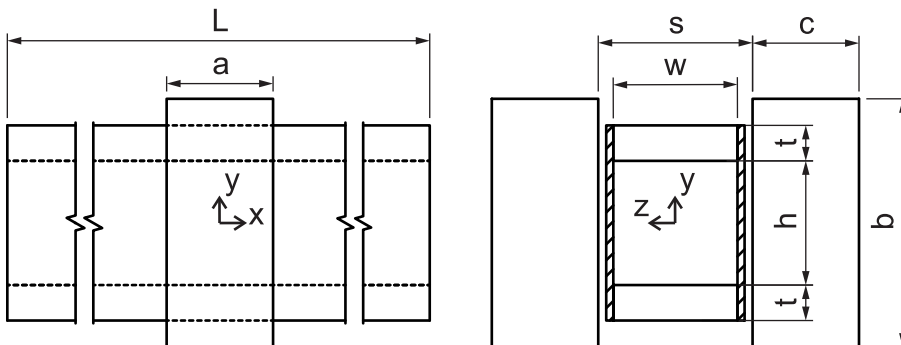


Figure 3.14: Sketch of the considered problem: electrolyte with conductivity σ_l flows through a rectangular duct with inside cross-section of $w \times h$. The upper and lower side walls are conducting with a value of conductivity σ_w and a thickness t . Two permanent magnets are placed at each side of the duct leaving an air gap between the surface of the magnet and the surface of the lateral walls, i.e. Hartmann walls, which are insulating. Their magnetization direction is \vec{e}_z and their center is placed at $x = 0, y = 0, z = \pm(s/2 + c/2)$.

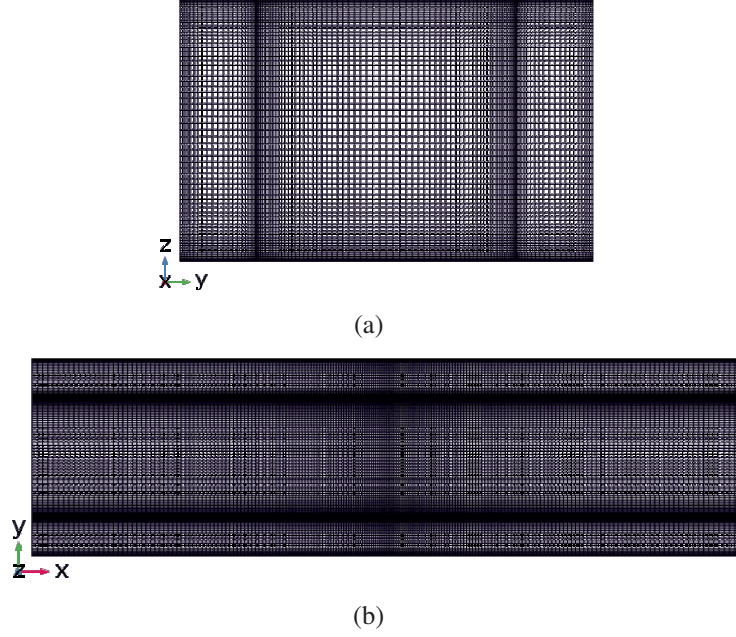


Figure 3.15: Cross-section (a) and front view (b) of the structure of the mesh containing in total $1.54 \cdot 10^6$ non-uniform second order hexahedral elements.

problem is shown in figure 3.14 and its mesh is depicted in figure 3.15.

This type of configuration has been already investigated in [22, 4, 36] for fully-developed magnetohydrodynamic laminar and turbulent profiles at high Hartmann numbers Ha . Here, the applied magnetic field is constant and the conducting walls are assumed thin. In the present problem we have low Ha but the conducting walls cannot be considered thin as F strongly depends on their thickness t . The analysis will be focused on fully-developed laminar and turbulent velocity profiles in a square duct, whereby the velocity distributions are prescribed. The laminar profile can be numerically determined according to [38] as

$$u_x(y, z) = \frac{\chi}{2\mu} b_0^2 \left[1 - \frac{z^2}{b_0^2} + 4 \sum_{n=1}^{\infty} \frac{(-1)^n \cosh(\alpha_n \frac{y}{b_0})}{\alpha_n^3 \cosh(\alpha_n \frac{a_0}{b_0})} \cos\left(\alpha_n \frac{z}{b_0}\right) \right], \quad (3.68)$$

$$\chi = \bar{u}_x (12\mu a_0 b_0) \left[4a_0 b_0^3 \left(1 - 6 \frac{b_0}{a_0} \sum_{n=1}^{\infty} \frac{1}{\alpha_n^5} \tanh\left(\alpha_n \frac{a_0}{b_0}\right) \right) \right]^{-1}, \quad (3.69)$$

where $a_0 = h/2$, $b_0 = w/2$, $\alpha_n = (n - 1/2)\pi$, and μ denotes the kinetic viscosity. The laminar velocity field in the model $u_x(y, z)$ is calculated until $n = 10$.

The fully-developed turbulent velocity profile in a square duct was obtained previously by Krasnov in [28] for $Re = 1 \cdot 10^5$. In the present case, the characteristic length $l_c = h/2 = 35/2$ mm of the square duct is chosen in such a way that the size of its cross-section corresponds to the same one used in [67], and \bar{u}_x is also in the same range for

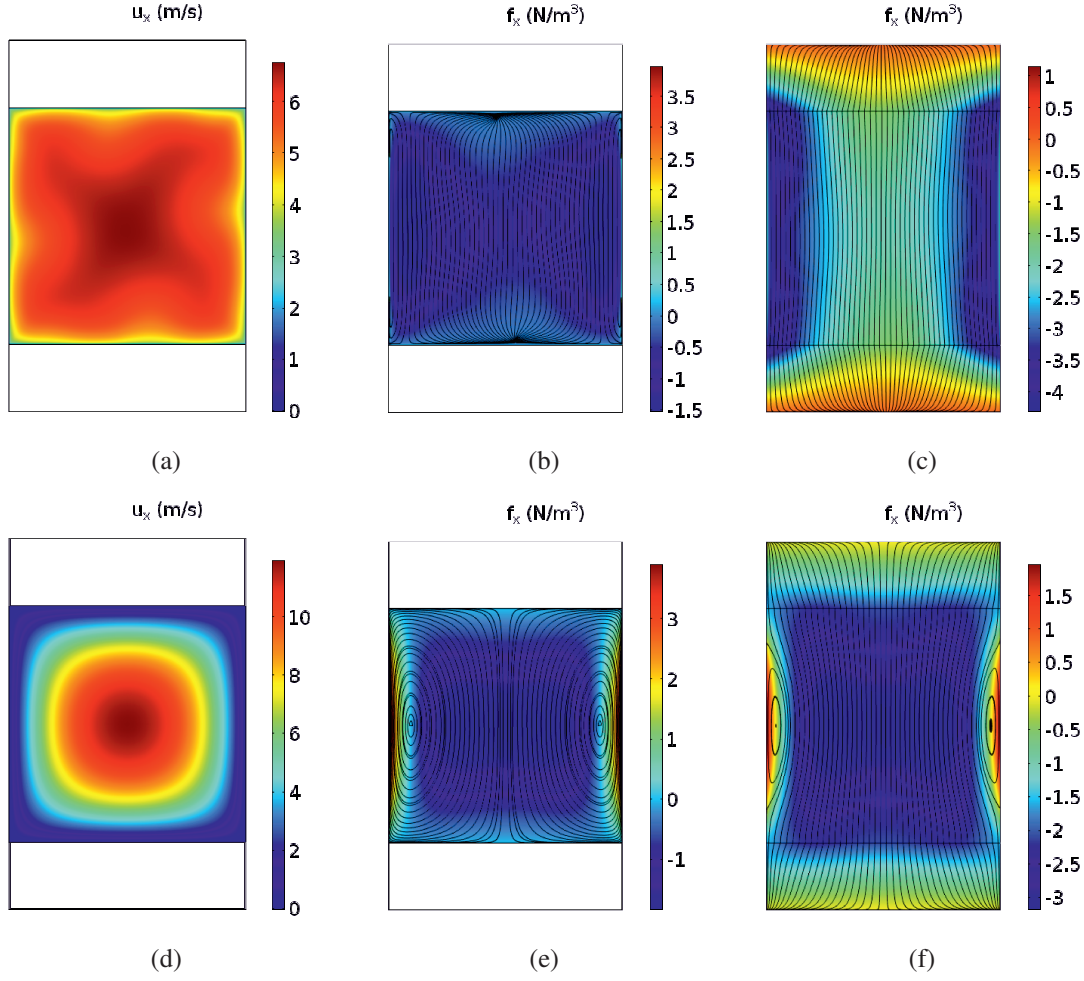


Figure 3.16: Streamwise velocity distribution u_x for turbulent (a) and laminar (d) solutions for the same $Re = 1 \cdot 10^5$ and average velocity $\bar{u}_x = 5.7 \text{ m/s}$ according to [28] and [38], respectively. Eddy current streamlines in the $z-y$ plane together with the contour plot of the streamwise Lorentz force density f_x for perfectly insulating (b) and conducting (c) walls for a fully-developed 3-dimensional turbulent velocity distribution. (e) and (f) are obtained by taking a laminar velocity profile for the same cases.

comparison. The numerical solution for a steady turbulent flow at high Reynolds numbers requires large storage and long computation time restricting optimization studies for the LFF. Therefore, the present study intends to compare the solutions of F for laminar and fully-developed 3D turbulent velocity profiles that share the same \bar{u}_x . If the error of assuming a laminar profile is relatively low, it will then be possible to perform conservative optimization procedures regarding the LFF for a given application. Figures 3.16(a) and 3.16(d) show the turbulent and laminar profiles for $\bar{u}_x = 5.7 \text{ m/s}$ and $Re = 1 \cdot 10^5$, which are the source of \vec{u} in the numerical model. As in the previous sections, table 3.7 and table 3.8 summarize the geometry and material properties of the liquid and the wall as well as the parameters of the permanent magnets, respectively.

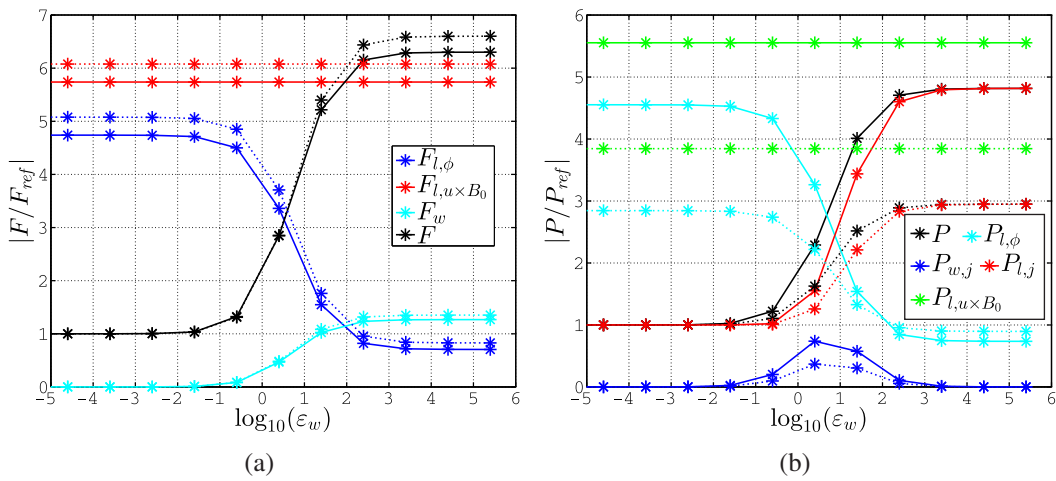
The advantage of using salt water as working fluid is that we can easily reach effectively infinite wall conductivity by using common materials for the wall such as

Table 3.7: Geometry parameters and material properties of salt water and electrically conducting wall.

Parameter	Value
Kinematic viscosity ν	$1 \cdot 10^{-6} \text{ m}^2/\text{s}$
Elec. cond. liquid σ_l	4 S/m
Elec. cond. wall σ_w	$10^{-8} \dots 10^6 \text{ S/m}$
Size liquid $w \times h \times L$	$35 \times 35 \times 200 \text{ mm}^3$
Wall thickness t	10 mm
Distance magnets s	41 mm

Table 3.8: Parameters of the permanent magnets according to [64].

Parameter	Value
Size ($a \times b \times c$)	$30 \times 70 \times 30 \text{ mm}^3$
Material	NdFeB
Grade	N48
Magnetization density M_z	$1.050 \cdot 10^6 \text{ A/m}$


 Figure 3.17: (a) $F_{l,\phi}$, $F_{l,u \times B_0}$, F_w and F as a function of $\log_{10}(\epsilon_w)$ for turbulent (solid line) and laminar (dashed line) velocities profiles. (b) Results of each of the components of (3.60) and (3.63) as a function of $\log_{10}(\epsilon_w)$.

copper or aluminum ($\log_{10}(\epsilon_w) \approx 7$). However, as now the Hartmann walls are insulating, the eddy currents j_y that are opposite to the ones from the core will now flow through the Hartmann layers in a rather small region (see figures 3.16(f) and 3.16(c)). This implies that now $F_{l,\phi}$ does not tend to zero but to a finite value resulting in a decrease of F_l for $\log_{10}(\epsilon_w) > 4.5$ (figure 3.17(a)). The power component $P_{l,\phi}$ is also higher meaning that more power from $P_{l,u \times B_0}$ is needed in order to satisfy charge conservation in the liquid as seen in both laminar and turbulent solutions (figure 3.17(b)). However, as now the top and bottom side walls are electrically conducting, the eddy currents are stretched further in y -direction into the walls generating a F_w in the same direction of F . Hence, F_w compensates the negative effect of $F_{l,\phi}$ generating at the end a total Lorentz force F even higher than $F_{l,u \times B_0}$ as shown in figure 3.17(a). Analogous to section 3.1.4, the force components are normalized by the force using insulating walls $|F_{ref}| = 15.4 \mu\text{N}$ and $|F_{ref}| = 17.8 \mu\text{N}$ for the laminar and turbulent solutions, respectively. This is also the case of the power analysis where $|P_{ref}| = 0.183 \text{ mW}$ and

$|P_{ref}| = 0.105$ mW for the laminar and turbulent profiles, respectively.

Regarding the eddy current paths for both velocity profiles, one can observe noticeable differences between them. For example, in the turbulent case, the eddy currents in the cross-section of the liquid are almost parallel to the walls. This behavior is due to the very steep boundary layer for high Re behaving like a solid moving at $\overline{u_x}$. However, the increase of F in contrast to F_{ref} is comparable for the turbulent and laminar velocity profiles for the limiting case $\log_{10}(\epsilon_w) > 4.5$ with $F/F_{ref} = 6.3$ and $F/F_{ref} = 6.6$, respectively. Here, the difference between F_{ref} for both fixed velocity distributions is about 10%. It can therefore be concluded that the laminar solution can quickly give a conservative value of the expected magnitude of the force F for insulating and infinite conducting walls in a square duct. However, the error regarding F_{ref} does not only depend in general on the velocity distribution but also on the aspect ratio of the cross-section of the flow and the distance between the permanent magnets.

Let's now consider the exact parameters from the experiments in [67] and predict the increase of F using conducting top and bottom side walls. By applying the laminar approximation of the velocity profile for the aspect ratio $h/w = 46 \text{ mm}/26 \text{ mm} = 1.77$, $\overline{u_x} = 3 \text{ m/s}$ and $s = 32 \text{ mm}$, $|F_{ref}| = 17.7 \mu\text{N}$ whereas $|F_{exp}| \approx 17 \mu\text{N}$ having a deviation of about 4%. The expected increase of F using top and bottom copper walls ($t = 10 \text{ mm}$) is $F/F_{ref} = 3.3$, i.e. $F = 3.3(|F_{ref}|) = 3.3(17.7 \mu\text{N}) = 58.4 \mu\text{N}$. As shown in section 3.1.4 regarding the brass tube, an investigation of erosion, oxide layer formation and wettability at the boundary liquid-solid should be carried out beforehand. This step is needed in order to ensure that the generated eddy currents will flow through the wall without any additional resistance and obtain the expected increase of the measurable Lorentz force.

3.4 Conclusions

The present study has shown that the force component $F_{l,\phi}$ generated by the induced electric potential ϕ is sensitive to the ratio between electric conductivity of the wall and the liquid ϵ_w . Perfectly conducting and perfectly insulating walls appear when $\log_{10}(\epsilon_w) > 4.5$ and $\log_{10}(\epsilon_w) < -4.5$, respectively. In the first case, $F_{l,\phi}$ is zero and in the second one it reaches its maximum value. According to the results dealing with the variation of the aspect ratio of the cross-section of the flow, this force depends on the proximity of the top and bottom side walls to the applied magnetic field of higher magnitude. In general, the force component generated by the induced electrical potential is always opposite to the one given by $\vec{u} \times \vec{B}_0$. Hence, when $F_{l,\phi}$ is diminished by either increasing the electrical conductivity of the walls or by changing the aspect

ratio of the cross-section of the flow, there is a significant increase of the measurable total Lorentz force, and therefore, the sensitivity of the measurements is improved. In the case of Lorentz force velocimetry in electrolytes, infinite wall conductivity can be effectively reached using common materials like copper.

For top and bottom electrically conducting walls in infinite wall conductivity regime, a 6 times higher force can be expected in comparison with insulating walls for a rectangular duct. By comparing a laminar and a turbulent velocity profile for the same Re , the results in the last section have shown that a conservative estimate of the expected increase of the measurable Lorentz force can be obtained by using the laminar approximation. Hence, it allows in the future fast and broader parameter optimization of the Lorentz force flowmeter. An optimization procedure dealing with the magnet size, aspect ratio of the flow and wall thickness of the top and bottom walls is advantageous for achieving higher values of the total Lorentz force for a given application.

3. Electric potential in Lorentz force velocimetry

Chapter 4

1D local Lorentz force velocimetry

This chapter focuses on the first experimental stages of local Lorentz force velocimetry (local LFV) using cross-shaped magnets in comparison with a reference 10mm cubic magnet. The idea is to investigate the effect of non-axisymmetric magnetic field distributions on the streamwise Lorentz force for a fully-developed-turbulent channel flow with and without cylindrical obstacles inside the duct. The used magnet systems are described in section 4.1 followed by a comparison of their corresponding magnetic field distributions. Then, section 4.2 presents the experimental set-up and section 4.3 provides the main results. Finally, section 4.4 gives a summary of the main conclusions.

4.1 Magnet systems

As already mentioned in chapter 1, the volume subset of the liquid that interacts with the magnetic field has to be considerably smaller than the cross-section of the flow in order to have a localized velocity assessment of the liquid metal. However, if we decrease the size of the magnets under a limit, the measured force decreases likewise making its measurement a big challenge for the existing force measurements devices. For instance, it was found by Heinicke [16] that the force using a 5 mm cubic magnet is 150 times weaker in comparison with a 15 mm cubic magnet (about 5 mN), whose volume is 27 times bigger. This behavior is due to the different magnetic field distributions in the liquid metal. In simple words: the bigger the magnet, the greater the volume of the fluid spanned by the magnetic field is, and therefore, the magnitude of the force is stronger. This topic will be deeply discussed in section 5.8, where the spatial resolution of different magnet systems is numerically analyzed for the experiments at the mini-LIMMCAST facility. However, not just the volume of the magnet has an impact on the force or torque, but its geometry has also to be considered. An

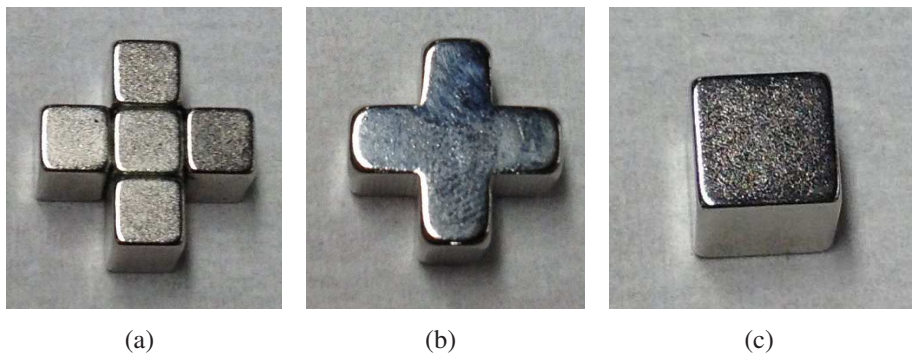


Figure 4.1: Permanent magnet systems: (a) cross-shaped magnet arrangement ($CSMA_{10.66}$), (b) cross-shape magnet ($CSM_{10.66}$), and (c) 10mm cubic magnet (CUB_{10}). The subscript of the magnet systems corresponds to the characteristic length l_{mag} of the magnet. The definition of l_{mag} is explained in section 5.2. All magnet systems share the same volume and material for comparison. Their magnetization points orthogonal to the surface of the paper.

optimized geometry of the magnet system can generate, for example, axisymmetric or non-axisymmetric magnetic field distributions in the liquid depending on the application. A non-axisymmetric magnetic field distribution is needed in order to have access to the torque component that points in the direction of magnetization of the magnet (see section 5.3.3). As shown in chapter 5, this torque gives us an insight into the local gradient or curl of the velocity field in this direction.

In the present study, a non-axisymmetric magnetic field distribution is generated using cross-shaped magnets. The goal is to potentially maintain or increase the spatial resolution of the force, whereby the torque in the direction of magnetization of the magnet can now be accessible. Hence, when the force and torque are simultaneously measured, we can have an insight into both local velocity and local vorticity of the liquid metal in the region adjacent to the wall. The results of multicomponent measurements and simulations will be later presented in chapter 5. As multicomponent measurements is meant the simultaneous measurement of all three force and all three torque components acting on the magnet system. In view of the present and latter experiments, two cross-shaped magnets and a reference cubic permanent magnet were considered at the beginning of the study (figure 4.1). The model experiments were performed at the ILMET facility (Ilmenau Liquid METal Channel), which is later described in section 4.2. The reason of investigating two different cross-shaped magnets is that when the CSMA increases in size, i.e. bigger CSMA that the one shown in figure 4.1(a), the bonding through an adhesive joint was difficult to achieved. In order to avoid these problems, the alternative of having a single magnet with the same cross-shaped form (figure 4.1(b)) is also considered for future multicomponent measurements. All magnet systems share the same material and total volume for comparison and their properties are summarized in table 4.1.

Table 4.1: Parameters of magnet systems.

Property	Range
Magnet systems	CSM _{10.66} , CSMA _{10.66} , CUB ₁₀
Dimensions (CUB ₁₀)	10 mm × 10 mm × 10 mm = 1000 mm ³
Dimensions (CSM _{10.66} , CSMA _{10.66})	5(5 mm × 5 mm × 8 mm) = 1000 mm ³
Material	NdFeB
Grade	N52
Remanent magnetization B_r	1.43 T
Magnetization density M_0	1.138×10^6 A/m

4.1.1 Magnetic field distribution

For a rectangular magnet with uniform magnetization there is an analytic solution for its magnetic field components as explained previously in section 3.1.3. This model can be further used to obtain analytically the magnetic field of cross-shaped magnets by the superposition principle of magnetic fields, or in other words, by adding simultaneously the magnetic field of five $5 \times 5 \times 8$ mm³ rectangular magnets that share the same magnetization direction pointing orthogonal to the surface of the duct. Figure 4.2 compares the magnetic field component B_z of the considered cross-shaped magnets (figure 4.2(a) and 4.2(b)) in comparison with the analytic solution (figure 4.2(c)).

According to figure 4.2, the analytic solution can predict accurately the magnetic field produced by a cross-shaped permanent magnet system. Additionally, the measurements of the magnetic field component B_z show that the CSM_{10.66} exhibits a stronger and more symmetric magnetic field distribution than the CSMA_{10.66}. This situation can be explained due to intrinsic relative positioning uncertainty of the single

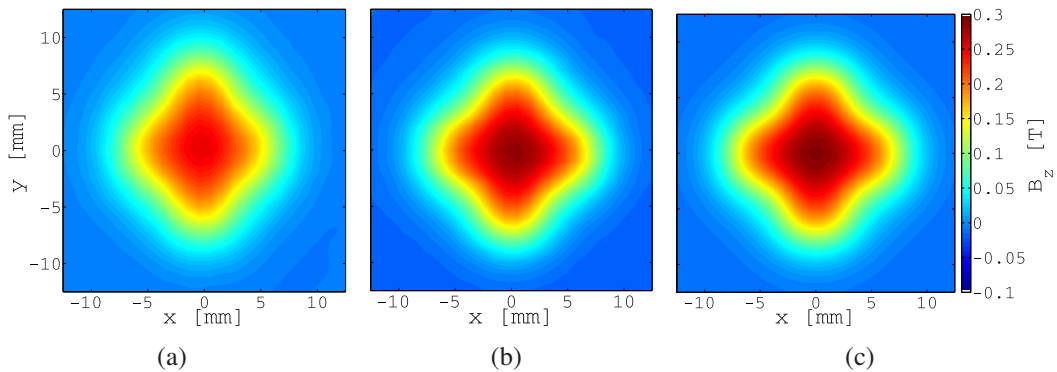


Figure 4.2: Contour plots of the measured B_z component of the magnetic field of the CSMA_{10.66} (a) and CSM_{10.66} (b) in comparison with the analytic solution for a CSM_{10.66} (c) at a distance of 3 mm away from the surface of the magnet. The magnetic field was measured using a 3D Hall probe with a 1 mm resolution.

rectangular magnets during to the process of bonding into a cross-shaped form. Hence, a single magnet in a cross-shaped form (CSM) was selected for the multicomponent measurements at the continuous caster model (section 5.7).

4.2 Experimental set-up

The ILMET facility (Ilmenau Liquid METal Channel) is a liquid metal loop that consists of stainless steel pipes and a plexiglass test section filled with the low-melting alloy GaInSn in eutectic composition. The material properties and dimensionless parameters are summarized in table 4.2. A sketch of the set-up is depicted in figure 4.3. An electromagnetic pump drives the working fluid and the flow rate is measured by a commercial inductive flowmeter (Krohne Altoflux IFS 6000). Just before the liquid metal enters the test section, it flows across a honeycomb ($D_h = 3$ mm, length = 160 mm) that works as a hydraulic resistance generating a typical turbulent flow profile. The test section is a plexiglass rectangular duct ($50\text{ mm} \times 50\text{ mm}$, wall thickness = 5 mm) which is connected to the steel pipes through flexible bellows. Their task is to isolate the duct from vibration or noise coming from the pump during experiments.

The force measurement system is composed of an interference optical force sensor (IOFS) and a small-size magnet system. In this thesis, these two systems (IOFS + magnet system) altogether are referred as the 1D-L2F2 (1D local Lorentz force flowmeter). The IOFS has a quartz glass as deformation body and the deflection is measured by a high-resolution laser interferometer [14, 13]. The deformation is resolved with an

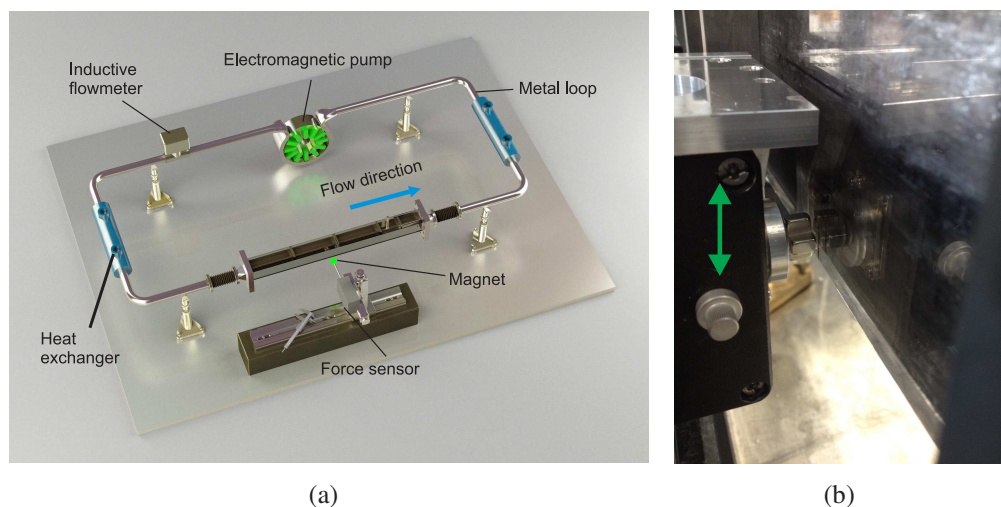


Figure 4.3: (a) Experimental facility ILMET. (b) 1D-L2F2 and plexiglass duct at the starting point of the measurements. The positioning system (not shown) moves vertically the magnet (green arrow) in predefined steps until reaching the top wall.

Table 4.2: Material properties of GaInSn and dimensionless parameters.

Property	Range	Description
σ_l	$3.46 \cdot 10^6 \text{ S/m}$	Electrical conductivity
ρ	$6.36 \cdot 10^3 \text{ kg/m}^3$	Density
ν	$3.4 \cdot 10^{-7} \text{ m}^2/\text{s}$	Kinematic viscosity
l_c	25 mm	Characteristic length (half height of the duct)
u	9.5 cm/s	Characteristic velocity (mean velocity)
B	$\approx 0.065 \dots 0.193 \text{ T}$	B_z at $z = 5 \dots 11 \text{ mm}$
$Re = \frac{ul_c}{\nu}$	≈ 7000	Reynolds number
$N = \frac{\sigma_l B^2 l_c}{\rho u}$	0.6 ... 5.3	Interaction parameter
$Ha = \sqrt{NRe}$	65 ... 193	Hartmann number

internal resolution of 0.1 nm. Then, the deformation is converted into forces according to the calibration of the device that also takes into account the influence of the temperature on the refracting index of the air and on Young's modulus [42]. At experimental conditions, the IOFS reaches a resolution of $0.3 \mu\text{N}$ in the case of one 10 mm cubic magnet [17]. The sampling frequency of the measurements is about 6.24 Hz after using the digital filter 5 (low pass filter) from the interferometer. The filter damps the frequencies above the natural frequency of the force sensor. The 1D-L2F2 is mounted on a positioning system fixed to a granite stone decoupled from the loop to avoid unwanted vibration during measurements.

4.3 Results

It was demonstrated by Heinicke [17] that, by applying local Lorentz force velocimetry, it is possible to identify a cylindrical obstacle in the flow and to resolve the wake behind it. These experiments were performed at ILMET and it was observed a spatial resolution of at least 3 cm with a 10 mm cubic magnet. The goal of the first series of experiments in this section is to replicate these results obtained by Heinicke at the same range of $Re = 7000$ with and without obstacles in the flow for comparison. The resulting force profiles using the proposed magnet systems will show if there is indeed a noticeable advantage regarding the resolution and strength of the Lorentz force by using the proposed cross-shaped magnets. A sketch of the problem set-up is depicted in figure 4.4. Here, κ represents the distance between the outer surface of the magnet and the liquid metal. κ will be used afterwards for characterizing the decay of the Lorentz force along the z -direction.

4. 1D local Lorentz force velocimetry

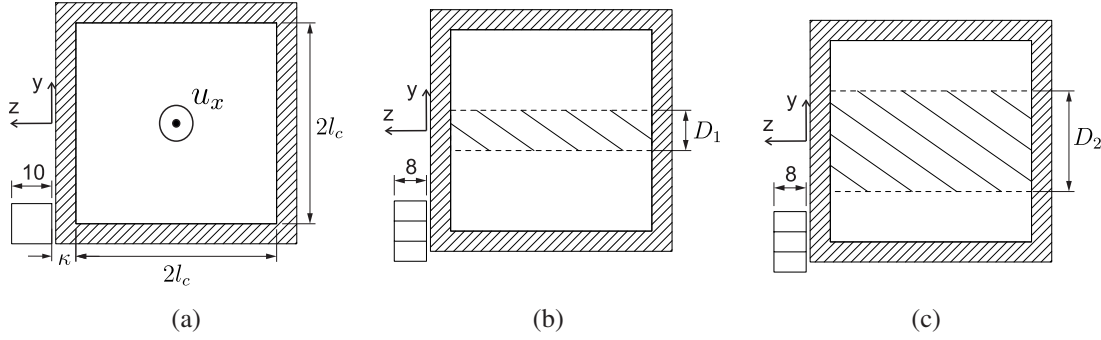


Figure 4.4: GaInSn turbulent flow without (a) and with cylindrical obstacles (b,c) inside the duct. The obstacles are two non-conducting cylindrical bars with dimensions $D_1 = 10$ mm (b) and $D_2 \approx 22$ mm (c). The 3 magnet systems taken into consideration are shown at the beginning of the experiments ($y = -l_c = -25$ mm): CUB₁₀ (a), CSM_{10.66} (b) and CSMA_{10.66} (c). The center of the obstacles as well as the center of the magnets systems are located on the $z - y$ plane.

The center of the permanent magnet is placed at the beginning of each experiment at the bottom of the duct $y = -25$ mm ($y^* = -1$). Its outer surface is facing and almost touching the wall at $z = 0$ mm (figure 4.4(a)). An air gap of about 0.4 mm between the surface of the magnet and the surface of the duct is maintained constant in order to avoid damaging the force sensor while traversing. Then, the magnet is moved upwards to $y = 25$ mm ($y^* = 1$) in 2.5 mm steps. In each step, the average value of the force is taken in 50 seconds obtaining information on the local velocity of the liquid metal inside the duct. Finally, the distance between the outer surface of the magnet and the test section is increased from $z = 0$ mm ($\kappa = 5$ mm) to $z = 6$ mm ($\kappa = 11$ mm) with a 1 mm step size. The results are presented in figure 4.5.

According to figure 4.5, the measured Lorentz force using the proposed magnet systems is stronger than the one obtained by Heinicke due to their higher magnetization. However, no noticeable difference was observed between the measured Lorentz forces using the cross-shaped magnets in comparison with the reference cubic magnet. There is still also some discrepancy in the value of the force at the bottom and top of the duct which is expected to be the equal. The higher force at the top of the duct could have been caused by the slight misalignment of the set-up; the magnet is closer to the liquid metal at the top than at the bottom of the duct ($\Delta z \approx 0.2$ mm). Appendix C (C Uncertainty analysis) will discuss the uncertainty of the measurements and a detailed analysis of its major contributions. The estimated uncertainty is around 13% of the measured forces.

Figure 4.6 depicts the decay of F with the distance κ . The results in this figure are given for $y = 0$ mm in order to avoid a possible influence of the top and bottom insulating walls on the solution. The force generated by the cross-shaped magnets presents similar decay, where $F \sim (\kappa + l_{mag}/2)^{-2.87}$ and $F \sim (\kappa + l_{mag}/2)^{-2.91}$ for

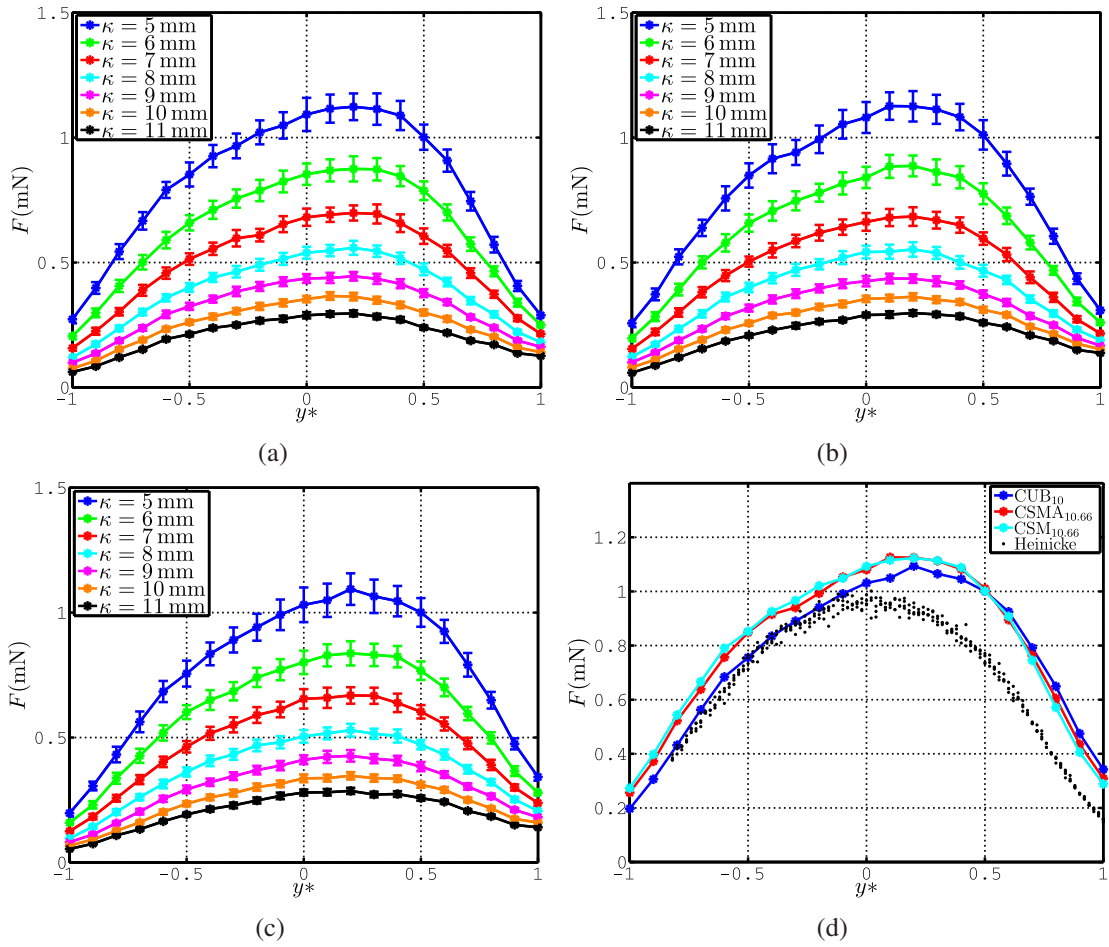


Figure 4.5: Lorentz force profiles in y - and in z - directions using the CSM_{10.66} (a), CSMA_{10.66} (b) and CUB₁₀ (c). The center of the magnets moves from the bottom ($y^* = -1$) to the top ($y^* = 1$) of the duct. A comparison between all magnets at $\kappa = 5$ mm is shown in (d).

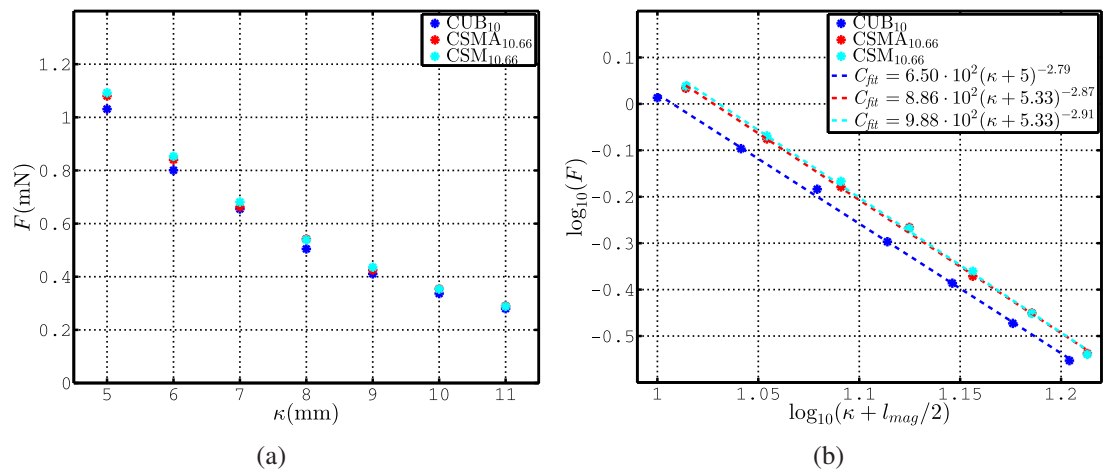


Figure 4.6: (a) F vs κ for the CUB₁₀, CSMA_{10.66} and CSM_{10.66}. (b) log-log plot illustrating the decay of F with the distance $\kappa + l_{mag}/2$.

the CSMA_{10.66} and the CSM_{10.66}, respectively. In the case of the CUB₁₀, the decay

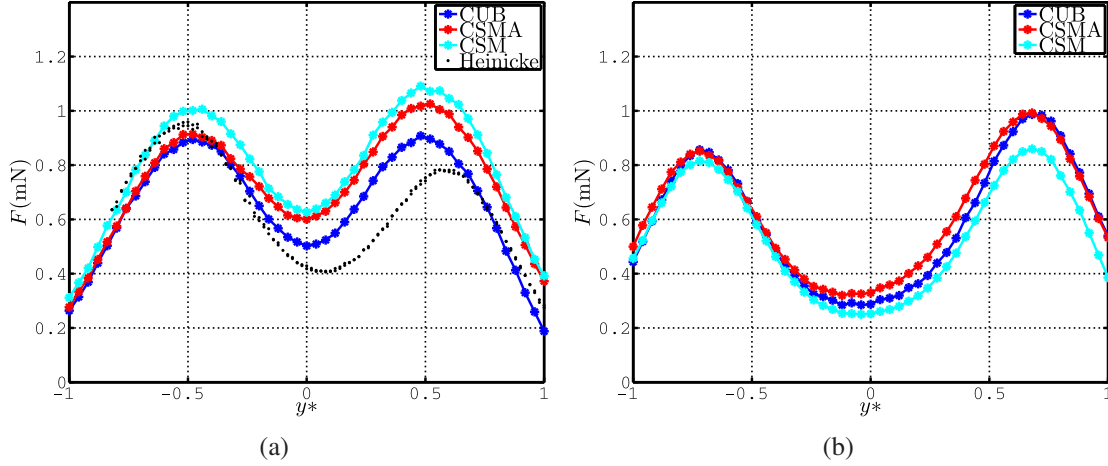


Figure 4.7: (a) Comparison between CUB_{10} , $CSMA_{10.66}$ and $CSM_{10.66}$ with a 10mm electrically insulating obstacle inside the duct. As reference, the results by Heinicke [17] using a 1.3cm obstacle are also plotted. (b) Comparison between CUB_{10} , $CSMA_{10.66}$ and $CSM_{10.66}$ with a 22mm electrically insulating obstacle inside the duct.

of F was less pronounced having $F \sim (\kappa + l_{mag}/2)^{-2.79}$. According to the numerical model from section 5.3.2, the expected decay of F for the all magnet systems should be the same or at least similar. It appears that the unexpected faster decay of the force generated by the cross-shape magnets would have been caused by a possible stronger influence of the top and bottom insulating walls of the duct or by different volume subsets of the flow spanned by the magnetic field.

In the case of the experiments with insulating cylinders immersed in the duct (figure 4.7), there were inconclusive results. For example, the measured Lorentz force was the strongest using the $CSM_{10.66}$ with the 10mm obstacle, whereas in the case with the 22mm obstacle it was the weakest. In these experiments the uncertainty increases as there is a new contribution due to the inexact position of the center of the magnet with respect to the center obstacle in the streamwise direction ($\Delta x \approx 1$ mm). Additionally, the effect of the insulating walls should be also consider as the top and bottom walls of the duct are not sufficiently away from the magnetic field generated by the permanent magnets.

4.4 Conclusions

A visible improvement of the magnitude and spatial resolution of the force was not observed by using the proposed cross-shaped magnets in comparison with the reference 10mm cubic magnet. Possible causes of these results may be explained owing to the rapid decay of the magnetic field with the distance. The effect of the cross-shaped geometry of the magnet systems is negligible for distances larger than $\kappa > l_{mag}/2$ as

it will be shown later in section 5.2. Despite these results, we cannot conclude if there is or not any advantage by using cross-shaped magnets in comparison with cubic magnets. As explain before, the uncertainty of the measured Lorentz force increases considerably when the entire set-up is readjusted for a new series of measurements using a different magnet system. In view for answering this question, a numerical model was developed. It consists on an electrically conducting disk which rotates in front of the proposed permanent magnet systems. This numerical model is described later in section 5.3.

Chapter 5

Multicomponent local Lorentz force velocimetry

This chapter focuses on multicomponent local LFV that consists on simultaneous sensing of all three force and three torque components acting on a magnet system. It will be discussed which information regarding the flow structure of the liquid metal can be inferred based on discrete distributions of local force and torque measurements across a given plane. The experiments were done at the continuous caster model, namely the mini-LIMMCAST facility, where the working fluid is GaInSn in eutectic composition. Two permanent magnet systems were considered in the experiments: a 15 mm cubic magnet and a cross-shaped magnet. The magnet systems are connected to a multicomponent force/torque sensor which has been specially designed for measuring all three force and three torque components in the range for local LFV applications. The system composed of the multicomponent force/torque sensor and the magnet system is called six-degrees-of-freedom local Lorentz force flowmeter (6D-L2F2).

According to equation (2.14), the value of the torques depends on the reference coordinate system. Hence, it is crucial to know the position of the center of the magnet system with respect to the sensor's coordinate system for an accurate torque measurement. For this purpose, a dry calibration procedure has been developed that solves this issue. Additionally, it can give a rough estimate of the calibration factor that relates the measured force and the value of the velocity of the liquid metal near the wall next to the magnet. For the dry calibration as well as for the experiments at the mini-LIMMCAST facility, numerical models have been developed for a deeper insight into the relationship between the measured local forces/torques and the information of the velocity field of the liquid metal. Some results in this chapter have been already published in the second, third and fourth references of the author's publication list and the other ones will be published in the fifth reference (Appendix: A List of publications).

This chapter is structured as follows: section 5.1 presents the 6D-L2F2 followed by the description of the magnet systems in section 5.2. Section 5.3 focuses on the concept of dry calibration for multicomponent local LFV based on a numerical model. Then, section 5.4 begins with the description of the experimental set-up at the mini-LIMMCAST facility and it will then go on with the numerical model of the experiments in section 5.5. Then, sections 5.6 and 5.7 present the experimental and numerical results using the cubic and the cross-shape magnet, respectively. Section 5.8 gives an estimate of the spatial resolution of different magnet systems based on the numerical model of the experiments at the mini-LIMMCAST facility. Finally, section 5.9 gives a summary of the main conclusions.

5.1 Multicomponent local Lorentz force flowmeter

The multicomponent/six-degrees-of-freedom local Lorentz force flowmeter (6D-L2F2) is composed of a multicomponent force/torque sensor and a magnet system. For the simultaneous multicomponent force and torque sensing in local LFV, the sensor has to be capable of measuring forces and torques acting on a permanent magnet in the range of mN and μNm , respectively. A reliable simultaneous measurement of these qualities in this range is a challenging task and such a device is not commercially available. Hence, a high-precision multicomponent force/torque sensor depicted in figure 5.1(a) was designed by the Institute of Process Measurement and Sensor Technology

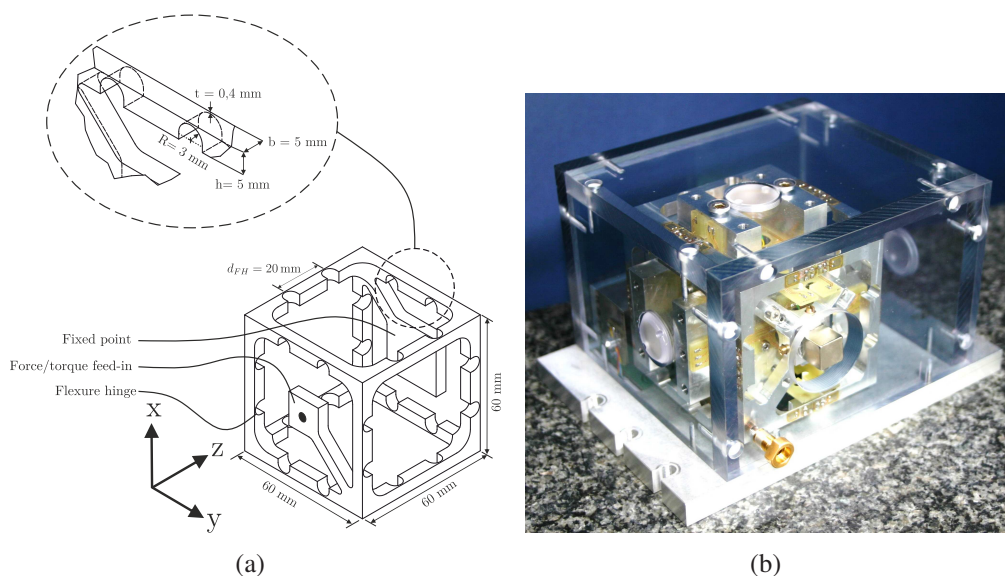


Figure 5.1: (a) Sensor consisting of six parallel springs with sensor coordinate system and parameters of flexure hinges [47]. (b) Six-degree-of-freedom force/torque sensor with permanent magnet attached to the force-feed-in for the use in multicomponent local Lorentz force velocimetry [47].

Table 5.1: Metrological parameters of multicomponent force/torque sensor [21, 47]

Parameter	Force	Torque
Components	F_x, F_y, F_z	T_x, T_y, T_z
Range	$\pm 2\text{N}$	$\pm 0.12\text{Nm}$
Resolution	$\pm 19 \cdot 10^{-6}\text{N}$	$\pm 1.4 \cdot 10^{-6}\text{Nm}$
Sensitivity	0.51mV/V/N	6.8mV/V/Nm
Eigenfrequencies	$73\text{Hz} \dots 119\text{Hz}$	$176\text{Hz} \dots 284\text{Hz}$
Maximum deformation	$\pm 0.37\text{mm}$	$\pm 5.5 \cdot 10^{-3}\text{rad}$

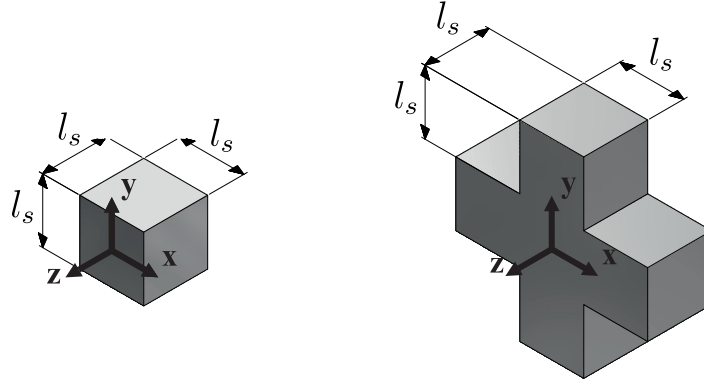
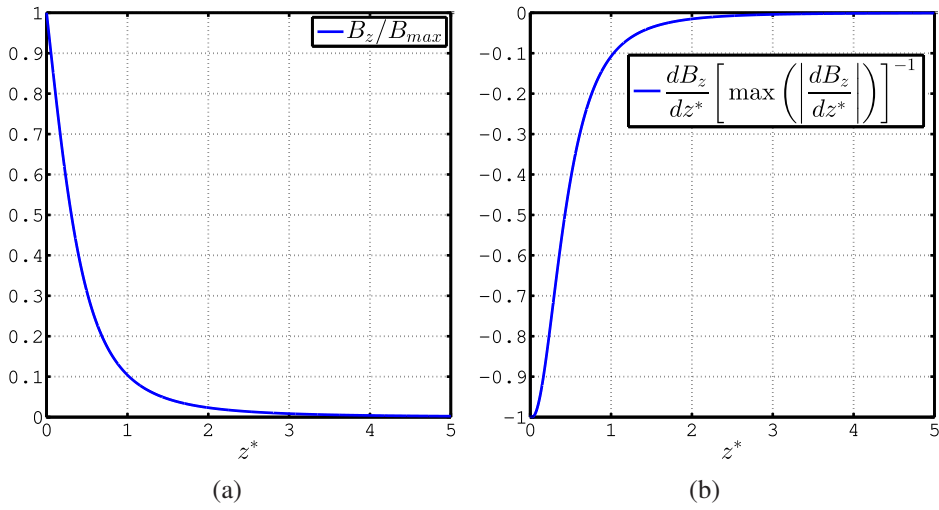
at the Technische Universität Ilmenau [43, 11]. Its parameters are summarized in table 5.1. The metrological parameters on this table were obtained by the experimental calibration procedure described in [48].

The sensor is composed of a monolithic structure of aluminum that consists of six parallel spring mechanisms. When a force or a torque is applied on the force-feed-in of the sensor, the deformation of the spring mechanisms is measured using strain gauges in form of full-bridge circuits. The output signals of the strain gauges are amplified and then digitalized up to 50kHz per channel. The multicomponent forces and torque sensor has an overload protection system for the force-feed-in and is enclosed inside an acrylic glass housing (figure 5.1(b)). The eigenfrequencies from table 5.1 can be slightly shifted when using magnets with different mass than the one used in the modal analysis. Additionally, due to the damping effect of the liquid metal, we will actually see the so-called damped eigenfrequencies in the measured signals.

5.2 Magnet systems

A cubic permanent magnet ($\text{CUB}_{l_{mag}}$) and a cross-shaped magnet ($\text{CSM}_{l_{mag}}$) were selected for the experiments at the mini-LIMMCAST facility (figure 5.2). As already explained in chapter 4, the subscript of the names of the magnets systems corresponds to their characteristic length l_{mag} . The definition of this l_{mag} will be explained further in the present section. The $\text{CUB}_{l_{mag}}$ has a side edge l_s and the $\text{CSM}_{l_{mag}}$ is composed of five cubic magnets with the same side edge. For the $\text{CUB}_{l_{mag}}$, there is an analytic solution for the magnetic field component B_z along its axis of magnetization z according to [12]

$$B_z(z) = \frac{\mu_0 M_z}{\pi} \left[\tan^{-1} \left(\frac{4(z+l_s) \sqrt{\frac{l_s^2}{2} + (z+l_s)^2}}{l_s^2} \right) - \tan^{-1} \left(\frac{4z \sqrt{\frac{l_s^2}{2} + z^2}}{l_s^2} \right) \right]. \quad (5.1)$$


 Figure 5.2: $CUB_{l_{mag}}$ with side length l_s and $CSM_{l_{mag}}$ composed of five cubic magnets (side length l_s).

 Figure 5.3: Decay of B_z (a) and dB_z/dz^* (b) along z^* for both $CUB_{l_{mag}}$ and $CSM_{l_{mag}}$.

When $z=0$, it follows from (5.1) that the maximum value of B_z along z is

$$B_{max} = B_z(z=0) = \frac{\mu_0 M_z}{\pi} \left[\tan^{-1} \left(4\sqrt{\frac{3}{2}} \right) \right]. \quad (5.2)$$

When $z = l_s$, B_z is independent from l_s so

$$B_z(z = l_s) = \frac{\mu_0 M_z}{\pi} \left[\tan^{-1} \left(8\sqrt{\frac{9}{2}} \right) - \tan^{-1} \left(4\sqrt{\frac{3}{2}} \right) \right] \approx 0.104 B_{max}. \quad (5.3)$$

It follows from (5.1) and (5.3) that the decay of B_z along the z -direction for cubic magnets can be described by the side edge l_s , which corresponds to the characteristic length $l_{mag} = l_s$ of the magnet (figure 5.3(a)). In the general case, l_{mag} can also be defined in the same way for the $CSM_{l_{mag}}$ as the point in which $B_z(z = l_{mag}) \approx 0.104 B_{max}$ along the z axis. In the case of cubic-magnet-composed CSM, $l_{mag} \approx 2.078 l_s$. Once

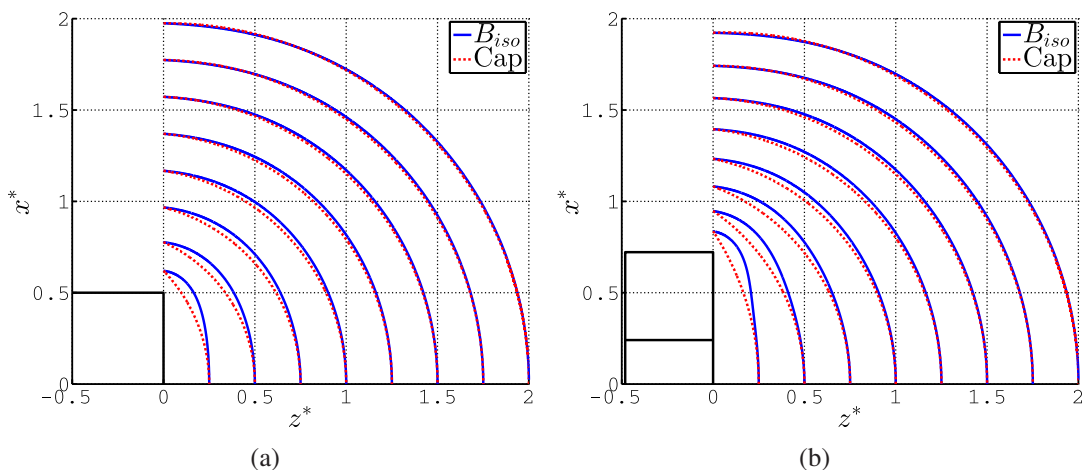


Figure 5.4: Isolines defined by B_{iso} (blue) at different values of z^* for the $CUB_{l_{mag}}$ (a) and the $CSM_{l_{mag}}$ (b). For comparison, a spherical cap (red) with height $h_{cap}^* = z^*|_{x^*=0}$ and radius of the base $a_{cap}^* = x^*|_{z^*=0}$ is plotted for each B_{iso} -isoline.

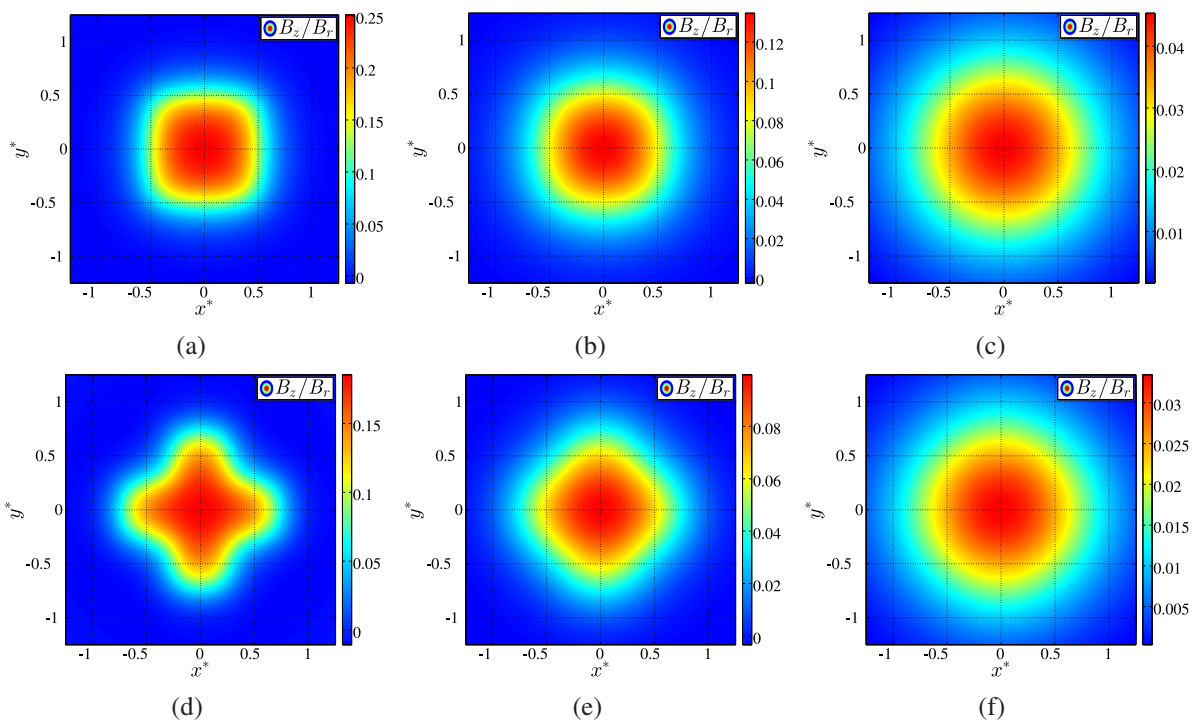


Figure 5.5: (a) B_z/B_r in the $x-y$ plane for the $CUB_{l_{mag}}$ at $z^* = 1/4$ (a), $z^* = 1/2$ (b) and $z^* = 1$ (c). B_z/B_r in the $x-y$ plane for the $CSM_{l_{mag}}$ at $z^* = 1/4$ (d), $z^* = 1/2$ (e) and $z^* = 1$ (f).

l_{mag} is defined, both magnet systems exhibit the same characteristic decay of B_z (as well as dB_z/dz^*) as a function of the normalized distance $z^* = z/l_{mag}$ (figure 5.3).

Let us now try to determine the size of the volume that is contained under isolines defined by $B_{iso} = \sqrt{B_x^2 + B_y^2 + B_z^2}$. The isolines according to B_{iso} are defined in the range $0.25 \leq z^* \leq 2$ and the results for the symmetry plane $z-x$ are shown in figure 5.4. An approximation of this volume is given by a spheri-

cal cap with height $h_{cap}^* = z^*|_{x^*=0}$ and radius of the base $a_{cap}^* = x^*|_{z^*=0}$ for each B_{iso} -isoline, where $x^* = x/l_{mag}$. According to figure 5.4, the spherical-cap assumption gives a relatively good approximation of the volume contained under a given B_{iso} -isoline for $z^* \geq 0.25$. The values a_{cap}^* can be in this case approximated as follows: $a_{cap}^* \approx 0.00062(z^*)^2 + 0.79z^* + 0.38$ for the CUB $_{l_{mag}}$ and $a_{cap}^* \approx 0.023(z^*)^2 + 0.61z^* + 0.62$ for the CSM $_{l_{mag}}$ in the range $0.25 \leq z^* \leq 5$.

Now let us consider the characteristic decay of B_z in the $x - y$ plane at different values of z^* (figure 5.5). In this case B_z is normalized by the remanent magnetization of the magnet B_r . According to figures 5.5(b) and 5.5(e), B_z does not longer exhibit a pronounced non-axisymmetric distribution regarding both magnet systems for $z^* > 1/2$.

The developed numerical model from section 5.5 was used to predict the expected magnitude of the torque T_z perpendicular to the mold of the mini-LIMMCAST facility using a CSM. The conclusion was that the size of the CSM should be at least $l_s = 15$ mm ($l_{mag} = 31.17$ mm). In this case, the expected magnitude of the torque T_z at the mini-LIMMCAST facility is in the measuring range of the 6D-L2F2. The geometry and parameters of the magnet systems used in the experiments in this chapter are summarized in table 5.2.

Table 5.2: Parameters of the permanent magnets.

Parameter	CUB $_{15}$	CSM $_{31.17}$
l_{mag}	15 mm	31.17 mm
Volume	15^3 mm 3	$5 \cdot 15^3$ mm 3
Grade	N48	N52
B_r	1.357 T	1.43 T
M_z	$1.080 \cdot 10^6$ A/m	$1.138 \cdot 10^6$ A/m
$B_z(z = 0)$	0.62 T	0.46 T

5.3 Dry calibration

As it has been already mentioned in section 2.3.1, LFV has in general the disadvantage that a calibration factor K_v has to be determined beforehand in order to obtain the corresponding flow rate or local velocity from a force measurement. However, multi-component local LFV has an additional challenge in comparison with the traditional Lorentz force flowmeter: one needs to identify accurately the position of the center of the magnet system with respect to the coordinate system of the force/torque sensor. When this position is unknown, it is not possible to have an accurate measurement of

the torques acting on the magnet system. Additionally, there are no analytical, numerical or similar experimental works previous to the ones treated on this thesis from which a prediction of the magnitude or behavior of T_z in liquid metal could be performed. T_z is the torque component pointing in the same direction of magnetization of the magnet.

According to section 5.6, T_z was not accessible at the first experimental campaign at the mini-LIMMCAST facility using the CUB₁₅. These results have left the following open questions regarding this torque T_z which is orthogonal to the surface of the mold: (i) what is its order of magnitude?, (ii) can this torque be measured in liquid metals with the 6D-L2F2?, (iii) which information regarding the flow distribution does this torque represent? Before performing new series of experiments using different magnet systems at the mini-LIMMCAST facility, a dry calibration procedure is proposed in which the flowing liquid is replaced by a moving solid (see figure 5.6). Here, the moving solid is a rotating disk made of aluminum whose velocity field is fixed and steady, and therefore, known. Hence, the variability and the noise of the measurements are considerably decreased providing an accurate calibration of the system. This allows us to find the center of the magnet on which the torques and forces originating from the liquid act.

The concept of a permanent magnet in front of an electrically conducting rotating disk was used in the past for velocity measurements in eddy current velocity indicators. This idea was patented in 1903 by Otto Schultze in his work "Improvements in Speed Indicators" [49], in which his invention was connected to the part of the machine whose velocity one wants to measure. The measured torque is proportional to the rotation velocity of the disk. However, it is not entirely clear what would be the behavior

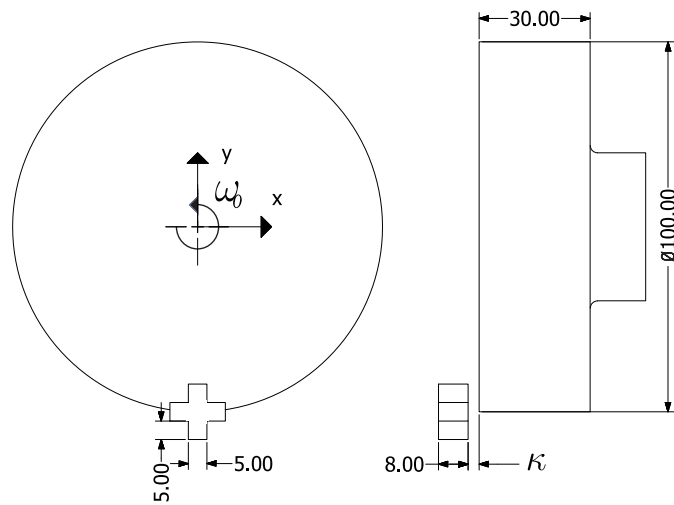


Figure 5.6: Dry calibration of the 6D-L2F2. Test principle: a permanent magnet system is placed in front of an electrically conducting disk which rotates at a constant angular velocity ω_0 . In the figure, the cross-shape permanent magnet CSM_{10,66} is shown and its center is placed at $(0, -50\text{ mm})$. The surface of the magnet is at a distance κ away from the disk.

of this torque when the permanent magnet is considerably smaller than the disk like in local LFV. In the following sections it is shown that this torque is constant across the surface of the disk except near the edge and proportional to the angular velocity. The magnet systems used in the numerical model are the CSM_{10.66} (or CSMA_{10.66}) and the CUB₁₀ from section 4.1.

5.3.1 Numerical model

A permanent magnet system is placed in front of an electrically conducting disk with conductivity σ_{disk} at a distance κ . The geometry of the disk is the same as the one used for the calibration procedure of the 6D-L2F2 with the CSM_{31.17} (section 5.3.5). The velocity field of the rotating disk shown in figure 5.6 is

$$\vec{u} = \omega_0 \vec{e}_z \times \vec{r}, \quad (5.4)$$

where the vector $\vec{r} = x \cdot \vec{e}_x + y \cdot \vec{e}_y$ denotes the position. From introductory books of fluid dynamics [29], it is known that the vorticity of the velocity field for a solid-body rotation

$$\omega_z = (\nabla \times \vec{u}) \cdot \vec{e}_z = 2\omega_0 \quad (5.5)$$

is constant in every point of the disk and proportional to the angular velocity ω_0 . First (2.11) is solved for insulating boundary conditions and then \vec{j} , \vec{F} and \vec{T} are obtained through (2.10), (2.13) and (2.14), respectively. Here, the torques are calculated at the center of the magnet system. The mesh is composed of about $1.62 \cdot 10^5$ non-uniform second-order hexahedral elements ($1.33 \cdot 10^6$ DoF) that take into account the decay of the magnetic field with the distance in the axial direction of the disk.

5.3.2 Results

The following parameters were considered in the present numerical model: $\omega_0 = 1$ Hz, $\sigma_{disk} = 24.5$ MS/m, $\kappa = 1 \dots 5$ mm. Here, the CSM_{10.66} scans the surface of the disk from $(x = -50$ mm, $y = -50$ mm) to $(x = 50$ mm, $y = 50$ mm) with a grid resolution of 5 mm and $\kappa = 3$ mm. It is observed that the force is tangential and grows linearly with the distance from the center (figure 5.7(a)), whereby it decreases significantly and decays to zero outside the disk. According to figure 5.7(b), the torque component perpendicular to the surface of the disk T_z is indeed constant in a region sufficiently away from the rim. By comparing the value of T_z for the CSM_{10.66} and CUB₁₀ magnet systems, figure 5.7(c) shows that there is an important increase of about 9 times higher torque by using the CSM_{10.66} in the region with constant T_z . However,

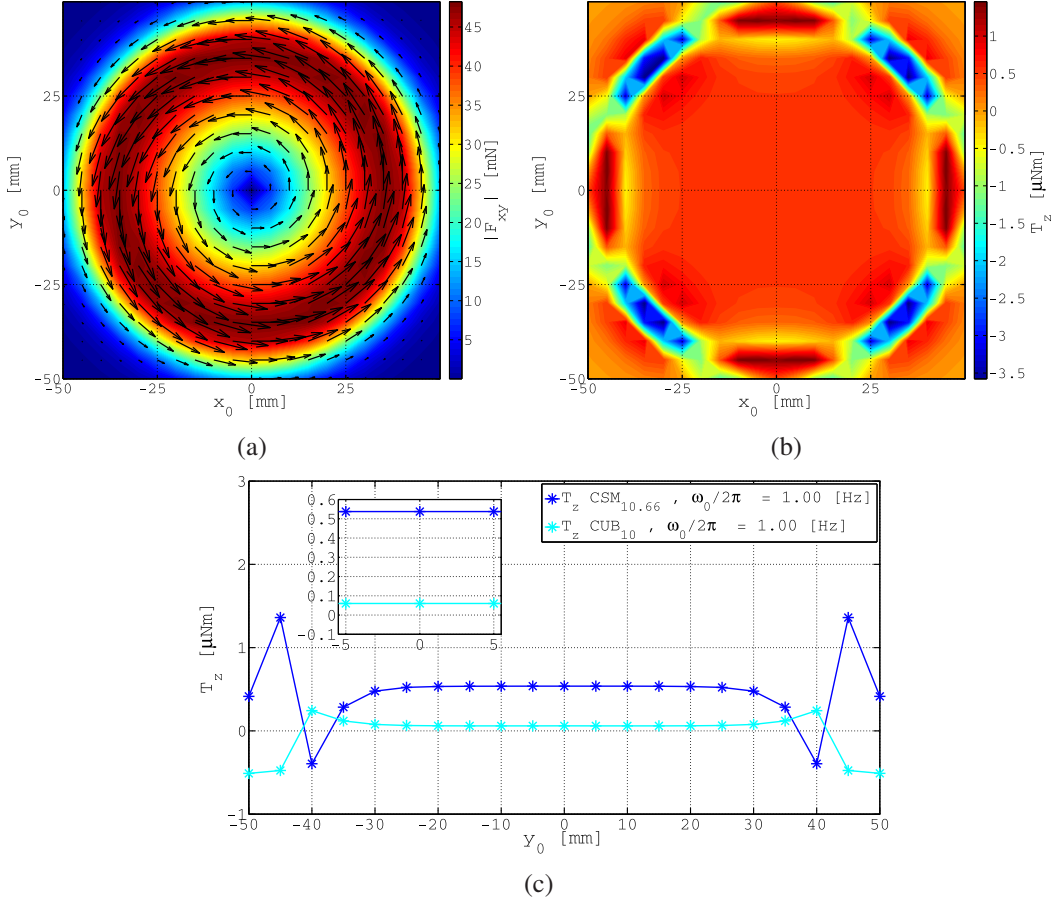


Figure 5.7: Contour plots regarding F_{xy} (a) and T_z (b) for the CSM_{10.66}. The vector and contour plots in (a) were calculated based on F_x and F_y , where the contour plot corresponds to the magnitude and the vectors to the direction of the total force at the position of the center of the magnet (x_0, y_0) . The torque component perpendicular to the surface of the disk T_z (b) is constant in the region where the magnet is sufficiently far away from outer boundaries. (c) Torque component T_z acting on the CSM_{10.66} and CUB₁₀ magnet systems from $(0, -50 \text{ mm})$ to $(0, 50 \text{ mm})$. The torque T_z is proportional to the angular velocity of the disk and constant in the region between $y_0 \approx -20 \text{ mm} \dots 20 \text{ mm}$. The CSM_{10.66} experiences around 9 times higher torque than the 10 mm cubic magnet. *Parameters:* CSM_{10.66} and CUB₁₀, $\omega_0/2\pi = 1 \text{ Hz}$, $\kappa = 3 \text{ mm}$.

its magnitude ($0.53 \mu\text{Nm}$) is still smaller than the measuring range of the 6D-L2F2 for $\omega_0 = 1 \text{ Hz}$. Nevertheless, as T_z is proportional to ω_0 , higher rotation frequencies can be used in future calibration experiments. In the case of higher angular velocities, the magnet system should be placed near the center of rotation of the disk in order to avoid finite R_m effects by high relative velocities.

Owing to the rapid decay of magnetic fields, the magnitude of the forces and torques are strongly sensitive to the distance between the magnet and the flowing liquid metal or moving electrically conducting solid. According to (2.16) and (2.17), the force scales $\sim \kappa_{dip}^{-3}$ and the torque $\sim \kappa_{dip}^{-2}$ for a magnetic dipole, where κ_{dip} denotes the distance between the dipole and a semi-infinite moving plate (see section 2.2). However, this scaling factors may differ when the permanent magnets are very close and

5. Multicomponent local Lorentz force velocimetry

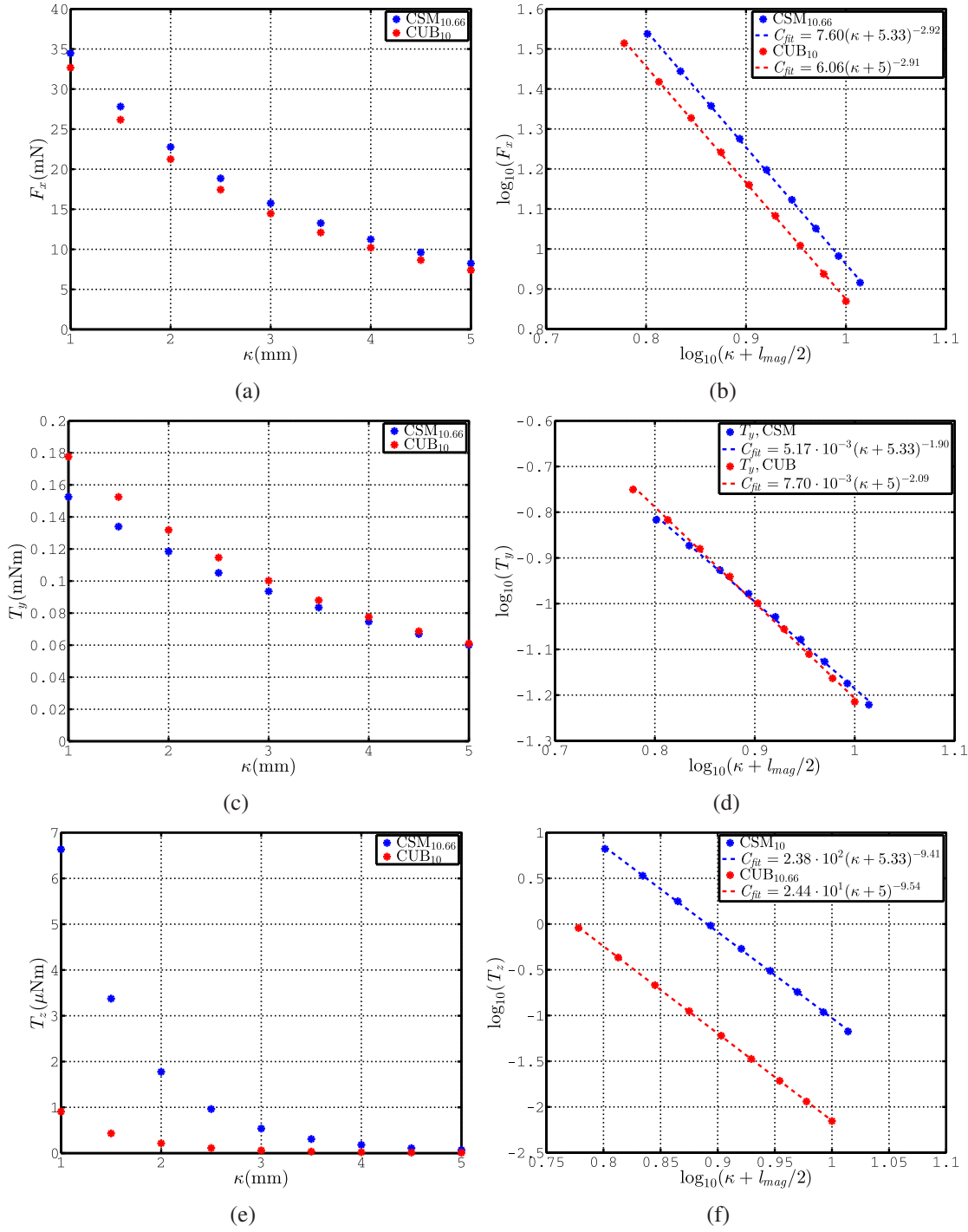


Figure 5.8: Decay of the force component F_x (a) and the torque components T_y (c) and T_z (e) for the CSM_{10.66} and CUB₁₀ as a function of κ at (0,10mm). log-log plots illustrating the decay of F_x (b), T_y (d) and T_z (f) with the distance $\kappa + l_{mag}/2$.

non-axisymmetric magnetic field distributions are applied on the solid. Therefore, the effect of κ variations on the forces and torques acting on the magnet are also investigated in the present numerical model. In this sense, the CSM_{10.66} and CUB₁₀ are placed at (0,10 mm) in the y -axis in order to have a value of T_z and a single force F_x in

the $x - y$ plane, whereby a torque T_y is also additionally induced. Then, the distance between the surface of the magnet and the disk κ is increased from 1 mm to 5 mm in 0.5 mm steps. Figure 5.8 summarizes the results for the corresponding decay of F_x , T_y and T_z as a function of κ for the CUB₁₀ and the CSM_{10.66}. A fitting model is suggested for a quantitative assessment of this decay

$$C_{fit} = a \cdot (\kappa + l_{mag}/2)^b, \quad (5.6)$$

where C_{fit} corresponds to the force or torque value, and a and b to the model parameters, respectively. Here, $l_{mag} = 10.66$ mm and $l_{mag} = 10$ mm for the CSM_{10.66} and the CUB₁₀, respectively. l_{mag} for these magnet systems was obtained following the procedure previously explained in section 5.2. According to the fitting model, the force F_x and the torques T_y and T_z scale with the distance $\kappa + l_{mag}/2$ as $\sim (\kappa + l_{mag}/2)^{-2.92}$, $\sim (\kappa + l_{mag}/2)^{-1.90}$ and $\sim (\kappa + l_{mag}/2)^{-9.41}$ for the CSM_{10.66}, respectively. In the case of the CUB₁₀, the force F_x and the torques T_y and T_z scale with the distance $\kappa + l_{mag}/2$ as $\sim (\kappa + l_{mag}/2)^{-2.91}$, $\sim (\kappa + l_{mag}/2)^{-2.09}$ and $\sim (\kappa + l_{mag}/2)^{-9.54}$. The decay of T_z is approximately 5 times stronger than T_y , which appears to be the least sensitive component with respect to κ variations. Despite the fact that the decay of F_x , T_y , and T_z is similar for both magnet systems, the force component F_x and the torque component T_z are stronger due to the non-axisymmetric magnet field distribution, whereas the T_y component was weaker. The reason of the more rapid decay of T_z is due to the strong dependence of the non-axisymmetric magnetic field distribution of cross-shaped magnets on the distance. As already shown in section 5.2, the non-axisymmetric magnet field distribution of a CSM or a CUB is in general not highly pronounced for $\kappa > l_{mag}/2$ and is almost totally axisymmetric for $\kappa > l_{mag}$. In figure 5.8 it can be observed that there is no noticeable difference regarding F_x , T_y and T_z between both magnets systems for $\kappa > l_{mag}/2$.

In conclusion, an optimal magnetic field distribution in the disk is needed for measuring the torque T_z acting on the magnet system. An axisymmetric magnetic field on the disk does not favor the generation of the T_z component, as it has been observed in the present numerical model. This statement is confirmed analytically in the next section. Therefore, when the magnet is sufficiently away from the surface of the disk, the field approaches an axisymmetric shape that does not provide an axial torque component T_z . In the numerical study it is confirmed that, by using a cross-shaped permanent magnet system, the torque T_z perpendicular to the surface of a rotating disk is considerably higher in comparison with a reference cubic permanent magnet. This torque can provide information on the local curl of the velocity field, which for a rotating disk is constant and proportional to the angular velocity.

5.3.3 Two-dimensional limit

The analytical model in this section is the result of private communication with Thomas Boeck (TU Ilmenau). A particular feature of the velocity field (5.4) is that the curl of the electromotive force $\vec{u} \times \vec{B}_0$ is curl-free. This can be shown by direct calculation of $\nabla \times (\vec{u} \times \vec{B}_0)$ using $\nabla \cdot \vec{B}_0 = 0$ and $\nabla \times \vec{B}_0 = 0$. The result is

$$\nabla \times (\vec{u} \times \vec{B}_0) = \nabla(\omega_0 \vec{e}_z \cdot (\vec{B}_0 \times \vec{r})). \quad (5.7)$$

Since the curl of the current density \vec{j} differs from (5.7) only by the prefactor σ_l , it follows that $\nabla \times \vec{j}$ is also curl-free, i.e.

$$\nabla \times (\nabla \times \vec{j}) = \nabla(\nabla \cdot \vec{j}) - \nabla^2 \vec{j} = 0. \quad (5.8)$$

Because $\nabla \cdot \vec{j} = 0$, it follows from (5.8) that each component of the current density satisfies the Laplace equation, in particular, the axial component j_z . On the surfaces $z = \text{const}$ of the disk we have $j_z = 0$ as boundary conditions. At the (outer) rim of the disk there can be a component j_z . However, this component should become negligible when the magnet is sufficiently far away from it such that there is no significant electromotive force at the rim. In this case, j_z satisfies the Laplace equation with homogeneous Dirichlet boundary conditions. The solution is then $j_z = 0$ throughout the disk, i.e. the current density is strictly two-dimensional.

When this limit applies, one can represent the solenoidal current density by a stream function $\psi(x, y)$, i.e.

$$\vec{j} = \nabla \times \psi(x, y) \vec{e}_z. \quad (5.9)$$

With this representation it then follows from Ohm's law that

$$-\vec{e}_z \cdot (\nabla \times \vec{j}) = \frac{\partial^2 \psi}{\partial x^2} + \frac{\partial^2 \psi}{\partial y^2} = \sigma_{disk} \omega_0 [\vec{e}_z \cdot (\vec{r} \times \nabla)] B_z. \quad (5.10)$$

This two-dimensional Poisson equation depends parametrically on z . On the outer boundary the current density is tangential to the rim, i.e. the rim is a streamline $\psi = \text{const}$.

The effects of magnet position are fairly obvious in the two-dimensional formulation when the disk has infinite radius. Assuming that the center of the magnet is at $\vec{r}_0 = (x_0, y_0, z_0)$, one can decompose the right-hand side of eq. (5.10) as

$$\sigma_{disk} [\omega_0 \vec{e}_z \cdot ((\vec{r} - \vec{r}_0) \times \nabla)] B_z + \sigma_{disk} [\omega_0 \vec{e}_z \cdot (\vec{r}_0 \times \nabla)] B_z, \quad (5.11)$$

where the first term corresponds to a rotation about \vec{r}_0 and the second one to a translation with velocity $\omega_0 \vec{e}_z \times \vec{r}_0$. The solution of (5.10) is then a superposition of the current distributions corresponding to a rotation and a translation, respectively. The translation can be decomposed further into a translation along x and one along y . In conclusion, the solution is

$$\psi = \sigma_{disk} \left(\omega_0 \psi^{(r)} + \omega_0 x_0 \psi^{(y)} - \omega_0 y_0 \psi^{(x)} \right), \quad (5.12)$$

where $\psi^{(r)}$ is the solution for a pure rotation about z and $\psi^{(x)}$, $\psi^{(y)}$ are solutions for pure translations along x and y , respectively.

From the decomposition (5.11) it is obvious that an axisymmetric magnetic field (about the z -axis) does not generate a contribution $\psi^{(r)}$ since the axial field component is then given by $B_z(\sqrt{(x-x_0)^2 + (y-y_0)^2})$, whereby the source term cancels. For symmetry reasons, this contribution is the only source of axial torque. A pure translation will only cause a drag force in the same direction. The translational contributions $\psi^{(x)}$ and $\psi^{(y)}$ clearly differ by a rotation of coordinates through a right angle about the z -axis. As a result of (5.12), the resulting planar force components satisfy

$$F_x = -\omega_0 y_0 F_x^{(0)}, \quad F_y = \omega_0 x_0 F_y^{(0)}, \quad (5.13)$$

where the value $F_x^{(0)}$ corresponds to a translation with unit velocity along x , and $F_y^{(0)}$ to a translation with unit velocity along y .

This two-dimensional problem has been also implemented numerically based on the stream function ψ . In this case we solve (5.10) for equidistantly spaced layers $z = \text{const}$ in COMSOL and compute the current and Lorentz force densities from ψ . The total force and torque are obtained by subsequent summation of the contributions from these layers.

5.3.4 Calibration factor

This section describes a method based on dry calibration for estimating the calibration factor that relates the measured force in local LFV and the local velocity of the liquid metal. A quantitative assessment of the magnitude of the velocity field u' of the liquid metal can be obtained by

$$u' = K_{liq} \cdot F, \quad (5.14)$$

where F is the magnitude of the measured force component and K_{liq} the calibration factor. However, one of the biggest difficulties in local LFV is that K_{liq} does not only

strongly depend on the distance between the permanent magnet and the liquid metal, but also on the velocity distribution near the wall spanned by the magnetic field. Let's say that in two points of the measuring grid the force F is the same. It may occur, however, that in the first point the velocity is lower but closer to the wall, whereas in the second point the velocity is higher but located deeper in the liquid. This situation will be later discussed in section 5.6.1, where it is shown that this uncertainty can be decreased by comparing simultaneously the distributions of force and torque. In application, the velocity field in a given set-up is unknown and we need to define K_{liq} *a priori* for not only to have a qualitative but also a quantitative assessment of the magnitude of velocity of the liquid metal. In this sense, the dry calibration idea can be used to estimate K_{liq} as follows

$$K_{liq} = K_{disk} \frac{\sigma_{disk}}{\sigma_l}, \quad (5.15)$$

where K_{disk} and σ_{disk} are the calibration factor and conductivity of the disk, respectively. K_{disk} is the ratio of the velocity field in the disk to the force acting at the center of the magnet at (x_0, y_0) . The position of the center of the magnet is sufficiently away from the rim of the disk in which the force is proportional to the radius \vec{r} . An example of this procedure is given in section 5.6.2.

5.3.5 Calibration set-up

The dry calibration concept was developed after the experiments at the mini-LIMMCAST facility using the CUB₁₅ (section 5.6). Therefore, the dry calibration procedure was experimentally done only for the CSM_{31.17} attached to the multicomponent force/torque sensor for the second measurement campaign. The calibration experiments were performed by Rafael Marangoni (TU Ilmenau) using the calibration set-up shown in figure 5.9(a). The measurements of all force and torque components were done by scanning an area of 8 mm × 8 mm over the disk's surface around the center. Based on the F_x and F_y distribution (figure 5.9(b)) and due to the fact that T_z is constant in this region sufficiently away from the rim of the disk, the exact position of the magnet center with respect to the sensor's coordinate system could be defined accurately. After this calibration procedure, it is possible to measure the forces and torques that act at the center of the magnet, specially T_z , which can be about two orders of magnitude smaller than the other two torque components. More detailed information of these experiments can be found in the fifth reference of the author's publication list.

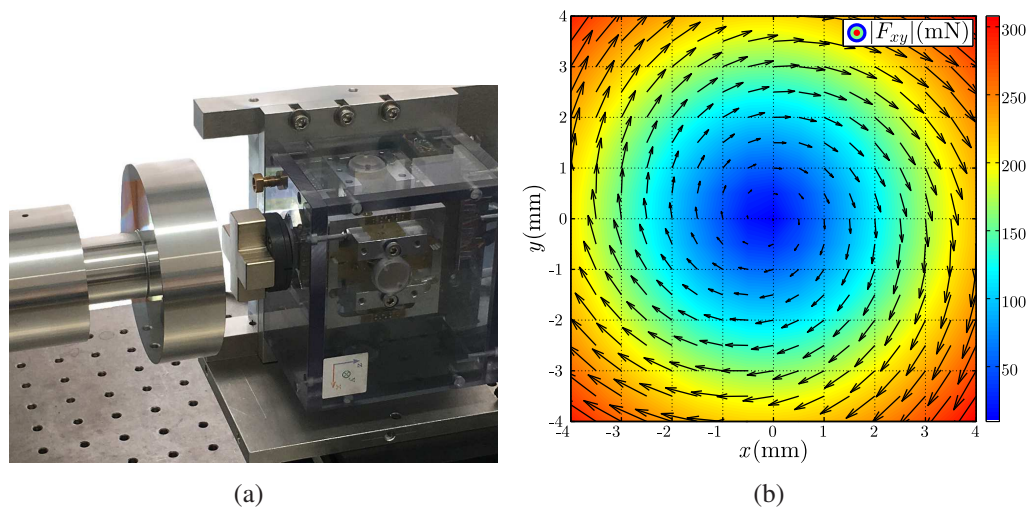


Figure 5.9: (a) Experimental set-up showing the CSM_{31.17}, multicomponent force/torque sensor and rotating disk. (b) Measured Lorentz force \vec{F} acting on the CSM_{31.17}.

5.4 Experimental set-up mini-LIMMCAST

The mini-LIMMCAST facility (LIquid Metal Model of continuous CASTing of steel) is a model of a continuous caster available at Helmholtz-Zentrum Dresden-Rossendorf. Continuous casting of steel is the casting process in which molten steel solidifies into billets or slabs. Since decades, it has been the dominant casting technology due to its advantages in terms of cost for large-tonnage operations. A sketch of a continuous casting installation is depicted in figure 5.10(a). The liquid steel flows from the ladle into the tundish, which acts as a buffer vessel or reservoir holding sufficient material to provide a continuous liquid metal flow. From the tundish, the liquid steel flows to the water-cooled copper mold through the submerged entry nozzle (SEN). The casting speed, and therefore, the flow through the SEN is regulated by the position of the stopper rod. In the mold, the liquid metal starts to solidify having a solid shell of some centimeters in thickness while the interior is still liquid. The flow field in the mold is critical in order to avoid flow-related problems like slag entrainment and surface quality problems. The ideal flow structure in the mold is characterized by a symmetric double-roll flow which has an inward flow at the meniscus as shown in figure 5.10(a). This type of flow field is desired as it guides the impurities and bubbles to the free surface avoiding its intrusion into the solid steel [30, 75]. Therefore, the quality of the molten steel depends strongly on the flow regime on the upper part of the mold. A lot of effort has been invested on the understanding, measuring, simulating and optimization of the process [60].

In the case of the mini-LIMMCAST facility (figure 5.10(b)), the working fluid is GaInSn in eutectic composition whose electrical conductivity is $3.3 \cdot 10^6 \pm 3 \cdot 10^4$ S/m

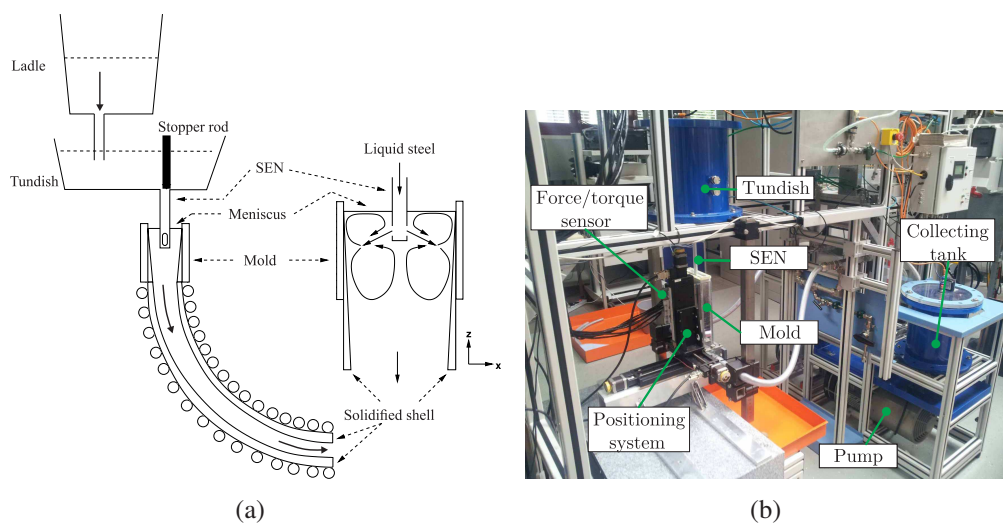


Figure 5.10: (a) Schematic sketch of a continuous casting installation [74]. (b) Mini-LIMMCAST facility with electromagnetic pump, tundish, SEN and mold together with positioning system and 6D-L2F2 on granite stone [21].

at 20°C [37]. In this set-up different flow phenomena have been investigated [56, 61] as well contactless velocity measurement techniques for liquid metals [45, 73]. The tundish is represented by a stainless steel cylinder which contains 5 – 6l of the melt. The position of the stopper rod controls the flow of the liquid metal from the tundish into the submerged entry nozzle (SEN). In the experiments, the stopper rod is lifted about 20mm, which corresponds to an average flow velocity of 1.5 m s^{-1} (0.121 s^{-1}) inside the SEN ($Re = 4.4 \cdot 10^3$). From the outlet of the SEN, the liquid metal flows into the acrylic glass mold which has a cross-section of $140\text{ mm} \times 35\text{ mm}$ ($Re = 2.5 \cdot 10^3$ with l_c being the width of the mold). The SEN is also made of acrylic glass and its inner diameter is 10mm. At the bottom of the mold, the metal melt flows through flexible tubes back to the collecting tank. Then, an induction pump drives the liquid from the collecting tank back to the tundish. The level of the melt in the tundish is kept constant by controlling the flow rate of the pump, thereby producing a steady flow in the mold. The level of liquid metal in the tundish and in the mold is monitored by a laser system and an ultrasonic distance sensor, respectively. The 6D-L2F2 was fixed to a positioning system composed of a 3-axis linear stage which was mounted on a granite stone. The stone is totally decoupled from the mini-LIMMCAST facility in order to isolate the sensor from vibrations or noise from the pump during experiments.

5.4.1 Measurement procedure

In order to obtain a velocity assessment of the velocity field inside the mold, the permanent magnet systems are placed in front of the wide face leaving an air gap of

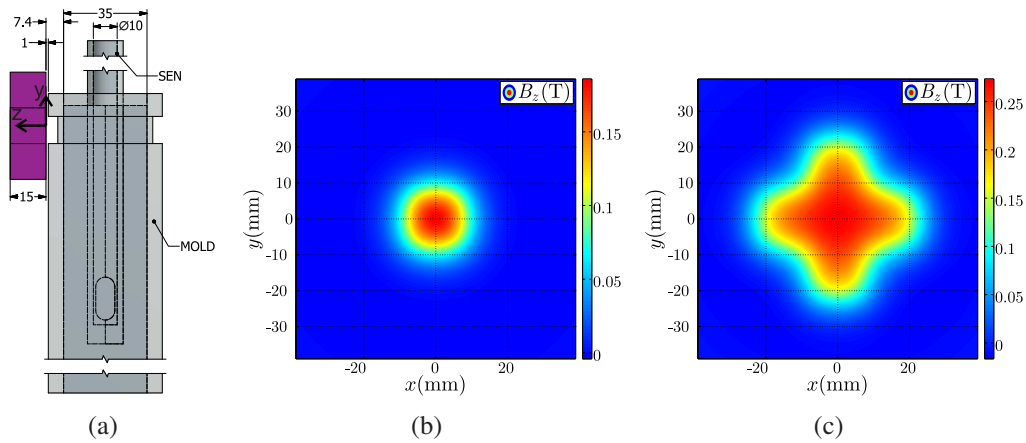


Figure 5.11: (a) $z-y$ view of the mini-LIMMCAST facility presenting the CSM_{31.17} (magenta) whose center is located at $(x = 0\text{ mm}, y = 0\text{ mm}, z = 7.5\text{ mm})$, leaving an air gap of 1 mm. The center of the CUB₁₅ as well as the center of the CSM_{31.17} in simulation and experiments are located at the same points for comparison. Magnetic field distribution of B_z at $z = -7.4\text{ mm}$ for the CUB₁₅ (b) and the CSM_{31.17} (c). The magnetic field of the CSM_{31.17} exhibits a clear non-axisymmetric distribution which is needed for the measurement of T_z .

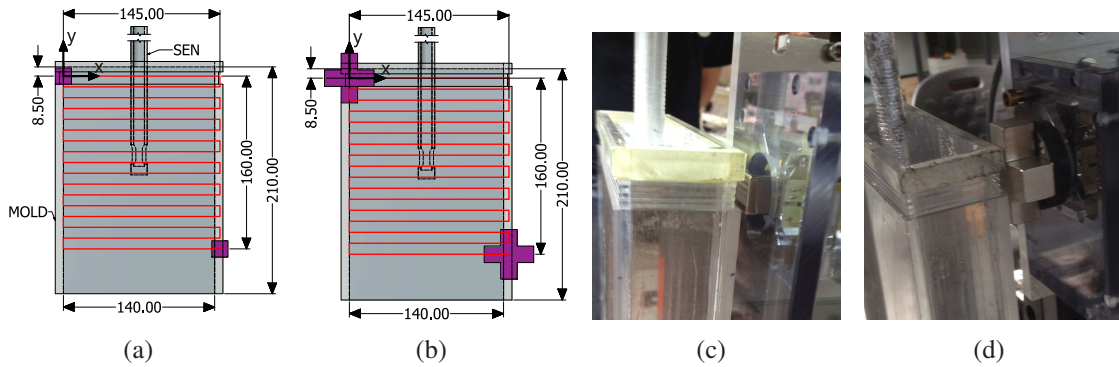


Figure 5.12: Sketch of the mini-LIMMCAST facility presenting the measuring grid and the location of the CUB₁₅ (a) and the CSM_{31.17} (b) (magenta) at the beginning ($x = 0\text{ mm}, y = 0\text{ mm}$) and at the end of the experiment ($x = 145\text{ mm}, y = -160\text{ mm}$). Photo of the experimental set-up showing the magnet systems CUB₁₅ (c) and CSM_{31.17} (d) at the beginning of the experiment.

about 1 mm (figure 5.11(a)). At the beginning of the measurements, the center of the magnet was placed at $(0\text{ mm}, 0\text{ mm})$ and then, the magnet follows a zig-zag movement maintaining a step size of 10 mm in the x - and in y -directions as shown in figure 5.12(a). When the magnet reaches 140 mm, it takes an additional step of 5 mm in order to cover the entire width of the acrylic glass wall. According to this zig-zag movement, the center of the magnet covers an area between $(0,0)$ and $(145,-160)$ having in total $16 \times 17 = 272$ measuring points. In each point from this measuring grid, the time-average is taken from each of the three force and torque components in a time slot of five seconds at a sampling frequency of 2 kHz. The selection of the time interval of 5 seconds is a compromise between measurement time for averaging at each position and the run time of the entire scan, during which the flow has to be stationary.

In this case, a complete measurement across the entire measuring path takes around 2 h. In total, two measurements are carried out. First, a measurement is performed without fluid flow in order to measure the local offset of the force and torque signals due to ferromagnetic materials in the environment. Then, the mini-LIMMCAST facility operates in continuous mode and the second measurement is performed. The final force and torque distributions across the measuring path ($F_x, F_y, F_z, T_x, T_y, T_z$) are obtained by subtracting the offset from the results of the second measurement with fluid flow. The measurements in comparison with the numerical results are shown in section 5.6 and section 5.7 for the CUB₁₅ and the CSM_{31.17}, respectively.

5.5 Numerical model

As already explained in chapter 2, the numerical model of the experiments at the mini-LIMMCAST facility is based on the low- R_m approximation of Ohm's law for electrically moving liquids and also on the premise that the flow is not affected by the applied magnetic field ($N < 1$). The third and final assumption is that the velocity field of the liquid metal in the mold is steady. In local LFV using a single multicomponent sensor, the components of force and torque can only be measured for a single domain of the flow at a time. In order to obtain a force or torque distribution, it is necessary to scan the mold in a pointwise manner assuming a steady velocity field. Hence, if the velocity field were not steady, it might be impossible to identify general patterns of the flow based on the force or torque distributions across the wide face of the mold. Fortunately, this assumption is appropriate for the mini-LIMMCAST facility as it was observed in the first measurement campaign using the CUB₁₅ (see section 5.6). Thus, a simulated steady flow structured in the mold previously used in [74] is the source of the velocity field \vec{u} in the numerical model. Here, \vec{u} was obtained from a CFD simulation using the finite-volume solver OpenFoam and a $k - \omega$ turbulence model, which was validated with UDV measurements. For this purpose just one quarter of the volume of the mold was meshed and solved for a steady state solution with pre-supposed symmetries (half width of the mold in the z -direction and half length of the mold in the x -direction).

In order to decrease computing time, just the upper part of the mold with height $h = 210$ mm is analyzed (in [74] $h = 330$ mm). This height is sufficient to avoid the influence of the bottom wall on the solution. Hence, the velocity field \vec{u} is confined in a rectangular mold with dimensions 140 mm \times 35 mm \times 210 mm. Figure 5.13 shows the streamlines of the velocity field inside the mold of the mini-LIMMCAST facility based on \vec{u} . The sidewalls are electrically insulating as well as the top and bottom walls.

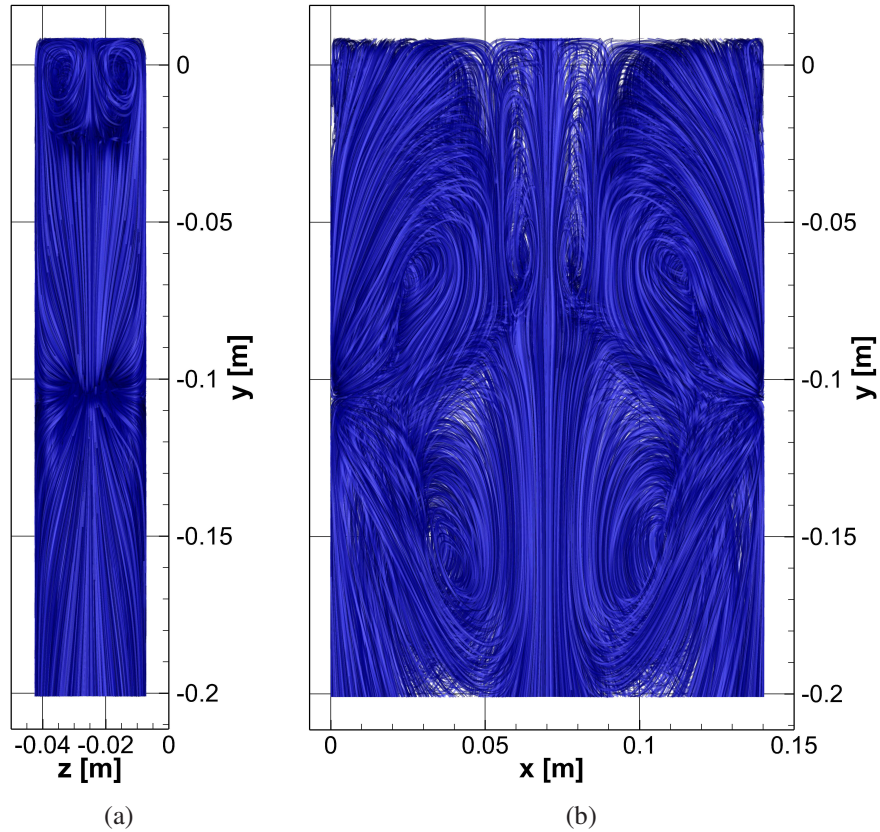


Figure 5.13: (a) $z-y$ and (b) $x-y$ view of the velocity field streamlines inside the mold of the mini-LIMMCAST based on \vec{u} .

Here, the SEN is modeled as a part of the liquid metal but with $|\vec{u}| \approx 0 \text{ m s}^{-1}$, contrary to experiments in which SEN is insulating. As the SEN is at a distance $|z| > 17.4 \text{ mm}$ away from the surface of the magnet systems, the influence of its conductivity on the solution is assumed negligible.

The mesh of the numerical model is composed of non-uniform second-order hexahedral elements. The structure of the non-uniform mesh is defined by the following parameters: number of grid lines along x , y and z , with N_x , N_y and N_z , respectively. The grid lines due to N_x and N_y are uniformly distributed along their corresponding axis, whereas the ones due to N_z are clustered in the z -direction near the wall next to the magnet system. Regarding grid convergence, for $N_x = 143$, $N_y = 157$ and $N_z = 60$, in comparison with $N_x = 72$, $N_y = 79$, $N_z = 30$, the error is less than 1%. The finer mesh is used for the numerical model of the CUB₁₅ and the CSM_{31.17} magnet systems. In total we have about $1.35 \cdot 10^6$ elements, i.e. $1.1 \cdot 10^7$ degrees of freedom. First, ϕ is obtained by solving (2.11) for insulating boundary conditions. Then, \vec{j} , \vec{F} and \vec{T} are calculated using (2.10), (2.13) and (2.14), respectively. The forces and torques using the numerical model (F'_x , F'_y , F'_z , T'_x , T'_y , T'_z) are given for the same points of the measuring grid for comparison.

5.6 Results using the CUB₁₅

The numerical model is validated by comparing the distributions of the measured ($F_x, F_y, F_z, T_x, T_y, T_z$) and simulated ($F'_x, F'_y, F'_z, T'_x, T'_y, T'_z$) force and torque components across the wide face of the mold for the CUB₁₅ magnet system. The torques are calculated at the center of the sensor's coordinate system which is defined by calibration and located at $z=48.5$ mm. The results are summarized in contour and vector plots, where the contour plot shows the magnitude, e.g. $F_{xy} = (F_x^2 + F_y^2)^{1/2}$, and the vector plot the direction of the two-component force and torque. In the case of the vector plot based on T_x, T'_x , and T_y, T'_y , the values of T_x and T'_x are plotted in y -direction and the values of $-T_y$ and $-T'_y$ are plotted in x -direction in order to obtain the expected double-roll structure of the velocity field. For a better visualization of the results, equally-spaced interpolated points between the measured and simulated data were introduced using cubic splines. As a result of this step, x is now define from 0 to 145 and y from -160 to 0 with a grid resolution of 5 mm resulting in a total of 990 points. This step is done for all simulation and experimental results for both magnet systems presented further in this chapter.

As a first comparison between the numerical results and the measurements, let us focus on the torque component perpendicular to the mold T_z . According to figure 5.14, no correlation between T'_z and any pattern related to the velocity distribution of the liquid metal could be identified in either experiments or simulations. According to the numerical model, the expected torque in the z -direction using the CUB₁₅ magnet system is $T'_z < 0.2 \mu\text{Nm}$, which is lower than the resolution of the multicomponent force/torque sensor ($\pm 1.4 \mu\text{Nm}$). Additionally, an important source of deviation is that

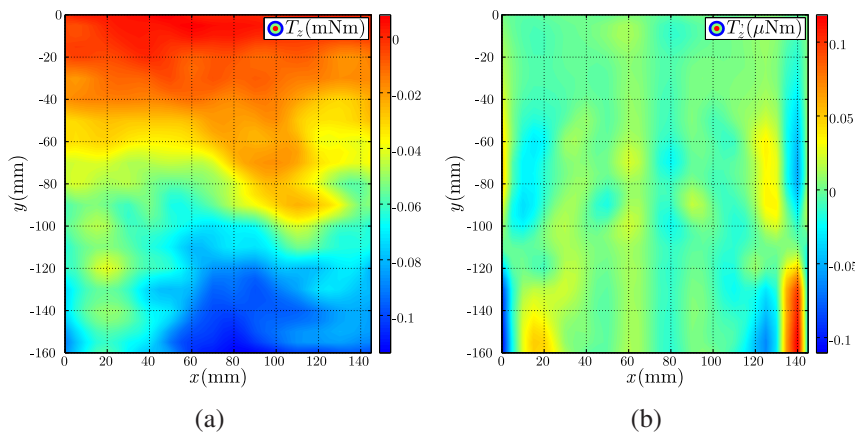


Figure 5.14: Contour plots based on T_z (a) and T'_z (b) in the $x-y$ plane. The numerical results show that $T'_z < 0.2 \mu\text{Nm}$, which means that the measured torque T_z might be noise due to positioning errors or a possible temperature drift of the sensor rather than an actual torque measurement originated by the flow.

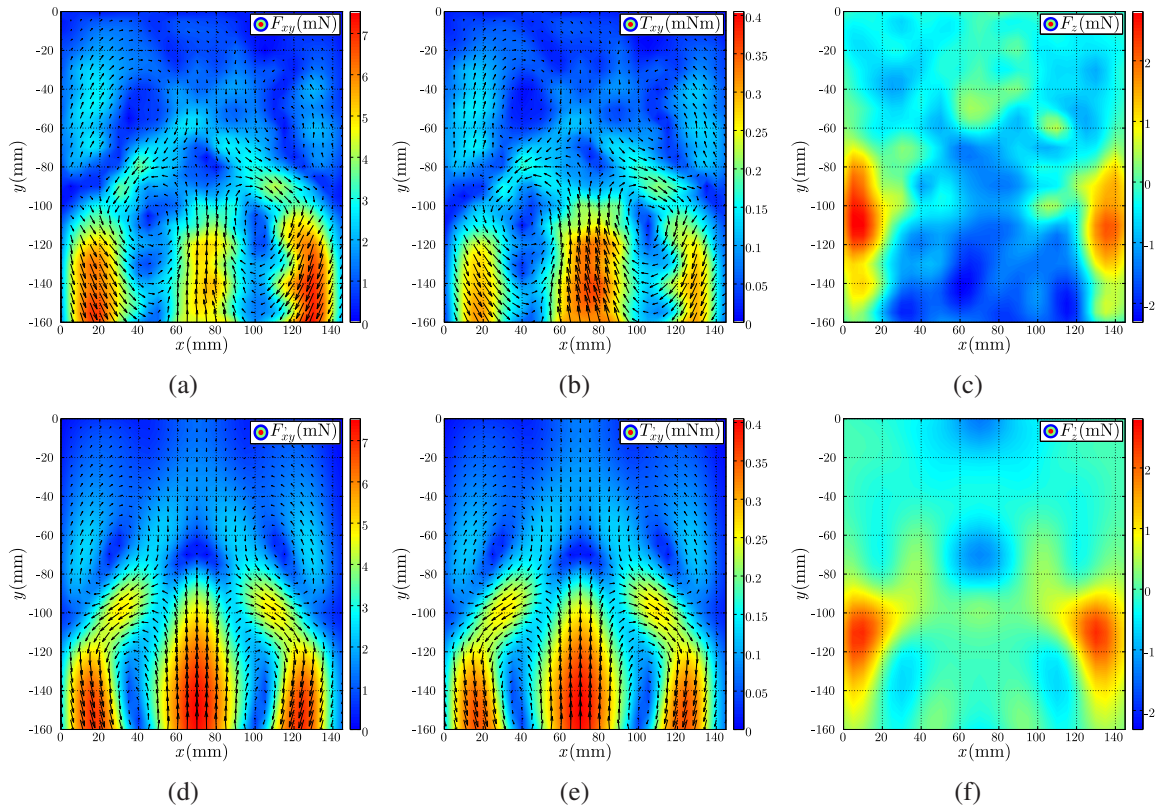


Figure 5.15: Contour and vector plots based on F_x and F_y (a) and F'_x and F'_y (d). Here, the contour plot corresponds to the magnitude and the vectors to the direction of the local force. This same approach is done for T_x and T_y (b) and T'_x and T'_y (e). Perpendicular component of the force for experiments F_z (c) and simulations F'_z (f).

the exact position of the magnet center with respect to the sensor's center was not accurately known, as there was no dry calibration *a priori* for this magnet (see section 5.3). Thus, T_z as well as T_x and T_y are calculated at the center of the sensor rather than at the center of the magnet. The numerical model has shown that T_z is too small to be measured using the current 6D-L2F2 connected to a 15 mm cubic magnet, even with a perfect alignment between the magnet and the liquid metal which is totally fulfilled in simulations.

The results regarding F_x, F_y, F_z, T_x and T_y , as well as, F'_x, F'_y, F'_z, T'_x and T'_y are shown in figure 5.15. Here, the simulated forces and torques in the $x - y$ plane show a fairly good agreement with the experiments: the magnitude of the force and torques lies in the same order of magnitude and the flow topology like the double-roll structure is clearly identified (figures 5.15(a), 5.15(d), 5.15(b) and 5.15(e)). However, we have to state some local discrepancies. For instance, the center of the vortices is shifted and the vectors differ slightly in their local direction. A possible reason of this deviation could be that the velocity field with predefined symmetries in simulations may diverge locally in comparison with the experiments. We have to keep in mind that the flow regime in

the mold is turbulent and some deviations in comparison with an ideal steady velocity case are expected. Another important source of deviation is the position of the magnet in relationship to the flow. In simulations, the magnet moves parallel and maintains a constant air gap of 1 mm between its outer surface and the surface of the mold. However, in experiments, there are always uncertainties in positioning due to the geometry of the magnet, relative flatness of the surface of the mold, the air gap and relative angle between the surface of the magnet and the mold. In experiments, the air gap between these two varied from 1 to 2 mm. In order to quantify the degree of correlation between the numerical and experimental results, the normalized 2-D cross-correlation with zero lag is used. It is defined as

$$\gamma = \frac{\sum_{x,y} (F(x,y) - \bar{F}) \cdot (F'(x,y) - \bar{F}')}{\sqrt{\sum_{x,y} (F(x,y) - \bar{F})^2 \cdot \sum_{x,y} (F'(x,y) - \bar{F}')^2}}. \quad (5.16)$$

Here, F and F' correspond to the value of the force or torque from experiments and simulations, respectively, and \bar{F} and \bar{F}' to their mean values. Now, in order to estimate the error regarding the magnitude between numerical and experimental results, let us define

$$\varepsilon = \left| \frac{\text{RMS}(F') - \text{RMS}(F)}{\text{RMS}(F')} \right|, \quad \text{RMS}(F) = \sqrt{\frac{1}{n} \sum_{i=1}^n F_i^2}, \quad (5.17, 5.18)$$

where RMS is the root mean square and n the number of points of the measurement grid. The results of (5.16) and (5.17) are summarized in table 5.3.

Table 5.3: Values of γ and ε according to (5.16) and (5.17).

	F_{xy}	F_z	T_{xy}	T_z
	mN	mN	mNm	μNm
RMS (sim)	3.05	0.62	0.16	0.02
RMS (exp)	2.70	0.98	0.14	54.03
ε	12%	57%	13%	-
γ	85%	64%	87%	-

According to table 5.3, F_z is the component that shows the lowest correlation with $\gamma < 65\%$ and the highest deviation regarding its magnitude with $\varepsilon > 50\%$. This situation can be explained using the data at the position (70,-140), where the force components $F_{xy} \approx 4.9 \text{ mN} < F'_{xy} \approx 7.35 \text{ mN}$ (figure 5.15(a)), whereas

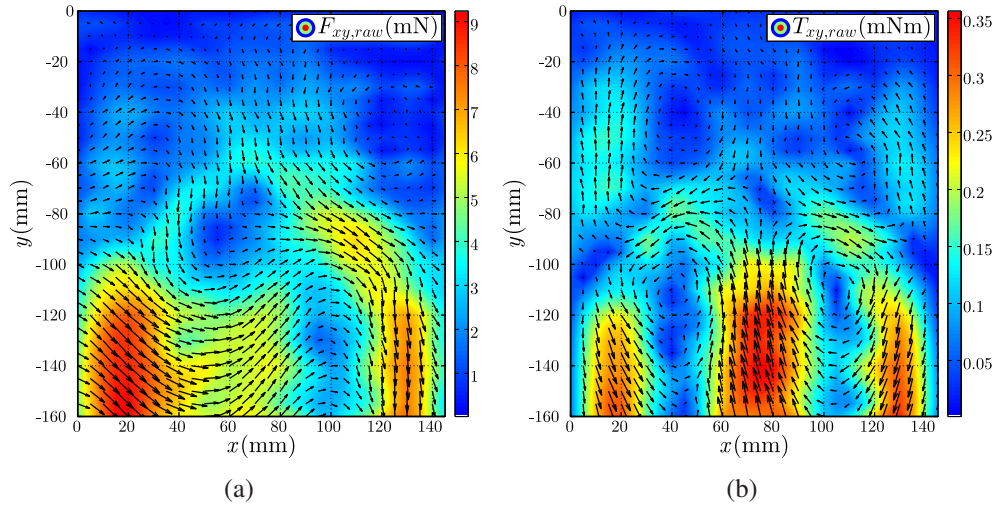


Figure 5.16: Contour and vector plots of the forces $F_{x,raw}$ and $F_{y,raw}$ (a) and torques $T_{x,raw}$ and $T_{y,raw}$ (b) acting on the magnet. They correspond to the measurements of the force and torque components in x - and y -directions without subtracting the value of the local offset.

$|F_z| \approx 1.8 \text{ mN} > |F'_z| \approx 0.13 \text{ mN}$ (figure 5.15(c)). It seems that the deviation of F_z in this area, or in general the deviation of other components like F_x near the lateral walls, can be attributed to more critical differences between the velocity distribution in simulation and experiments or to higher positioning errors. However, in the case of F'_{xy} and T'_{xy} , they both show good agreement with experiments having values of $\gamma \approx 85\%$ and $\varepsilon < 15\%$.

One of the advantages of measuring the torques acting on the magnet is that they appear to be less sensitive than the force components in the presence of ferromagnetic materials in the environment. In the case of the measurements at the mini-LIMMCAST facility, the vector plot of the force signal without taking the local offset into account (figure 5.16(a)) is disturbed probably by the influence of ferromagnetic parts like the driving motors of the positioning system. As a result, the component $F_{x,raw}$ of the force deviates considerably and we are not able to identify the four-vortex structure of the velocity field inside the mold. On the other hand, in regard to the vector plot of the torque signal, the results are very similar in comparison with the ones obtained in figure 5.15(b), where the local offset was subtracted from each measurement. The overall magnitude of the torque raw signal deviates only by about 2 % in comparison with T_{xy} and the general tendency of the vector plot remains nearly identical.

To summarize, the double-roll flow structure of the velocity was clearly identified by either the force or torque signal, the latter being less sensitive to perturbation in the environment due to ferromagnetic materials. Here, the force perpendicular to the wall offered an insight into the velocity in this direction, whereas the torque component aligned to this force was too small to be measured. Additionally,

the numerical model the experiments at the mini-LIMMCAST facility has been presented and validated. It was possible to predict the expected behavior and magnitude of all force and torque components acting on the magnet. However, some force and torque components present higher deviation in comparison with the experimental results, specially F_z and T_z , but the general tendency like the double-roll structure and the magnitude and distribution of the force and torque components in the x - and y -directions showed good agreement. By comparing the numerical and experimental results, we can conclude that the interaction parameter N is smaller than one. For its estimation according to (2.6), we use the root mean square of the velocity field in the mold $\text{RMS}(|\vec{u}|) \approx 0.18 \text{ m s}^{-1}$ and the maximum value of $B_z \approx 0.1 \text{ T}$ at a distance of 4 mm inside the liquid ($z = -11.4 \text{ mm}$). In this case, $N \approx 0.33$ for $l_c = 11.4 \text{ mm}$, $\rho = 6.33 \cdot 10^3 \text{ kg m}^{-3}$, $B = 0.1 \text{ T}$ and $u = 0.18 \text{ m s}^{-1}$.

5.6.1 Torque-to-force ratio

According to figure 5.15(a) and 5.15(b), it has been observed that the relative magnitude of the torque differs slightly locally when comparing with the relative magnitude of the force. For example at the point (130,-140), $T_{xy}/\max(T_{xy}) \approx 0.81$ and $F_{xy}/\max(F_{xy}) \approx 0.97$, as well as in simulations $T'_{xy}/\max(T'_{xy}) \approx 0.77$ and $F'_{xy}/\max(F'_{xy}) \approx 0.81$. The hypothesis for explaining this behavior is based on (2.14), where the magnitude of the torque depends on the distance between each element of the fluid and the magnet. Hence, it may provide additional information regarding the velocity of the liquid metal such as an assessment of its distribution in z -direction. Let's assume that in two points, 1 and 2, the magnitude of the force is the same $F_1 = F_2$ but the magnitude of the torque is different $T_1 < T_2$. For a qualitative analysis, let's consider two dipoles with dipole moment $m\vec{e}_z$ in front of a semi-infinite conducting layer. A sketch of the considered problem is shown in figure 5.17.

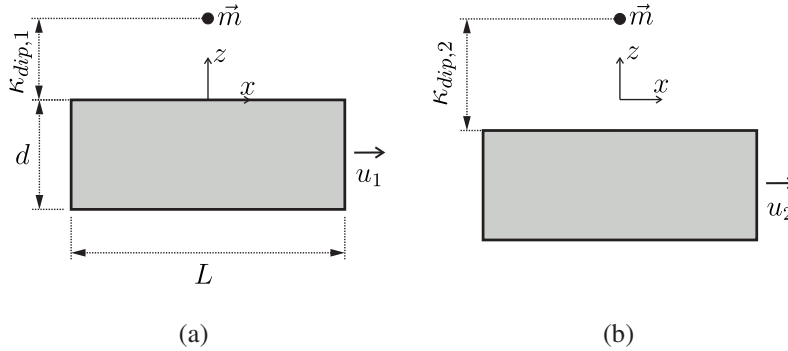


Figure 5.17: (a) Dipole at a distance $\kappa_{dip,1}$ away from a semi-infinite layer ($L \gg \kappa_{dip,1}, d \gg \kappa_{dip,1}$) with velocity u_1 . (b) Dipole at a distance $\kappa_{dip,2}$ away from a semi-infinite layer with velocity u_2 .

The first dipole is at a distance $\kappa_{dip,1}$ and the second one at a distance $\kappa_{dip,2}$ away from a moving layer with velocity u_1 and u_2 , respectively. According to (2.16), the magnitudes of the forces acting on the dipoles are

$$F_1 = \left(\frac{\mu_0^2 \sigma_l m^2}{128\pi} \right) \left(\frac{u_1}{\kappa_{dip,1}^3} \right), \quad F_2 = \left(\frac{\mu_0^2 \sigma_l m^2}{128\pi} \right) \left(\frac{u_2}{\kappa_{dip,2}^3} \right). \quad (5.19, 5.20)$$

According to (2.17), the magnitudes of the torques acting on the dipoles are

$$T_1 = \left(\frac{\mu_0^2 \sigma_l m^2}{128\pi} \right) \left(\frac{u_1}{\kappa_{dip,1}^2} \right), \quad T_2 = \left(\frac{\mu_0^2 \sigma_l m^2}{128\pi} \right) \left(\frac{u_2}{\kappa_{dip,2}^2} \right), \quad (5.21, 5.22)$$

where $T_1 = F_1 \cdot \kappa_{dip,1}$ and $T_2 = F_2 \cdot \kappa_{dip,2}$. From (5.19), (5.20), (5.21) and (5.22), it follows that when $F_1 = F_2$ and $T_1 < T_2$, then $u_1 < u_2$ and $\kappa_{dip,1} < \kappa_{dip,2}$. If we face this similar situation at the mini-LIMMCAST facility, we can therefore infer that for F_1 , the volume subset of the fluid that contributes mainly to the Lorentz force is located next to the wall. In the case of F_2 , due to relative higher velocities in the middle of the mold at some points of the measuring grid, the volume subset of the fluid that contributes mainly to the force signal is located deeper in the liquid.

Figure 5.18(a) depicts T_{xy} as a function of F_{xy} for each point of the measuring grid (including the interpolated points) and we see clearly the same effect. There are points that share the same value of F_{xy} but different values of T_{xy} . According to figure 5.18(b), the same tendency in simulations can be observed but the effect is less pronounced. For a deeper analysis of the results, the points are separated by a black line that corresponds to a linear regression through the origin. Then, we calculate the value k and k' which is the vertical distance between each point from T_{xy} vs. F_{xy} and T'_{xy} vs. F'_{xy} and the corresponding black fitting line: if the point is located on top of the line $k > 0$ and $k' > 0$ and vice versa. The results for k and k' are summarized in figure 5.18(c) and 5.18(d) for experiments and simulations, respectively. Let us focus first on the area below $y \approx -100$ mm of the mold. Here, we can see that most of the points where $k < 0$ are located near the lateral walls, whereas the points where $k > 0$ are located at $x \approx 50 \dots 100$ mm. Regarding k' , it shows the same behavior in that region of the mold, but above $y \approx -100$ mm, the deviation of k' in comparison with k is higher. This deviation might be due to the electrical conductivity of the SEN. According to chapter 3, the Lorentz force is stronger when the electrical conductivity of the wall increases and this might have an influence on k' .

Now, let us focus on 3 characteristic points (70,-135), (125,-100) and (125,-150) on figures 5.18(c) and 5.18(d), and then calculate the ratio T_{xy}/F_{xy} and T'_{xy}/F'_{xy} . The results are summarized in table 5.4. Here, it is shown that the ratio T'_{xy}/F'_{xy} is not constant: its maximum value is at (125,-100) and its lowest at (125,-150). If the earlier

5. Multicomponent local Lorentz force velocimetry

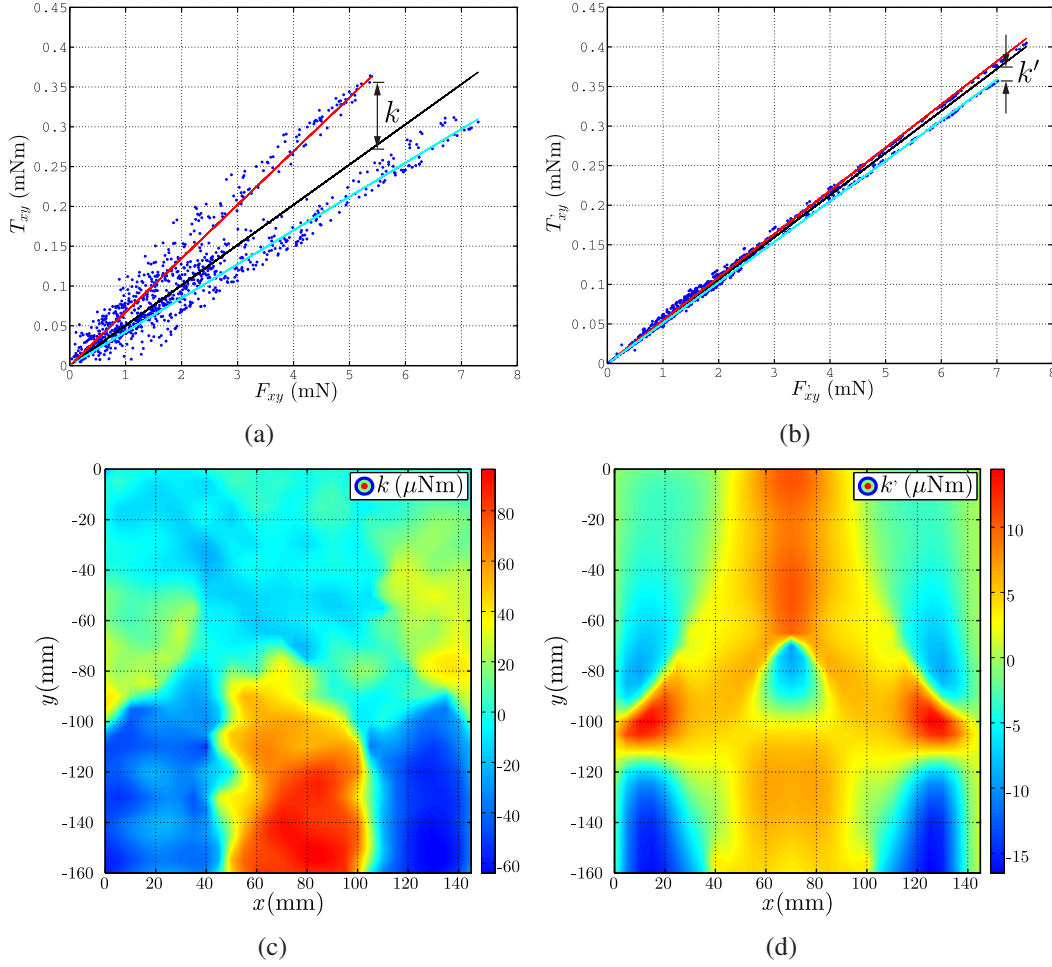


Figure 5.18: T_{xy} as a function of F_{xy} from experiments (a) and T'_{xy} as a function of F'_{xy} from simulations (b). The black lines corresponds to a linear regression through the origin, where $T_{xy} = 0.0505F_{xy}$ and $T'_{xy} = 0.0532F'_{xy}$. In both experiments and simulations $T_{xy} \sim F_{xy}$, although they appear to tend two different slopes m which are more pronounced in experiments ($m_{red} = 0.0673$ m, $m_{cyan} = 0.0425$ m) than in simulations ($m_{red} = 0.0546$ m, $m_{cyan} = 0.0512$ m). Distribution of k (c) and k' (d) in the $x - y$ plane. k and k' represent the vertical distance between each blue point from (a) and (b) and the corresponding black fitting line.

Table 5.4: T_{xy}/F_{xy} in comparison with T'_{xy}/F'_{xy} at three different points across the wide face of the mold.

Point	(70,-135)	(125,-100)	(125,-150)
T_{xy}/F_{xy} (mm)	68.74	40.33	40.76
T'_{xy}/F'_{xy} (mm)	54.03	59.05	50.92

predictions are correct, the maximum of the velocity field that contributes mainly to the Lorentz force should be near the wall at (125,-150), whereas at (125,-100) should be located deeper inside the liquid. By comparing the magnitude of the velocity field u_{xy} at these points along the z -direction (figure 5.19), we clearly see that this is indeed the case.

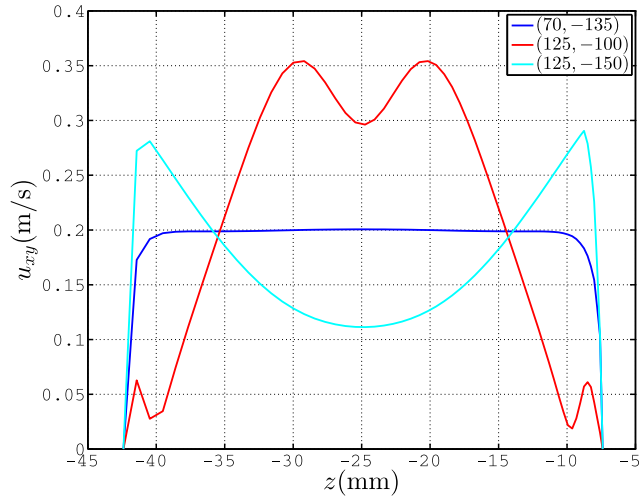


Figure 5.19: u_{xy} as a function of z at different points across the wide face of the mold according to table 5.4.

5.6.2 Calibration factor

In this section, an assessment of the magnitude of the velocity field $u_x \vec{e}_x$ in experiments is going to be performed based on the dry calibration concept from section 5.3.4. The CUB₁₅ is located at a distance of $\kappa = 7.4$ mm away from the surface of the disk, which corresponds to the distance between the surface of the magnet and the liquid metal in the experiments at the mini LIMMCAST facility (figure 5.11). In this case, the calibration factor $K_{disk} = 2.7$ is obtained numerically using a disk with 200 mm in diameter (figure 5.6). Due to the comparably bigger distance and volume of the magnet system in comparison with the one used in section 5.3, a bigger diameter of the disk has to be considered to avoid edge effects.

Finally, the calibration factor at the mini-LIMMCAST facility according to (5.15) is $K_{liq} = K_{disk}(\sigma_{disk}/\sigma_l) \approx 2.7(25.4/3.3) = 20.8$ m/(sN). For validation, 10 UDV probes with a vertical distance of 10 mm were mounted at the narrow face and their center was 4 mm away from the wide face of the mold (similar to [61]). In this configuration, the velocity close to the wall of the wide face could be recorded. Owing to the rapid decay of magnetic fields, this might be the place of the highest contribution of the measured Lorentz force. A comparison between the velocity field u_x measured by UDV in comparison with the velocity field $u'_x = K_{liq} \cdot F_x$ according to (5.14) is shown in figure 5.20 having good agreement ($\text{RMS}(u_x) = 27.6$ mm/s \approx $\text{RMS}(u'_x) = 27.2$ mm/s).

With the proposed dry calibration procedure, we could obtain a conservative assessment of the magnitude of the velocity field at a depth of 4 mm at mini-LIMMCAST facility. It can be assumed, in general, that this method can be used for a simple and fast approximation for K_{liq} regarding cubic or cross-shaped magnet systems. However,

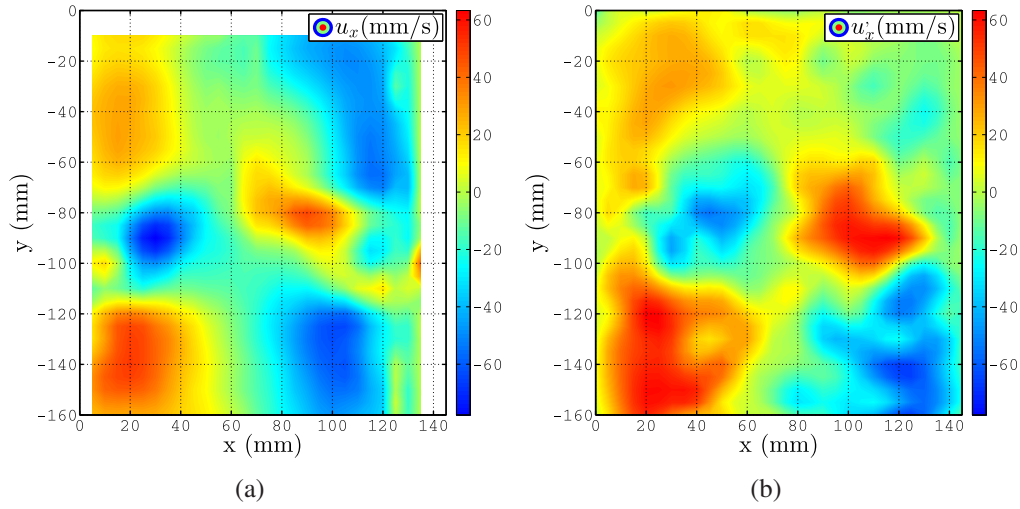


Figure 5.20: Comparison between UDV measurements of u_x near the wall (a) and the velocity component u'_x (b) according to (5.14) using the measured force component acting on the magnet F_x [44].

this approximation of K_{liq} has the intrinsic uncertainty related to the type of velocity distribution of the liquid next to the wall spanned by the magnetic field. As it has been discussed in section 5.6.1, different velocity distributions can generate the same values of the Lorentz force exhibiting different volumes of integration. This topic will be further discussed in section 5.8, where the spatial resolution of the experiments will be numerically investigated.

5.7 Results using the CSM_{31.17}

After the calibration procedure described in section 5.3.5, the second measurement campaign at the mini-LIMMCAST facility was performed using the 6D-L2F2 attached to the CSM_{31.17}. The CSM_{31.17} was placed in front of the acrylic glass mold leaving an air gap of about 1 mm and scanned the wide face in the same zig-zag movement as the CUB₁₅ for comparison (figure 5.12(b)). The results of the measured ($F_x, F_y, F_z, T_x, T_y, T_z$) and simulated ($F'_x, F'_y, F'_z, T'_x, T'_y, T'_z$) force and torque components across the wide face of the mold are summarized in figures 5.21 and 5.22 as vector and contour plots. The torques in the present section are now calculated at the center of the CSM_{31.17} ($z = 7.5$ mm), in contrast with the results using the CUB₁₅ (section 5.6) in which the torques were calculated at the center of the multicomponent force/torque sensor ($z = 48.5$ mm).

According to figures 5.21(a), 5.21(d), 5.21(b) and 5.21(e), the orientation of the vector plots is slightly different in comparison with the results using the CUB₁₅. This difference is due to the fact that the volume of the CSM_{31.17} is 5 times larger than the CUB₁₅. This means that the portion of the flow volume that interacts with

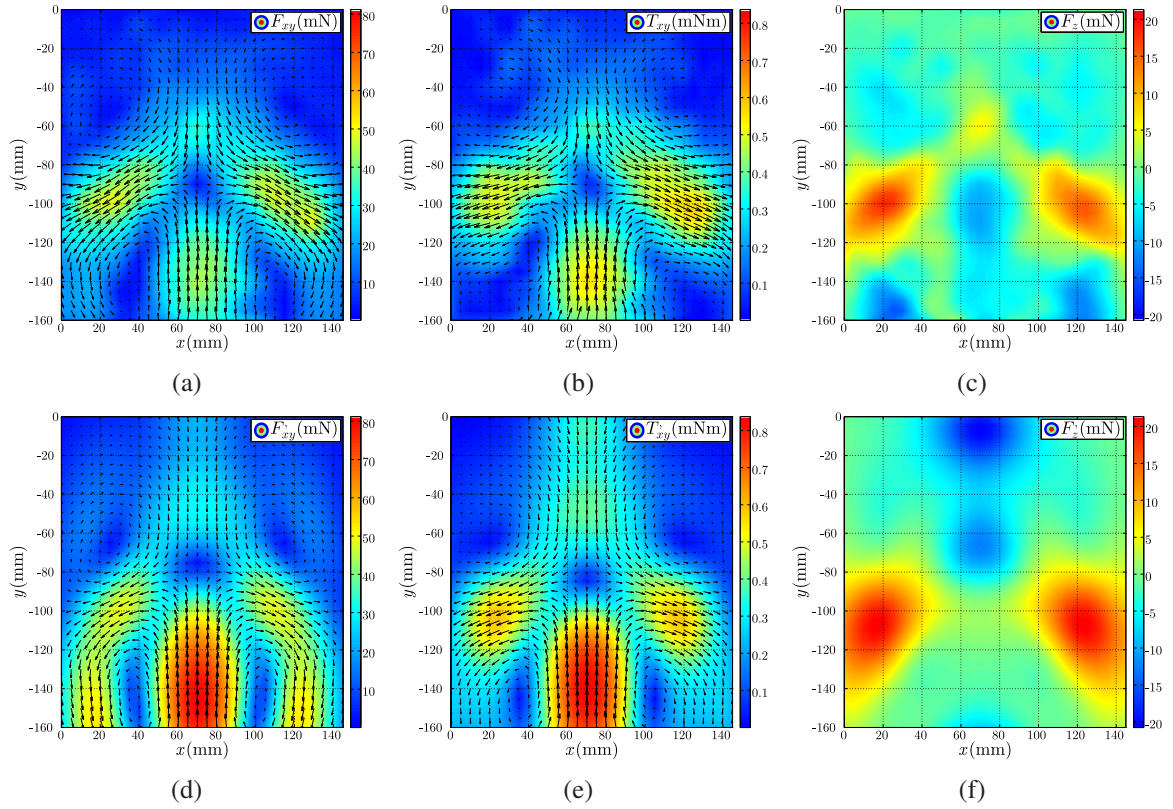


Figure 5.21: Contour and vector plots acting based on F_x and F_y (a) and F'_x and F'_y (d). Here, the contour plot corresponds to the magnitude and the vectors to the direction of the local force. This same approach is done for T_x and T_y (b) and T'_x and T'_y (e). Perpendicular component of the force F_z (c) and F'_z (f).

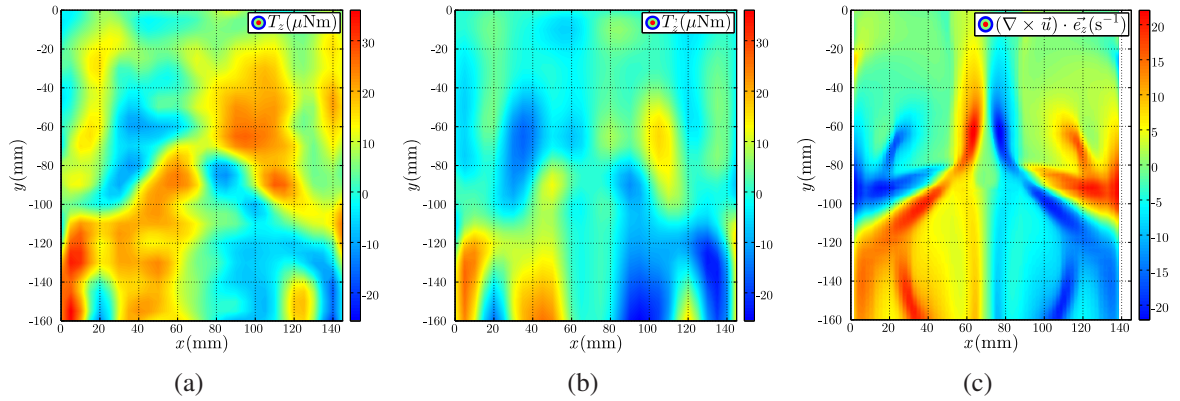


Figure 5.22: Distribution of T_z (a) and T'_z (b). Distribution of the vorticity of the velocity field perpendicular to the wide face of the mold $(\nabla \times \vec{u}) \cdot \vec{e}_z$ at $z \approx -13.8$ mm (c). According to (a), (b) and (c), a correlation between T_z or T'_z and $(\nabla \times \vec{u}) \cdot \vec{e}_z$ can be observed.

the magnetic field is larger, and therefore, the spatial resolution of a local velocity assessment decreases. Nevertheless, the vector plots regarding F_x, F_y and T_x, T_y , in comparison with F'_x, F'_y and T'_x, T'_y show the expected double-roll structure of the velocity field. However, we observe a higher deviation when comparing the magnitude of these components as now the interaction parameter seems to be of order 1. For

example, in the case of F_{xy} and F'_{xy} , we see that $\max(F_{xy}) \approx 48.8 \text{ mN}$ is about 40% weaker than $\max(F'_{xy}) \approx 81.2 \text{ mN}$. This effect was also observed regarding T_{xy} and T'_{xy} , where $\max(T_{xy}) = 0.57 \text{ mNm}$ and $\max(T'_{xy}) = 0.84 \text{ mNm}$. For the estimation of N according to (2.6), we used the same u , l_c and ρ as the CUB₁₅, but now $B_z \approx 0.2 \text{ T}$ for the CSM_{31.17}. In this case, $N \approx 1.32$. For F_{xy} and T_{xy} , the values of γ are in general lower than the ones obtained using the CUB₁₅ and in the case of ε , the values are greater. This situation is shown in table 5.5 analogous to table 5.3 for comparison.

Table 5.5: Values of γ and ε according to (5.16) and (5.17), respectively.

	F_{xy}	F_z	T_{xy}	T_z
	mN	mN	mNm	μNm
RMS (sim)	31.34	7.41	0.33	8.28
RMS (exp)	21.84	5.38	0.25	12.24
ε	30%	27%	23%	48%
γ	70%	57%	80%	78%

However, in the case of F_z, T_z and F'_z, T'_z it has been observed a relative good agreement in both magnitude and overall distribution despite the finite value of N . In the case of T_z (figure 5.22(a)) and T'_z (figure 5.22(b)) the same patterns were identified specially in the regions at the top and bottom of the measuring grid, where the vortex structure of the force or torque distribution appears. In the points of positive force vorticity, T_z is positive and vice versa. In can therefore be inferred that this torque could give us information regarding $(\nabla \times \vec{u}) \cdot \vec{e}_z$, which is true for a magnet in front of a rotating disk made of aluminum as shown in section 5.3. Now let's plot $(\nabla \times \vec{u}) \cdot \vec{e}_z$ at $z \approx -13.8 \text{ mm}$, i.e. 6.4 mm away from the wall (figure 5.22(c)). This similar pattern of vorticity appears up to a distance of about 8 mm inside the liquid metal ($z \approx -15.4 \text{ mm}$) and at $z \approx -13.8 \text{ mm}$ it reaches the maximum value of $\gamma \approx 47\%$ when comparing with T'_z . When these two quantities $(\nabla \times \vec{u}) \cdot \vec{e}_z$ and T'_z are locally compared at each point of the measuring grid, we can find higher deviations owing to the fact that the value of the torque, as well as the force, is a volume integration rather than a value on a point. However, a general tendency and a clear correlation between $(\nabla \times \vec{u}) \cdot \vec{e}_z$ and T_z can be identified: in the regions of positive or negative vorticity, we have also positive and negative values of T_z . We can therefore conclude that, by measuring the torque T_z , we could infer information on the vorticity of the velocity field of the liquid metal in this direction.

5.7.1 Torque-to-force ratio

Figures 5.23(a) and 5.23(b) show T_{xy} as a function of F_{xy} and T'_{xy} as a function of F'_{xy} , respectively. In the case of k and k' , the results are presented in figure 5.23(c) and 5.23(d). According to figures 5.23(a) and 5.23(b) the distributions of T_{xy} vs F_{xy} as well as T'_{xy} vs F'_{xy} are rather disperse and no clear characteristic slopes could be identified in both experiments and simulations as the ones obtained using the CUB₁₅. The values of k and k' in this case show different patterns, in which k might have been influenced by finite N effects. Additionally, it appears that the CSM_{31.17} is too big in comparison with the cross-section or the general structure of the velocity field in the mold.

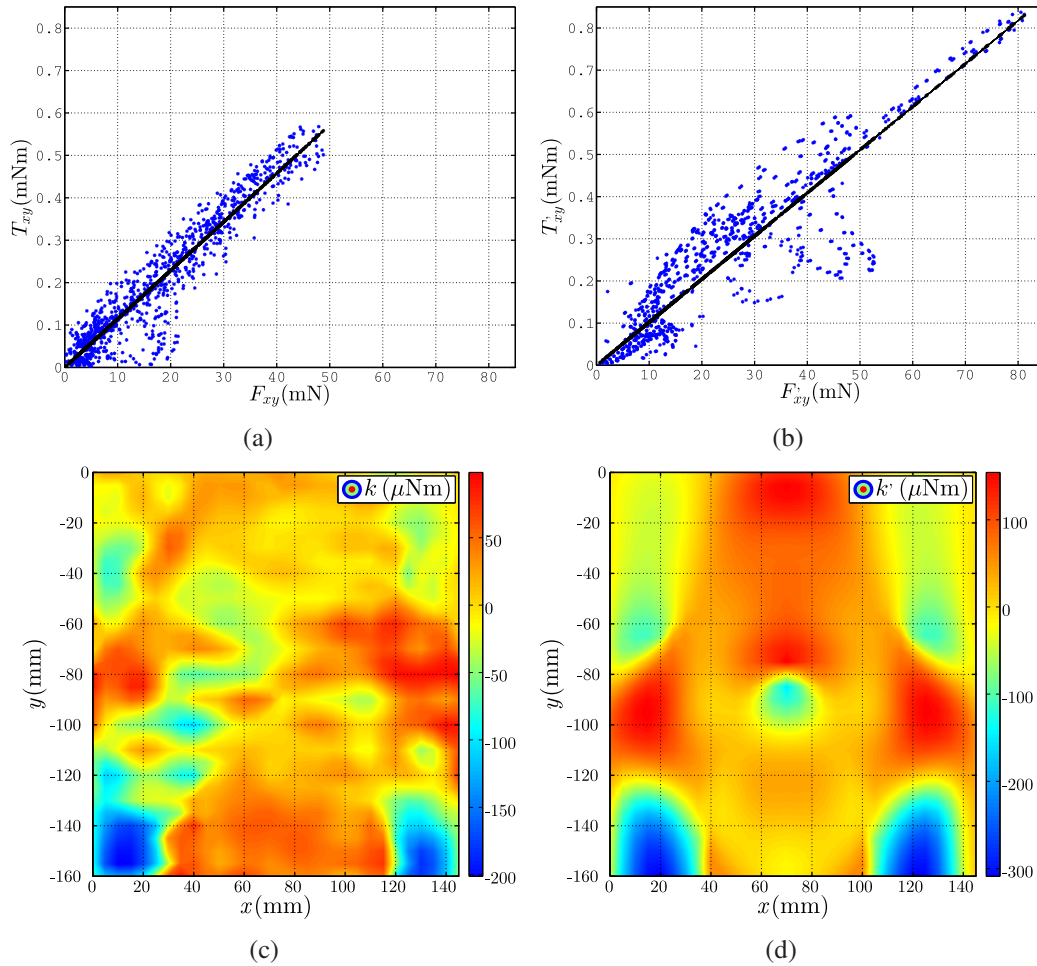


Figure 5.23: T_{xy} as a function of F_{xy} from experiments (a) and T'_{xy} as a function of F'_{xy} from simulations (b). The black lines corresponds to a linear regression through the origin, where $T_{xy} = 0.0114F_{xy}$ and $T'_{xy} = 0.0102F'_{xy}$. Distribution of k (c) and k' (d) in the $x-y$ plane. k and k' represent the vertical distance between each blue point from (a) and (b) and the corresponding black fitting line.

5.8 Spatial resolution

The goal of the present section is to determine the fraction of the fluid that contributes mainly to the Lorentz force acting on the magnet. According to equation (2.13), local Lorentz force velocimetry is intrinsic associated with a volume of integration depending on the portion of the flow spanned by the magnetic field. One of the biggest difficulties of this task is that this volume cannot be uniquely defined, as it also depends on the velocity distribution of the flow despite the rapid decay of the magnetic field. As it has been shown in figure 5.18 from section 5.6.1, we can have points across the measuring grid at the mini-LIMMCAST facility that share the same force but different velocities distributions in the depth-wise direction inside the mold. Thus, the portion of the fluid volume that contributes to the measured force may vary within them. This volume uncertainty could be decreased by developing new magnet systems that generate strongly localized magnetic fields in a rather smaller volume, like the one developed by Weise in [71]. However, this might led to much higher values of the interaction parameter N or very weak Lorentz forces due to the reduced volume of integration. Another alternative is to place the magnet system as close as possible next to the liquid metal. In this section, this minimum optimal distance between the magnet system and the liquid metal is going to be analyzed for cubic and cross-shaped magnet systems. For the analysis, the following magnets systems are taking into consideration: cubic permanent magnets with side edge 5 mm, 10 mm and 15 mm (CUB₅, CUB₁₀ and CUB₁₅^{*}) and the cross-shaped magnet CSM_{31.17}. All magnet systems share the same magnetization ($M_z = 1.138 \text{ MA/m}$) in order to focus only on the influence of their size on the solution. Their center in the x - and y -directions is placed at the same points of the measuring grid previously defined in section 5.4.1 maintaining an air gap of 1 mm. In this section, the name of the 15 mm cubic magnet has an asterisk in order to differentiate it from the one used in section 5.6, which has a weaker magnetization.

The developed numerical model from section 5.5 will be used for the analysis of the penetration depth and the spatial resolution of the measurements at the mini-LIMMCAST facility. As shown previously in section 5.2, isosurfaces defined by the magnitude of the magnetic field $B_{iso} = \sqrt{B_x^2 + B_y^2 + B_z^2}$ allow us to uniquely define a portion of the flow volume spanned by the magnetic field. This volume can be approximated by an spherical cap of height $h_{cap} = z_{max} - z_{min}$, i.e. penetration depth, and radius of the base of the cap $a_{z=z_{min}}$, i.e. spatial resolution (figure 5.24). As shown in figure 5.11(a), $z_{min} = 7.4 \text{ mm}$ is the distance between the surface of the magnet systems and the liquid metal at the mini-LIMMCAST facility. The analysis will focus on finding the portion of the fluid that contributes mainly to the magnitude of the forces

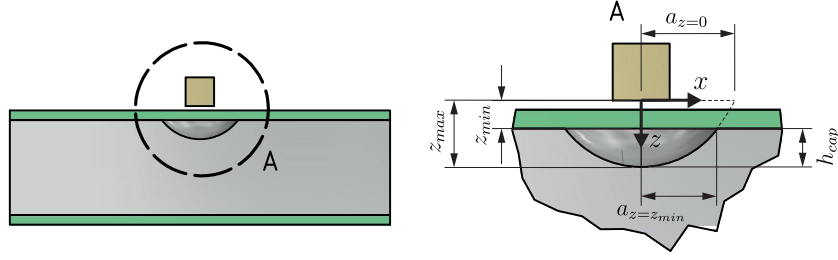


Figure 5.24: Sketch of the spherical cap in the liquid that generates the force $F'_{xy}|_{B_{iso}} \approx F'_{xy}$.

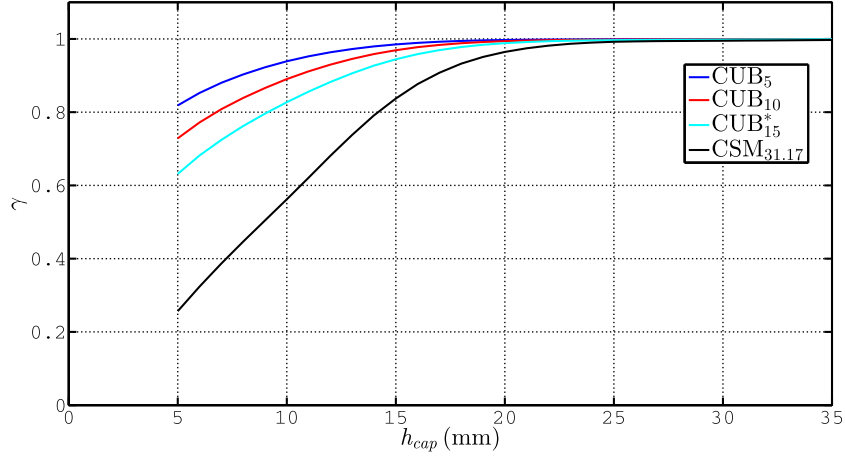


Figure 5.25: 2D normalized cross-correlation γ between $F'_{xy}|_{B_{iso}}$ and F'_{xy} as a function of h_{cap} for each magnet system considered in this section.

orthogonal to the magnetization of the magnets, i.e. $F'_{xy}|_{B_{iso}} \approx F'_{xy}$. The area of interest of the mold will be below $y = -80$ mm from the measuring grid in order to avoid the influence of the SEN on the solution.

Now, the 2D normalized cross-correlation γ is calculated between F'_{xy} and $F'_{xy}|_{B_{iso}}$ according to equation (5.16). The information of γ is used to identify a minimum value of h_{cap} , in which $F'_{xy}|_{B_{iso}}$ sufficiently correlates with F'_{xy} in average by taking into account all points of the measuring grid below $y = -80$ mm. The value of B_{iso} as well as h_{cap} of each magnet system are obtained for $\gamma \approx 99\%$ as shown in figure 5.25. The parameters of the spherical caps are shown in table 5.6, and a comparison between F'_{xy} and $F'_{xy}|_{B_{iso}}$ is depicted in figures 5.26 and 5.27. The values of $a_{z=0\text{mm}}$ are obtained using equations $a_{z=0\text{mm}}/l_{mag} \approx 0.00062(z_{max}/l_{mag})^2 + 0.79z_{max}/l_{mag} + 0.38$ for the $CUB_{l_{mag}}$ and $a_{z=0\text{mm}}/l_{mag} \approx 0.023(z_{max}/l_{mag})^2 + 0.61z_{max}/l_{mag} + 0.62$ for the $CSM_{l_{mag}}$ (see section 5.2). Then, we can obtain R as follows $R = (a_{z=0\text{mm}}^2 + z_{max}^2)/(2z_{max})$. Once R is known, the spatial resolution in the liquid is given by $a_{z=7.4\text{mm}} = \sqrt{2h_{cap}R - h_{cap}^2}$.

According to table 5.6, the volume of integration is larger when the characteristic length of the magnet l_{mag} increases, as expected. Thus, we can have an insight into the velocity distribution of the liquid metal at different depths inside the mold depending on the size of the magnet. Let us focus on the center and on the lateral walls of the

5. Multicomponent local Lorentz force velocimetry

Table 5.6: Penetration depth and spatial resolution of different magnet systems.

Magnet	l_{mag}	B_{iso}	z_{min}/l_{mag}	z_{max}/l_{mag}	h_{cap}	$a_{z=0mm}$	R	$a_{z=7.4mm}$	$\max(F'_{xy})$
	mm	mT			mm	mm	mm	mm	mN
CUB ₅	5	1.6	1.48	4.72	16.2	20.6	20.8	20.3	0.1
CUB ₁₀	10	8.1	0.74	2.59	18.5	24.3	24.3	23.6	1.4
CUB ₁₅ *	15	17.9	0.49	1.86	20.5	27.7	27.7	26.8	8.4
CSM _{31.17}	31.17	47.2	0.24	1.01	24.0	39.2	40.2	36.8	81.4

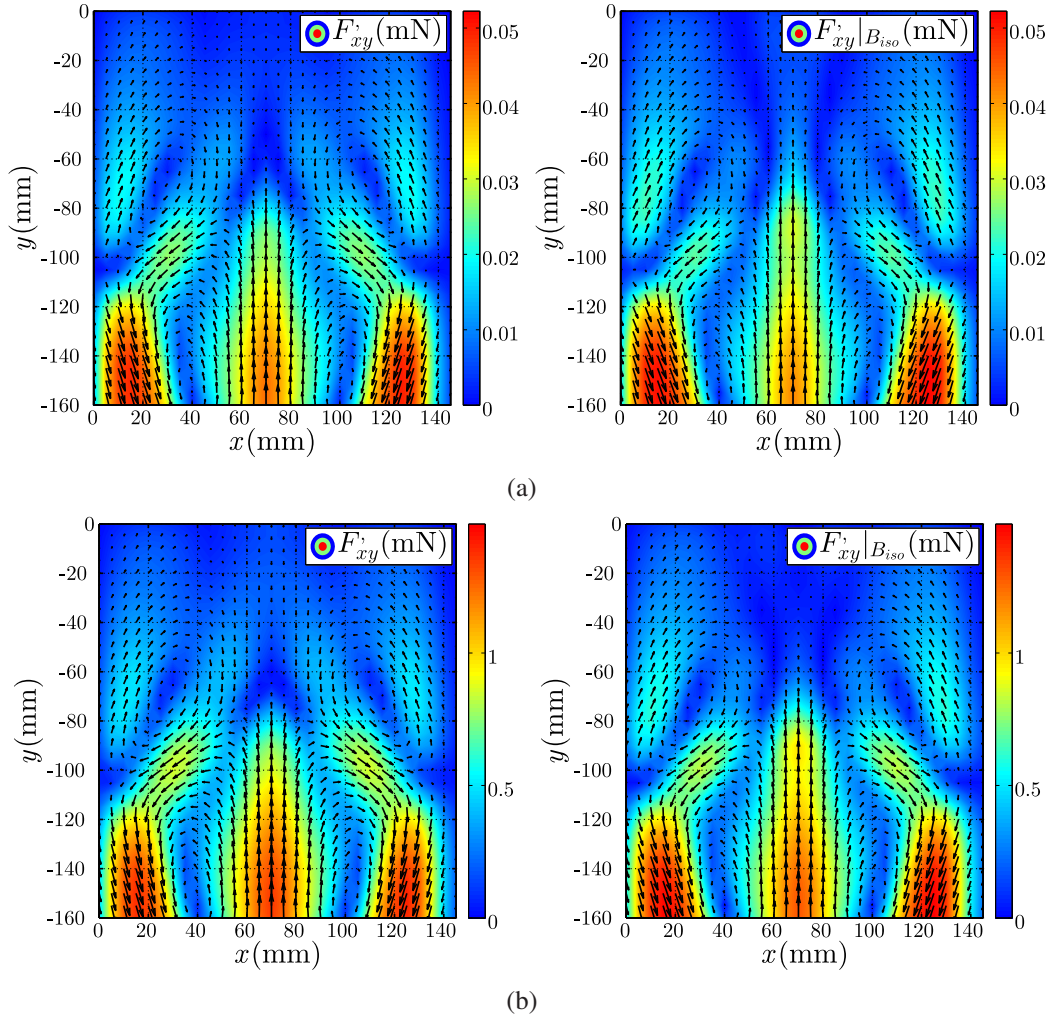


Figure 5.26: Comparison between the Lorentz force contour and vector plots based on F'_{xy} and $F'_{xy}|_{B_{iso}}$ for the CUB₅ (a) and CUB₁₀ (b) magnet systems according to the parameters from table 5.6.

measuring grid below $y = -80$ mm. As we have seen in section 5.6.1, at (125,-150) the maximum value of u_{xy} in the liquid is located near the wall, whereas at (70,-135) the maximum is located deeper inside the liquid. As a consequence, the CUB₅ is able to see a portion of the fluid closer to the wall and therefore the maximum value of F'_{xy}

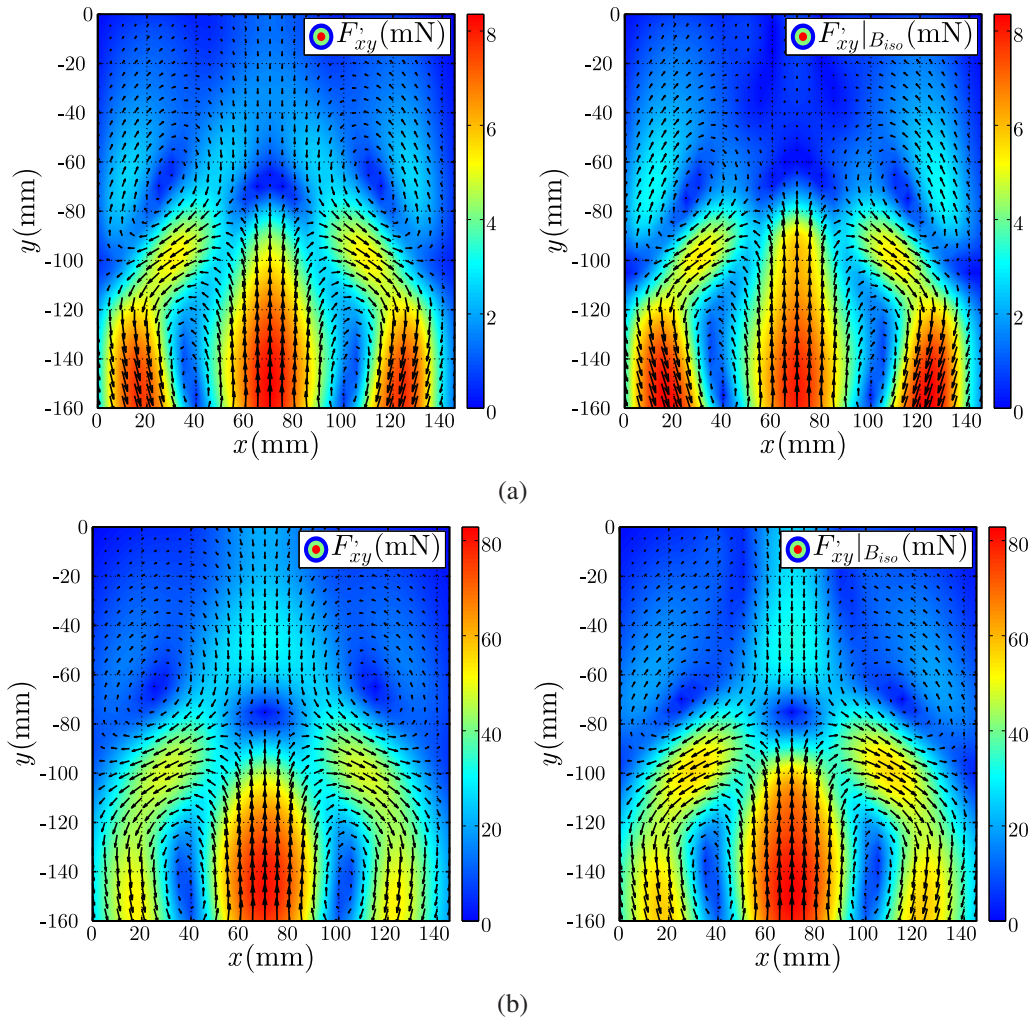


Figure 5.27: Comparison between the Lorentz force contour and vector plots based on F'_{xy} and $F'_{xy}|_{B_{iso}}$ for the CUB_{15}^* (a) and $CSM_{31.17}$ (b) magnet systems according to the parameters from table 5.6.

is in this case located near the lateral walls (see figure 5.26(a)). When l_{mag} is larger, the maximum value of F'_{xy} is no longer located at the lateral walls but in the middle of the mold (see figure 5.27). The volume of integration is sufficiently big to identify the velocity field distribution deeper inside the mold.

However, the volume of integration in the fluid given by h_{cap} and $a_{z=7.4mm}$ seems to scale linearly with the characteristic length l_{mag} , in contrast to the scaling of the maximum value of the force in this area of the mold for the CUB magnet systems ($\max(F'_{xy}) \sim (l_{mag})^{4.6}$). Thus, it is not always advantageous to decrease the size of the magnet for improving the spatial resolution, as the magnitude of the force decays considerably faster increasing the complexity of its measurement. Another important issue to consider is that the surface of the magnets are all at a distance of $z = 7.4$ mm away from the liquid, which is larger than the l_{mag} of the CUB_5 and slightly smaller than the one of the CUB_{10} . Hence, the liquid metal will not be subjected to stronger magnetic

field gradients for $z > l_{mag}$, and therefore, the volume of integration is noticeably larger than expected for the CUB₅ or for the CUB₁₀. We can see for example that between CUB₁₀ and CUB₁₅^{*} the penetration depth h_{cap} and spatial resolution $a_{z=7.4mm}$ decrease by about 10% and 12%, respectively, whereas F'_{xy} is about 83% weaker. In conclusion, the optimal distance between the surface of the magnet and the liquid metal z_{min} depends on the characteristic length l_{mag} of the permanent magnet. This distance should be at least lower than l_{mag} . In this sense, we could reduce the uncertainty of the portion of the fluid that contributes mostly to the measured Lorentz force, which can be approximated by a spherical cap as shown in section 5.2.

5.9 Conclusions

In this chapter, multicomponent local Lorentz force velocimetry was used to infer the flow characteristics of steady turbulent liquid metal flows. In particular, multicomponent LFV was capable of providing a three-dimensional velocity assessment of GaInSn in eutectic composition in the region adjacent to the wall of a model of a continuous caster. The double-roll flow structure, typical of the continuous casting of steel, was clearly identified by either the force or torque signal, the latter being less sensitive to perturbation in the environment due to the presence of ferromagnetic materials. Moreover, the force perpendicular to the wall showed the areas where the liquid metal jet reaches the side walls, strongly diffuses and deviates in an upper and lower vortex giving an insight into the velocity in this direction.

With the numerical model of the experiments using kinematic LFV, it was possible to predict the expected behavior and magnitude of all force and torque components acting on two given magnet systems: a 15 mm cubic permanent magnet (CUB₁₅) and a cross-shaped magnet (CSM_{31.17}). However, some force and torque components presented higher deviations in comparison with the experimental results, but the general behavior like the double-roll structure and the magnitude and distribution of the force and torque components in the x and y -directions were in good agreement. In the case of the CUB₁₅ magnet system, it was observed that the ratio T'_{xy}/F'_{xy} can also be used to obtain information on the velocity field distribution of u_{xy} in the depth-wise direction by comparison with other points across the wide face of the mold. The numerical model confirmed that T'_z is too small to be measured under the experimental conditions at the mini-LIMMCAST facility using a 15 mm cubic magnet.

In the case of the numerical results regarding the CSM_{31.17}, where the back reaction of the induced Lorentz forces in the liquid is also neglected, we obtained a higher deviation in comparison with the experimental results as the interaction parameter N

is in this case finite ($N \approx 1.32$). The torque and force components in the x - and y -directions were the most affected, in contrast with the torque and force components perpendicular to the surface of the mold T_z and F_z . These last two components showed a general good agreement like a similar overall magnitude and patterns across the wide face of the mold. By comparing T_z' with the vorticity of the velocity field in this direction, a correlation between these two quantities was observed. By measuring T_z , we can therefore obtain a rough estimate of the curl of the local velocity field in this direction, in addition to a local assessment of the velocity field based on the other force and torque components. In this chapter, it has been shown that T_z is indeed measurable in liquid metals with the multicomponent force/torque sensor attached to a cross-shaped magnet. The cross-shaped magnet provides a pronounced non-axisymmetric magnetic field distribution in the liquid metal, which is needed for obtaining measurable values of T_z . However, there is still abundant room for further optimization of the magnet system in order to increase further the magnitude of T_z while maintaining lower values of N .

Last but not least, this chapter also investigated the concept of dry calibration of the 6D-L2F2 using a rotating disk made of aluminum. With this set-up, the location of the magnet system center with respect to the sensor's coordinate system can be accurately determined. This step is mandatory for correct torque measurements. Additionally, this dry calibration procedure can help to conservatively estimate the value of the calibration factor that relates the measured Lorentz force and the local velocity of the liquid metal.

Chapter 6

Summary and Outlook

In this work, it was shown that the force component generated by the induced electric potential was sensitive to the ratio between the electrical conductivity of the wall and the liquid. This ratio defines the limits in which perfectly-conducting and perfectly-insulating walls appeared. In the first case, the force originating from the electric potential was zero and in the second case it reached its maximum value. The results obtained when varying the aspect ratio of the flow cross-section have shown that, this force depends on the proximity of the top and bottom walls to the applied magnetic field. In general, the force component generated by the induced electrical potential was always opposite to the one given by the cross product between the velocity of the liquid and the applied magnetic field. Hence, when this force component was diminished by either increasing the electrical conductivity of the walls or by changing the aspect ratio of the flow cross-section, the measurable total Lorentz force increased significantly, and therefore, the sensitivity of the measurements can be improved. With Lorentz force velocimetry applied to electrolytes, an effectively infinite wall conductivity can be reached using common materials like copper.

In the case of local LFV, multicomponent local Lorentz force velocimetry was numerically and experimentally investigated. This method has proven to be a useful contactless tool to obtain information on the local velocity field related to three-dimensional turbulent steady flows in the region adjacent to the wall next to the magnet. In particular, multicomponent local Lorentz force velocimetry was used to infer the flow characteristics of GaInSn inside a mold of a continuous caster model. In this case, the three-dimensional velocity assessment is given by the value of the three force components across the wide face of the mold. The double-roll flow structure, typical of the continuous casting of steel, was clearly identified as well as the velocity field perpendicular to the wall. The torque components orthogonal to the magnetization of the magnet systems showed the same double-roll structure like the force. Interestingly,

when comparing the ratio of this two-component torque to the magnitude of the two-component force, information on the velocity distribution in the depth-wise direction could be inferred. Additionally, by comparing the torque component with the vorticity of the velocity field both pointing in the same direction as the magnetization of the magnet, a correlation between these two quantities was observed. Therefore, we can obtain a rough estimate of the curl of the local velocity field in this direction, in addition to a local assessment of the velocity field based on the other measured force and torque components. It has also been shown that, a non-axisymmetric magnetic field distribution in the liquid metal is needed for measuring this torque component, which can be generated by a cross-shaped magnet system.

Despite the fact that the torque component perpendicular to the mold was indeed measurable in GaInSn using the proposed cross-shaped magnet, the finite value of the interaction parameter N is a factor to be considered in future applications. Nevertheless, there is still abundant opportunity for further optimization of the magnet system in order to continue increasing the magnitude of this torque component while maintaining lower values of N . To decrease the gap between local velocity assessment via force and torque measurements, calibration procedures can be numerically and experimentally developed, which can be based on characteristic velocity distributions, e.g., 1D, 2D, and 3D laminar and turbulent profiles, and on distance variations between the magnet system and the liquid metal.

In multicomponent local Lorentz force velocimetry, it is crucial to know the position of the center of the magnet system with respect to the sensor's coordinate system for accurate torque measurements. For this purpose, a dry calibration procedure was developed that solves this issue. With the proposed dry calibration procedure of the multicomponent force and torque sensor using a rotating electrically-conducting disk, the location of the magnet system center with respect to the sensor's coordinate system can be accurately determined. Additionally, this dry calibration procedure can help to conservatively estimate the value of the calibration factor that relates the measured Lorentz force and the local velocity of the liquid metal.

The term "local" in local Lorentz force velocimetry is intrinsically associated with a volume of integration, no matter how small the permanent magnet is. Based on the numerical models of the experiments, the portion of the flow spanned by the magnetic field was estimated in terms of the characteristic length l_{mag} of the magnet system, which is defined as the point along the magnetization of the magnet in which the magnitude of the magnetic field decreases to about 10.4%. Decreasing the size of the magnet does not necessarily offer a significant advantage in improving the spatial resolution, as the distance between the magnet and the liquid metal needs to be consid-

ered as well. In general, the distance between the magnet system and the liquid metal should be less than l_{mag} , where the magnitude and gradient strength of the magnetic field are more strongly pronounced than elsewhere. Hence, a more accurate estimate of the integration volume is possible using the applied magnetic field. Moreover, a pronounced non-axisymmetric magnetic field distribution from a cross-shaped magnet was observed for distances below $l_{mag}/2$.

Important future work regarding Lorentz force velocimetry with conducting walls could focus on the investigation of erosion, oxide layer formation and wettability at the boundary liquid-solid using different combinations of wall materials and electrically conducting liquids. The next step regarding multicomponent Lorentz force velocimetry could focus on the investigation of non-steady velocity fields using arrays of multicomponent force and torque sensors for simultaneous scanning of a given area of the flow.

A List of publications

1. D. Hernández, T. Boeck, C. Karcher, and T. Wondrak. Numerical and experimental study of the effect of the induced electric potential in Lorentz force velocimetry. *Measurement Science and Technology*, 29(1):15301, 2018. DOI: 10.1088/1361-6501/aa9095.
2. D. Hernández, J. Schleichert, C. Karcher, T. Fröhlich, T. Wondrak, and K. Timmel. Local Lorentz force flowmeter at a continuous caster model using a new generation multicomponent force and torque sensor. *Measurement Science and Technology*, 27(6):65302, 2016. DOI: 10.1088/0957-0233/27/6/065302.
3. D. Hernández, T. Boeck, C. Karcher, and T. Wondrak. Numerical calibration of a multicomponent local Lorentz force flowmeter. *Magnetohydrodynamics*, 53(2):233-244, 2017.
4. M. Ratajczak, D. Hernández, T. Richter, D. Otte, D. Buchenau, N. Krauter, and T. Wondrak. Measurement techniques for liquid metals. *IOP Conference Series: Materials Science and Engineering*, 228:012023, 2017. DOI: 10.1088/1757-899X/228/1/012023.
5. D. Hernández, R. Marangoni, J. Schleichert, C. Karcher, T. Fröhlich, and T. Wondrak. Numerical and experimental study on vorticity measurement in liquid metal using local Lorentz force velocimetry. *Measurement Science and Technology*, 29(3):035301, 2018. DOI: 10.1088/1361-6501/aa9f85.
6. D. Hernández, and C. Karcher. Dynamics of liquid metal droplets and jets influenced by a strong axial magnetic field. *IOP Conference Series: Materials Science and Engineering*, 228:012010, 2017. DOI: 10.1088/1757-899X/228/1/012010.

B General description of the numerical model

For almost all experiments performed in this dissertation, a numerical model was developed in order to obtain a better understanding of the results. In every experiment, the average force or torque measurement was obtained for steady turbulent flows or moving solids. Hence, the simplified numerical model is based on the following assumptions:

- Kinematic regime of Lorentz force velocimetry
- The velocity field and the applied magnetic field are given and steady

When these assumptions are fulfilled, a fast and conservative assessment of the expected forces and torques acting on the magnet can be obtained. Once \vec{B}_0 and \vec{u} are defined, the induced electric potential is determined by solving (2.11) with insulating boundary conditions. Then through (2.10), (2.13) and (2.14), the values of \vec{j} , \vec{F} and \vec{T} are obtained. All partial differential equations in this thesis were solved using the PDE Module in the commercial FEM software COMSOL Multiphysics.

If possible, the velocity field in each case was obtained analytically, e.g. turbulent pipe flow (section 3.1.3) or laminar approximation for rectangular flows (section 3.3).

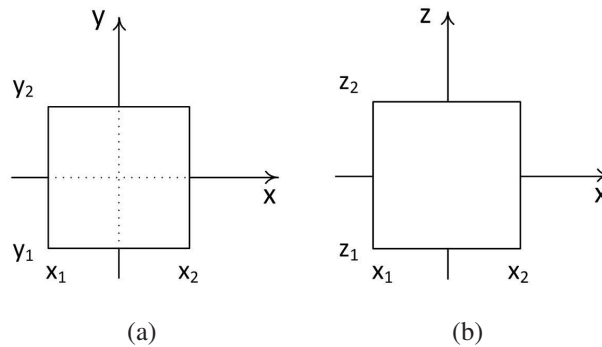


Figure 6.1: Cross-sectional views of a rectangular magnet on the $x - y$ plane (a) and on the $x - z$ plane (b).

If not, the results of previous simulations were used as the source of \vec{u} , e.g. a fully-developed turbulent flow in a rectangular duct (section 3.3) or in a continuous caster model (section 5.5). In the case of the applied magnetic field $\vec{B}_0 = B_x\vec{e}_x + B_y\vec{e}_y + B_z\vec{e}_z$ generated by a rectangular permanent magnet with magnetization $M_z\vec{e}_z$ (figure 6.1), there is an analytic solution for its components B_x , B_y and B_z , according to [12]. In this case, these components take the form

$$B_x(x, y, z) = \frac{\mu_0 M_z}{4\pi} \sum_{k=1}^2 \sum_{m=1}^2 (-1)^{k+m} \ln[F], \quad (6.1)$$

where

$$F(x, y, z, x_m, y_1, y_2, z_k) = \frac{(y - y_1) + [(x - x_m)^2 + (y - y_1)^2 + (z - z_k)^2]^{1/2}}{(y - y_2) + [(x - x_m)^2 + (y - y_2)^2 + (z - z_k)^2]^{1/2}}, \quad (6.2)$$

$$B_y(x, y, z) = \frac{\mu_0 M_z}{4\pi} \sum_{k=1}^2 \sum_{m=1}^2 (-1)^{k+m} \ln[H], \quad (6.3)$$

where

$$H(x, y, z, x_1, x_2, y_m, z_k) = \frac{(x - x_1) + [(x - x_1)^2 + (y - y_m)^2 + (z - z_k)^2]^{1/2}}{(x - x_2) + [(x - x_2)^2 + (y - y_m)^2 + (z - z_k)^2]^{1/2}}, \quad (6.4)$$

and

$$B_z(x, y, z) = \frac{\mu_0 M_z}{4\pi} \sum_{k=1}^2 \sum_{n=1}^2 \sum_{m=1}^2 (-1)^{k+n+m} \tan^{-1} \left[\frac{(x - x_n)(y - y_m)}{(z - z_k)} g \right], \quad (6.5)$$

where

$$g(x, y, z, x_n, y_m, z_k) = \frac{1}{[(x - x_n)^2 + (y - y_m)^2 + (z - z_k)^2]^{1/2}} \quad (6.6)$$

Here, x_n, y_m, z_k are given by the magnet dimensions with respect to the reference coordinate system and μ_0 denotes the permeability of free space.

C Uncertainty analysis

According to [55], uncertainties in measurements are classified into two groups: random uncertainties and systematic uncertainties. Random uncertainties reveal the experimental errors by repeated measurements, which can be treated afterwards statistically. If a measurement is repeatable, it should be repeated sufficiently often to obtain a reliable answer and to get a better estimate of the uncertainties. However, if the measurement is subjected to systematic errors, the repeated measurements will tend to the same direction despite a large number of repetitions. Systematic errors are for example the calibration of the sensor, starting conditions of the experiments, among others. The total uncertainty of the measurable value is a function of the random and systematic uncertainties. In the case of local LFV, the measurable force F is

$$F = F_{best} \pm \delta F_{total} \quad (6.7)$$

where $F_{best} = \bar{F}$ is the best estimate of the Lorentz force, and δF_{total} is the total uncertainty in the measurement. According to [55], δF_{total} is the quadratic sum of its corresponding random uncertainty δF_{ran} and systematic uncertainty δF_{sym} :

$$\delta F_{total} = \sqrt{(\delta F_{ran})^2 + (\delta F_{sym})^2}. \quad (6.8)$$

Here, δF_{ran} is given by the standard deviation of the mean \overline{SD} defined as

$$\delta F_{ran} = \overline{SD}(F) = \frac{SD(F)}{\sqrt{n}}. \quad (6.9)$$

Here, $SD(F)$ denotes the standard deviation of F and n the number of measurements. SD is given by the expression

$$SD(F) = \sqrt{\frac{1}{n-1} \sum_{i=1}^n (F_i - \bar{F})^2}. \quad (6.10)$$

Here, SD expresses the level of variability of the velocity distribution in the region adjacent to the wall next to the magnet at a fixed position.

Under systematic errors in local LFV we include the uncertainties of other parameters that have influence on the measurable Lorentz force. These are basically the factors that are not related to the velocity distribution of the flow, e.g. temperature, position of the magnet with respect to the flow, etc. According to (2.13), the Lorentz force acting on the magnet is a function of the applied magnetic field \vec{B}_0 acting on the flow and on the electrical conductivity of the liquid σ_l . According to propagation of uncertainty [55], δF_{sym} can be defined as

$$\delta F_{sym} = \left| \left(\frac{\partial F}{\partial \sigma_l} \right) \right| \delta \sigma_l + \left| \left(\frac{\partial F}{\partial B_0} \right) \right| \delta B_0. \quad (6.11)$$

Here, the first term of (6.11) represents the uncertainty of F caused by changes of σ_l and the second term expresses the uncertainty of F caused by changes of the applied magnetic field \vec{B}_0 . As it has already been discussed previously in section 2.3.1, the temperature of the environment has an influence on F as σ_l depends itself on the temperature of the liquid as well as \vec{B}_0 , which depends on the temperature of the magnet. In this thesis, the influence of the temperature on the measured forces can be neglected. For instance, the temperature change of GaInSn during 1 day of continuous measurements at ILMET did not exceed $2^\circ\text{C} \rightarrow \Delta \sigma_l \approx 0.3\%$ (thanks to the stainless steel pipes), and the magnets were always at room temperature. However, owing to the rapid decay of magnetic fields, the distribution of \vec{B}_0 in the liquid is therefore sensitive to the position of the magnet with respect to the liquid metal. Thus, it would be advantageous to express the second term of (6.11) as the uncertainty of F caused by variations of this distance in z -direction, which corresponds to the magnetization direction of the magnet. In this case, (6.11) takes the form

$$\delta F_{sym} = \left| \left(\frac{\partial F}{\partial z} \right) \right| \delta z \quad (6.12)$$

or

$$\delta F_{sym} = \delta F_{\Delta z}. \quad (6.13)$$

In the case of the of the experiments at ILMET using the 1D-L2F2 (chapter 4), the uncertainty of the position of the magnet with respect to the flow in z -direction is $\Delta z \approx 0.5\text{ mm}$. Then, $\delta F_{\Delta z}$ can be estimated using the fitting curves from figure 4.6(b) as follows $\delta F_{\Delta z} = F(\kappa) - F(\kappa + \Delta z)$. Here, κ corresponds to the distance between the surface of the magnet and the liquid metal. Table 6.1 summarizes all components of uncertainty at $y = 0\text{ mm}$ and $\kappa = 5\text{ mm}$ for all magnet systems, where the value of $\delta F_{\Delta z}$ and δF_{ran} reach their maximum value. According to table 6.1, the repeatability within one measurement series at a fixed position of the magnet is under 1% ($\delta F_{ran} < 1\%$).

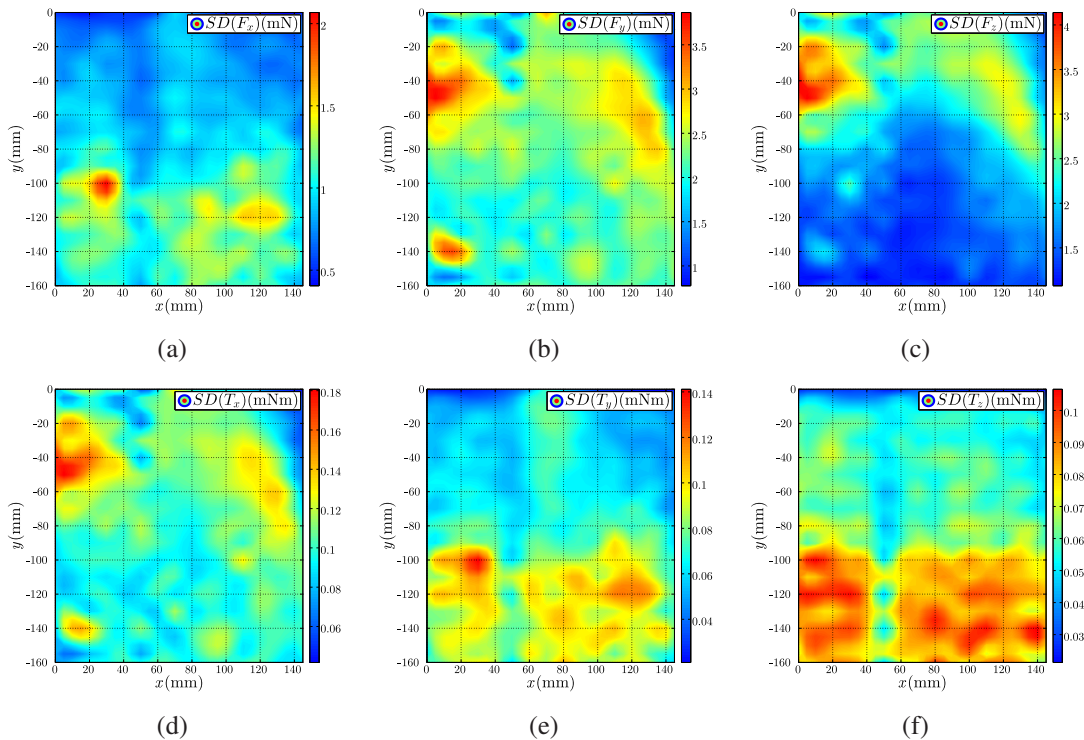
Table 6.1: Uncertainties components in ILMET

Magnet system	$F_{@y=0,z=0}$	$SD(F)$	$\delta F_{ran} = \overline{SD}(F)$	δF_{sym}	δ_{total}
CUB ₁₀	1.031 mN	6.7%	0.38%	13.0%	13.0%
CSM _{10.66}	1.093 mN	6.1%	0.34%	12.6%	12.6%
CSMA _{10.66}	1.081 mN	5.7%	0.32%	13.2%	13.2%

On the other hand, the reproducibility of the measurements can be as high as 13% ($\delta F_{sym} \approx 13\%$), when changing the magnet system and readjusting the set-up for a new series of experiments.

In the case of the experiments at the mini-LIMMCAST facility using the 6D-L2F2 (chapter 5), we start the uncertainty analysis of the experiments by obtaining the standard deviation of each force and torque component acting on each magnetic system across the wide face of the mold. The results are plotted on figures 6.2 and 6.3 for the CUB₁₅ and CSM_{31.17}, respectively.

According to figures 6.2 and 6.3, the standard deviation varies in every posi-

Figure 6.2: SD of each component of the measured force and torque signals acting on the CUB₁₅.

tion of the mold. It is shown that in complex 3-dimensional turbulent flows, the SD can be even higher than the maximum magnitude of its corresponding force or torque component across the measuring grid. Nevertheless, the \overline{SD} in the experiment at mini-LIMMCAST is around 1% as the values of the forces and torques are obtained from

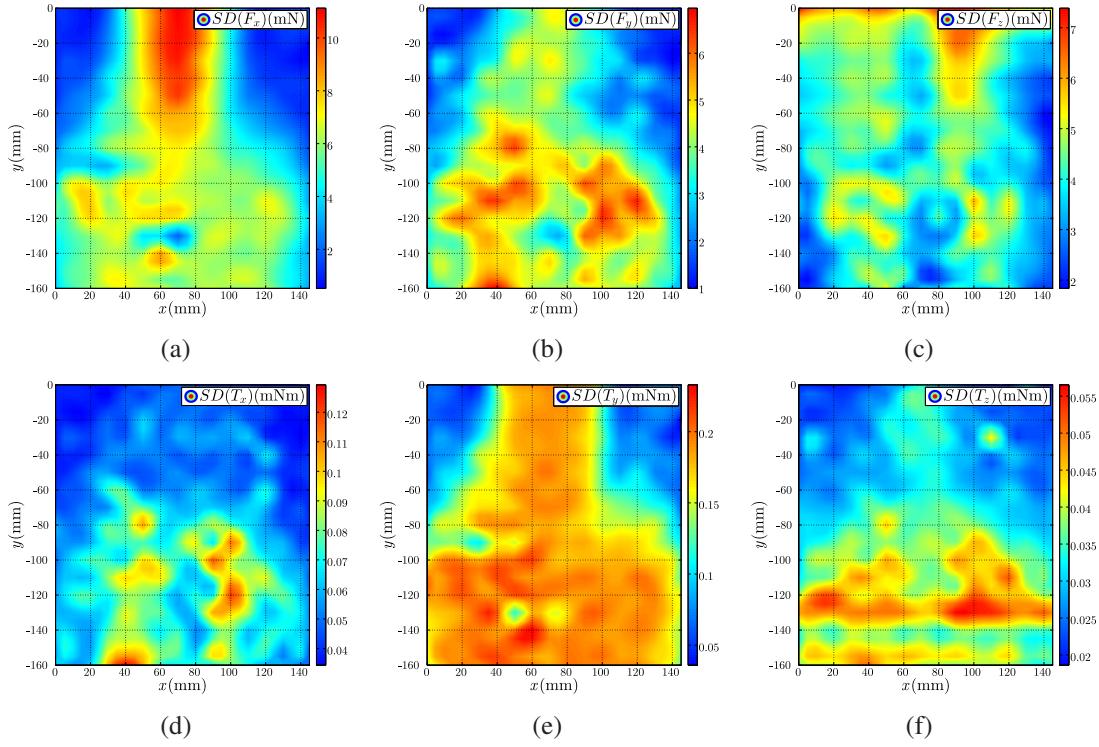

 Figure 6.3: SD of each component of the measured force and torque signals acting on the $CSM_{31.17}$.

 Table 6.2: Maximum value of each force and torque component with their corresponding maximum value of SD and δF_{ran} for the CUB_{15}

	$\max(F)$	$\max(SD(F))$	δF_{ran}
F_x	3.13 mN	66.2%	0.66%
F_y	6.76 mN	57.2%	0.57%
F_z	2.81 mN	147.3%	1.47%
T_x	0.355 mNm	51.0%	0.51%
T_y	0.167 mNm	84.4%	0.84%
T_z	0.113 mNm	94.1%	0.94%

 Table 6.3: Maximum value of each force and torque component with their corresponding maximum value of SD and δF_{ran} for the $CSM_{31.17}$

	$\max(F)$	$\max(SD(F))$	δF_{ran}
F_x	42.26 mN	26.4%	0.26%
F_y	44.44 mN	15.7%	0.16%
F_z	19.21 mN	38.5%	0.39%
T_x	0.921 mNm	14.0%	0.14%
T_y	0.844 mNm	27.6%	0.28%
T_z	0.036 mNm	156.8%	1.57%

a time-average of 5 seconds at 2000 Hz ($n = 10^4$ measured values). The maximum values of all three forces and three torques with their corresponding maximum value of SD across the measuring grid are summarized in table 6.2 and 6.3 for the CUB_{15} and $CSM_{31.17}$, respectively.

Due to the limited time for each measurement campaign at the mini-LIMMCAST facility, it was not possible to perform multiple measurements at different distances between the surface of the magnet and the mold in order to obtain an estimate of $\delta F_{\Delta z}$, i.e. δF_{sym} . Additionally, the complexity of finding a common characteristic decay of F increases in this case. This is due to the fact the force acting on the magnet is generated

from different velocity distributions in the liquid, and therefore, they will eventually show slightly different rates of decay at different points of the measuring grid.

References

References

- [1] N. P. Bansal and R. H. Doremus. *Handbook of glass properties*. Acad. Pr, Orlando, 1986.
- [2] C. M. Bender and S. A. Orszag. *Advanced Mathematical Methods for Scientists and Engineers I*. Springer New York, New York, 1999.
- [3] T. Boeck, M. Zec, and A. Thess. Electromagnetic drag on a magnetic dipole caused by a translating and rotating conducting cylinder. *Journal of Engineering Mathematics*, 88(1):177–195, 2014.
- [4] S. Cuevas, B. F. Picologlou, J. S. Walker, G. Talmage, and T. Q. Hua. Heat transfer in laminar and turbulent liquid-metal mhd flows in square ducts with thin conducting or insulating walls. *International Journal of Engineering Science*, 35(5):505–514, 1997.
- [5] P. A. Davidson. *An introduction to magnetohydrodynamics*, volume 25 of *Cambridge texts in applied mathematics*. Cambridge University Press, Cambridge, 2001.
- [6] Deutsche Edelstahlwerke GmbH. Crude steel production. <https://www.dew-stahl.com/en/company/production/crude-steel-production/>, 2017. [Online; accessed 01.10.2017].
- [7] N. Dubovikova, Y. Kolesnikov, and C. Karcher. Experimental study of an electromagnetic flow meter for liquid metals based on torque measurement during pumping process. *Measurement Science and Technology*, 26(11):115304, 2015.
- [8] N. Dubovikova, C. Resagk, C. Karcher, and Y. Kolesnikov. Contactless flow measurement in liquid metal using electromagnetic time-of-flight method. *Measurement Science and Technology*, 27(5):055102, 2016.
- [9] S. Eckert and G. Gerbeth. Velocity measurements in liquid sodium by means of ultrasound doppler velocimetry. *Experiments in Fluids*, 32(5):542–546, 2002.

- [10] S. Eckert, G. Gerbeth, and V. I. Melnikov. Velocity measurements at high temperatures by ultrasound doppler velocimetry using an acoustic wave guide. *Experiments in Fluids*, 35(5):381–388, 2003.
- [11] T. Fröhlich, F. Hillbrunner, and I. Rahneberg. *Vorrichtung zur simultanen Erfassung von Kraft- und Momentenkomponenten*, Patent DE102011106894B3, 2012.
- [12] E. P. Furlani. *Permanent magnet and electromechanical devices: Materials, analysis, and applications*. Series in electromagnetism. Acad. Press, San Diego, Calif., 2001.
- [13] R. Füßl and G. Jäger. The influence of the force feed-in system on high-accuracy low force measurement. In *Fundamental and applied metrology*, pages 235–238, 2009.
- [14] R. Füßl, G. Jäger, K. Hasche, and W. Holzapfel. *Interferenzoptische Kraftsensoren für den Lastbereich bis 0,1 Newton*. Habil.-schr., Technische Universität Ilmenau, Ilmenau, 2008.
- [15] D. J. Griffiths. *Introduction to electrodynamics*. Always learning. Pearson, Boston, 4 edition, 2013.
- [16] C. Heinicke. *Local Lorentz Force Velocimetry for liquid metal duct flows*. PhD thesis, Technische Universität Ilmenau, 2013.
- [17] C. Heinicke. Spatially resolved measurements in a liquid metal flow with lorentz force velocimetry. *Experiments in Fluids*, 54(6), 2013.
- [18] C. Heinicke, S. Tympel, G. Pulugundla, I. Rahneberg, T. Boeck, and A. Thess. Interaction of a small permanent magnet with a liquid metal duct flow. *Journal of Applied Physics*, 112(12):124914, 2012.
- [19] C. Heinicke and T. Wondrak. Spatial and temporal resolution of a local lorentz force flowmeter. *Measurement Science and Technology*, 25(5):055302, 2014.
- [20] D. Hernández, C. Karcher, and A. Thess. A lorentz force flow meter for application at blast furnaces: Design and calibration. *PAMM*, 14(1):725–726, 2014.
- [21] D. Hernández, J. Schleichert, C. Karcher, T. Fröhlich, T. Wondrak, and K. Timmel. Local lorentz force flowmeter at a continuous caster model using a new generation multicomponent force and torque sensor. *Measurement Science and Technology*, 27(6):065302, 2016.

-
- [22] J. C. R. Hunt. Magnetohydrodynamic flow in rectangular ducts. *Journal of Fluid Mechanics*, 21(04):577, 1965.
- [23] Institut Dr. Foerster GmbH und Co. KG. Sigmatest® 2.069. <https://www.foerstergroup.de/en/deu/products/sigmatest-2069/>, 2017. [Online; accessed 15.09.2017].
- [24] D. Jian and C. Karcher. Electromagnetic flow measurements in liquid metals using time-of-flight lorentz force velocimetry. *Measurement Science and Technology*, 23(7):074021, 2012.
- [25] O. Kazak, C. Heinicke, T. Wondrak, and T. Boeck. Electromagnetic interaction of a small magnet and liquid metal flow in a pipe with insulating or conducting walls. *Magnetohydrodynamics*, 51(3):579–588, 2015.
- [26] R. Klein, C. Weidemann, X. Wang, M. Gramss, A. Alferenok, A. Thieme, Y. Kolesnikov, C. Karcher, and A. Thess. Lorentzkraft-anemometrie für die berührunglose durchflussmessung von metallschmelzen. *Technisches Messen*, 79:394–398, 2012.
- [27] Y. Kolesnikov, C. Karcher, and A. Thess. Lorentz force flowmeter for liquid aluminum: Laboratory experiments and plant tests. *Metallurgical and Materials Transactions B*, 42(3):441–450, 2011.
- [28] D. Krasnov, O. Zikanov, and T. Boeck. Numerical study of magnetohydrodynamic duct flow at high reynolds and hartmann numbers. *Journal of Fluid Mechanics*, 704:421–446, 2012.
- [29] P. K. Kundu and I. M. Cohen. *Fluid mechanics*. Academic Press, San Diego, Calif., 2 edition, 2002.
- [30] S. Kunstreich and P. H. Dauby. Effect of liquid steel flow pattern on slab quality and the need for dynamic electromagnetic control in the mould. *Ironmaking & Steelmaking*, 32(1):80–86, 2013.
- [31] M. Leitner, T. Leitner, A. Schmon, K. Aziz, and G. Pottlacher. Erratum to: Thermophysical properties of liquid aluminum. *Metallurgical and Materials Transactions A*, 48(6):3159, 2017.
- [32] S. Liu and G. E. Kuhl. Temperature coefficients of rare earth permanent magnets. *IEEE Transactions on Magnetics*, 35(5):3271–3273, 1999.

- [33] V. Minchenya, C. Karcher, Y. Kolesnikov, and A. Thess. Dry calibration of the lorentz force flowmeter. *Magneto hydrodynamics*, 45(4):569–578, 2009.
- [34] V. Minchenya, C. Karcher, Y. Kolesnikov, and A. Thess. Lorentz force flow meter in industrial application. *Magneto hydrodynamics*, 45(3):459–465, 2009.
- [35] V. Minchenya, C. Karcher, Y. Kolesnikov, and A. Thess. Calibration of the lorentz force flowmeter. *Flow Measurement and Instrumentation*, 22(3):242–247, 2011.
- [36] U. Müller and L. Bühler. *Magneto fluid dynamics in Channels and Containers*. Springer Berlin Heidelberg, Berlin, Heidelberg and s.l., 2001.
- [37] Y. Plevachuk, V. Sklyarchuk, S. Eckert, G. Gerbeth, and R. Novakovic. Thermo-physical properties of the liquid ga–in–sn eutectic alloy. *Journal of Chemical & Engineering Data*, 59(3):757–763, 2014.
- [38] C. Pozrikidis. *Fluid dynamics: Theory, computation, and numerical simulation*. Kluwer Academic Publ, Boston, Mass., 2001.
- [39] J. Priede, D. Buchenau, and G. Gerbeth. Force-free and contactless sensor for electromagnetic flowrate measurements. *Magneto hydrodynamics*, 45(3):451–458, 2009.
- [40] J. Priede, D. Buchenau, and G. Gerbeth. Contactless electromagnetic phase-shift flowmeter for liquid metals. *Measurement Science and Technology*, 22(5):055402, 2011.
- [41] L. D. Pye, A. Montenero, and I. Joseph. *Properties of glass-forming melts*. Taylor & Francis, Boca Raton u.a., 2005.
- [42] I. Rahneberg. Multi-component force measurement systems. *Progress Report for the 1st Closed Session of the Research Training Group "Lorentz Force Velocimetry and Lorentz Force Eddy Current Testing"*, 2010.
- [43] I. Rahneberg, F. Hilbrunner, and T. Fröhlich. Novel concept of a high precision 6-dof force/torque transducer. In *NCSLI Annual Conf.*, 2011.
- [44] M. Ratajczak, D. Hernández, T. Richter, D. Otte, D. Buchenau, N. Krauter, and T. Wondrak. Measurement techniques for liquid metals. *IOP Conference Series: Materials Science and Engineering*, 228:012023, 2017.

-
- [45] M. Ratajczak, T. Wondrak, and F. Stefani. A gradiometric version of contactless inductive flow tomography: theory and first applications. *Philosophical transactions. Series A, Mathematical, physical, and engineering sciences*, 374(2070), 2016.
- [46] H. Schade, E. Kunz, and F. Kameier. *Strömungslehre*. De-Gruyter-Lehrbuch. de Gruyter, Berlin, 3 edition, 2007.
- [47] J. Schleichert. *Entwicklung und Untersuchung von Mehrkomponentensensoren für Kraft und Drehmoment*. PhD thesis, Technische Universität Ilmenau, Ilmenau, 2016.
- [48] J. Schleichert, I. Rahneberg, and T. Fröhlich. Calibration of a novel six-degree-of-freedom force/torque measurement system. *International Journal of Modern Physics: Conference Series*, 24:1360017, 2013.
- [49] O. Schulze. *Improvements in Speed Indicators*, Patent GB000190322622A, 1903.
- [50] J. A. Shercliff. *Textbook of magnetohydrodynamics*. Pergamon Press, Oxford, 1965.
- [51] F. Stefani, T. Gundrum, and G. Gerbeth. Contactless inductive flow tomography. *Physical review. E, Statistical, nonlinear, and soft matter physics*, 70(5 Pt 2):056306, 2004.
- [52] C. Stelian. Calibration of a lorentz force flowmeter by using numerical modeling. *Flow Measurement and Instrumentation*, 33:36–44, 2013.
- [53] C. Stelian, A. Alferenok, U. Lüdtke, Y. Kolesnikov, and A. Thess. Optimization of a lorentz force flowmeter by using numerical modeling. *Magnetohydrodynamics*, 47(3):273–283, 2011.
- [54] Y. Takeda. Measurement of velocity profile of mercury flow by ultrasound doppler shift method. *Nuclear technology*, 79(1):120–124, 1987.
- [55] J. R. Taylor. *An introduction to error analysis: The study of uncertainties in physical measurements*. University Science Books, Sausalito, Calif., 2. ed. edition, 1997.
- [56] N. Terzija, W. Yin, G. Gerbeth, F. Stefani, K. Timmel, T. Wondrak, and A. Peyton. Electromagnetic inspection of a two-phase flow of gainsn and argon. *Flow Measurement and Instrumentation*, 22(1):10–16, 2011.

- [57] A. Thess and T. Boeck. Electromagnetic drag on a magnetic dipole interacting with a moving electrically conducting sphere. *IEEE Transactions on Magnetics*, 49(6):2847–2857, 2013.
- [58] A. Thess, E. Votyakov, B. Knaepen, and O. Zikanov. Theory of the lorentz force flowmeter. *New Journal of Physics*, 9(8):299, 2007.
- [59] A. Thess, E. Votyakov, and Y. Kolesnikov. Lorentz force velocimetry. *Physical review letters*, 96(16):164501, 2006.
- [60] B. G. Thomas. Modeling of the continuous casting of steel—past, present, and future. *Metallurgical and Materials Transactions B*, 33(6):795–812, 2002.
- [61] K. Timmel, S. Eckert, and G. Gerbeth. Experimental investigation of the flow in a continuous-casting mold under the influence of a transverse, direct current magnetic field. *Metallurgical and Materials Transactions B*, 42(1):68–80, 2011.
- [62] C. Tropea, editor. *Springer handbook of experimental fluid mechanics*. Springer, Berlin u.a., 2007.
- [63] S. Vasilyan, R. Ebert, M. Weidner, M. Rivero, B. Halbedel, C. Resagk, and T. Fröhlich. Towards metering tap water by lorentz force velocimetry. *Measurement Science and Technology*, 26(11):115302, 2015.
- [64] S. Vasilyan and T. Froehlich. Direct lorentz force compensation flowmeter for electrolytes. *Applied Physics Letters*, 105(22):223510, 2014.
- [65] A. Viré, B. Knaepen, and A. Thess. Lorentz force velocimetry based on time-of-flight measurements. *Physics of Fluids*, 22(12):125101, 2010.
- [66] X. Wang, Y. Kolesnikov, and A. Thess. Numerical calibration of a lorentz force flowmeter. *Measurement science and technology*, 23(4):045005, 2012.
- [67] A. Wegfrass, C. Diethold, M. Werner, T. Fröhlich, B. Halbedel, F. Hilbrunner, C. Resagk, and A. Thess. A universal noncontact flowmeter for liquids. *Applied Physics Letters*, 100(19):194103, 2012.
- [68] A. Wegfrass, C. Diethold, M. Werner, C. Resagk, T. Fröhlich, B. Halbedel, and A. Thess. Flow rate measurement of weakly conducting fluids using lorentz force velocimetry. *Measurement Science and Technology*, 23(10):105307, 2012.
- [69] C. Weidemann. *Design and laboratory test of a Lorentz force flowmeter for pipe flows*. PhD thesis, Technische Universität Ilmenau, Ilmenau, 2013.

-
- [70] C. Weidermann, A. Thess, D. Lieftucht, and M. Reifferscheid. Application of lorentz force velocimetry (lfv) in continuous casting of steel. In *Fifth International Congress on Science and Technology of Steelmaking ICS*, 2012.
- [71] K. Weise, R. Schmidt, M. Carlstedt, M. Ziolkowski, H. Brauer, and H. Toepfer. Optimal magnet design for lorentz force eddy-current testing. *IEEE Transactions on Magnetics*, 51(9):1–15, 2015.
- [72] A. Wiederhold, R. Ebert, M. Weidner, B. Halbedel, T. Fröhlich, and C. Resagk. Influence of the flow profile to lorentz force velocimetry for weakly conducting fluids—an experimental validation. *Measurement Science and Technology*, 27(12):125306, 2016.
- [73] T. Wondrak, S. Eckert, G. Gerbeth, K. Klotsche, F. Stefani, K. Timmel, A. J. Peyton, N. Terzija, and W. Yin. Combined electromagnetic tomography for determining two-phase flow characteristics in the submerged entry nozzle and in the mold of a continuous casting model. *Metallurgical and Materials Transactions B*, 42(6):1201–1210, 2011.
- [74] T. Wondrak, V. Galindo, G. Gerbeth, T. Gundrum, F. Stefani, and K. Timmel. Contactless inductive flow tomography for a model of continuous steel casting. *Measurement Science and Technology*, 21(4):045402, 2010.
- [75] L. Zhang, S. Yang, K. Cai, J. Li, X. Wan, and B. G. Thomas. Investigation of fluid flow and steel cleanliness in the continuous casting strand. *Metallurgical and Materials Transactions B*, 38(1):63–83, 2007.

Erklärung

Ich versichere, dass ich die vorliegende Arbeit ohne unzulässige Hilfe Dritter und ohne Benutzung anderer als der angegebenen Hilfsmittel angefertigt habe. Die aus anderen Quellen direkt oder indirekt übernommenen Daten und Konzepte sind unter Angabe der Quelle gekennzeichnet.

Bei der Auswahl und Auswertung folgenden Materials haben mir die nachstehend aufgeführten Personen in der jeweils beschriebenen Weise unentgeltlich geholfen:

1. Die fachliche Betreuung der Arbeit erfolgte durch Prof. Dr.-Ing. habil. Christian Karcher und Dr. Thomas Wondrak (Helmholtz-Zentrum Dresden-Rossendorf).
2. Die analytischen Betrachtungen von Section 3.1.2 und Section 5.3.3 wurden von Priv.-Doz. Dr. Thomas Boeck durchgeführt.
3. Die Versuche von Section 5.3.5 wurden von Rafael Marangoni (TU Ilmenau) durchgeführt.
4. Die UDV Messungen von Abbildung 5.20(a) wurden von Dr. Klaus Timmel (Helmholtz-Zentrum Dresden-Rossendorf) durchgeführt.
5. Editage - English Language Editing Services, Elsevier (Abstract, Introduction, Conclusions): Sprachkorrektur; Ausschliesslich Bearbeitung von Rechtschreibung und Grammatik. Es wurden keine inhaltlichen Änderungen, Ergänzungen oder weitere Beiträge durch die Editoren vorgenommen. (entgeltlich)

Weitere Personen waren an der inhaltlich-materiellen Erstellung der vorliegenden Arbeit nicht beteiligt. Insbesondere habe ich hierfür nicht die entgeltliche Hilfe von Vermittlungs- bzw. Beratungsdiensten (Promotionsberater oder anderer Personen) in Anspruch genommen. Niemand hat von mir unmittelbar oder mittelbar geldwerte Leistungen für Arbeiten erhalten, die im Zusammenhang mit dem Inhalt der vorgelegten Dissertation stehen.

Die Arbeit wurde bisher weder im In- noch im Ausland in gleicher oder ähnlicher Form einer Prüfungsbehörde vorgelegt. Ich bin darauf hingewiesen worden, dass die Unrichtigkeit der vorstehenden Erklärung als Täuschungsversuch bewertet wird und gemäß §7 Abs. 10 der Promotionsordnung den Abbruch des Promotionsverfahrens zur Folge hat.

Ort, Datum

Unterschrift

Acknowledgments

The work has been financed by Helmholtz Alliance - Liquid Metal Technologies (LIMTECH) in the framework of the Young Investigator Group (YIG) and by the Deutsche Forschungsgemeinschaft (DFG) within the Research Training Group Lorentz Force Velocimetry and Lorentz Force Eddy Current Testing (GRK 1567).

I am grateful to my supervisors Prof. Christian Karcher and Dr. Thomas Wondrak (Helmholtz-Zentrum Dresden-Rossendorf) for their guidance, patience, useful critics and suggestions for improving my work each time. I would also like to thank Dr. Thomas Boeck for his useful suggestions and for been approachable for questions and for discussing new ideas; for helping me to improve the level of my work and of our mutual publications. Fruitful discussions with Prof. André Thess in our regular PhD meetings are gratefully acknowledged. I also thank Dr. Oleg Kazak for his help at the beginning of my work using COMSOL. I would also like to thank all colleagues for their help and support throughout my work here and for the friendly working atmosphere.

Finally, I will like to thank my family for their unconditional support and love.